

Cell Cytoplasm Compartmentalization: Localization Through Gradients

DISSERTATION

zur Erlangung des akademischen Grades

Doctor rerum naturalium
(Dr. rer. nat.)

vorgelegt

der Fakultät Mathematik und Naturwissenschaften
der Technischen Universität Dresden

von

jöbin gharakhani



MAX-PLANCK-INSTITUT FÜR PHYSIK KOMPLEXER SYSTEME

Dresden, 2012

Abstract

During embryonic development, precursor germ cells contain aggregates of protein and RNA known as germ granules. These germ granules are important in the specification of a functioning germ line, i.e. functioning sex cells within mature organisms. In the single cell fertilized embryo of the nematode worm *C.elegans*, germ granules (referred to as P granules) localize to the posterior side of the cell. After cell division occurs, they are found only in the posterior daughter cell. The localization behavior of P granules has been a topic of much interest, and considered an important aspect of symmetry breaking during development. We learn the fundamental properties of P granule localization, and determine possible parameters and features of this biological system by developing theory in close collaboration with experimental evidence.

In this study, experimental evidence is presented which shows that P granules are liquid droplets, and that their localization occurs through preferential nucleation and growth behavior on one side of the cell and simultaneous preferential dissolution on the opposite side. It is also shown that this behavior is linked to the concentration gradient of the protein Mex-5 along the antero-posterior axis of the cell, which is necessary to induce the preferential growth of P granules.

From this experimental data, a theoretical model for the preferential growth of P granules is developed, where the localization of P granules occurs by phase separation. That is, P granules separate from the bulk cytoplasm by a process described by a first order liquid-liquid phase transition, where a liquid droplet granule phase nucleates and then grows out of the bulk liquid cytoplasmic phase. In this model, a spatial gradient is imposed on the saturation point, the boundary point between the single phase state consisting only of the cytoplasm, and a metastable state which includes both a P granule and cytoplasm phase. This gradient mimics the properties of the Mex-5 gradient and is sufficient in explaining P granule localization.

Using numerical simulations, the theoretical model is studied. It is found sufficient to both successfully describe P granule localization, and to describe interesting behavior in a system with asymmetric growth due to a spatial gradient. From a purely theoretical standpoint, we observe cyclical non-equilibrium steady states, where material is cycled back and forth along the gradient. From the biological side, experimental properties of the system, such as the diffusion coefficient of P granules and P granule growth rates are determined through both simulation and image analysis of data. In addition, the possibility of different types of growth behavior at later cell stages, and a method of long range intracellular signalling are suggested from the theoretical model.

Acknowledgements

“My name is Ozymandias ...” – P.B.S

This work would not have been possible without the help and support of many people. I would like to thank in particular my collaborators, Clifford P. Brangwynne, who performed all the experiments presented in this text, Chiu Fan Lee, for his assistance in theoretical work and advice on this manuscript, Anthony A. Hyman, for discussions and the resources left to my disposal, and to my advisor, Frank Jülicher, for his guidance and patience throughout this time. In addition, I would like to explicitly mention the following people who were very helpful throughout this process, which I am quite thankful for: My parents, Bahram Gharakhani and Fereshteh Tahvilhdari, Helene Berthoumieux, Benjamin Lindner, Carsten Hoege, Dáibhid Ó Maoiléidigh, and Peer Mumcu.

Contents

1. Introduction	1
1.1. Cellular Organization	1
1.1.1. The Nematode <i>Caenorhabditis elegans</i>	4
1.1.2. Germ Granules	5
1.2. Pattern Formation by Phase Separation	7
1.2.1. First Order Phase Transition in a Binary Fluid	8
1.3. Overview of This Work	21
2. Germ Granule Segregation in the <i>C. elegans</i> Embryo	23
2.1. Mechanism of Localization	24
2.2. Properties of Germ Granules	29
2.2.1. Diffusion of Granule Components	29
2.3. Effects of the Mex-5 Protein Gradient on Growth	31
2.4. Chapter Summary	32
3. Droplet Kinetics in Presence of a Gradient	33
3.1. The Cytosol as a Binary Fluid	33
3.2. Single Droplet Growth Dynamics	34
3.3. Dynamics of the Model for Multiple Droplets	39
3.4. Droplet Dynamics in a Saturation Gradient	40
3.4.1. Spatially Dependent Free Energy Density	41
3.4.2. Monomeric Background Field	42
3.5. The Droplet Growth Model Within a Gradient	43
3.5.1. Continuum Description of Growth	43
3.5.2. 1-D Discrete Model	47
3.5.3. Model Implementation	49
4. Effects of a Spatial Gradient	55
4.1. Long Times, Non-Equilibrium Steady State	55
4.1.1. Multi-Droplet Steady State	59
4.2. Slow, Droplet Growth Regime	65
4.3. Chapter Summary	70
5. Comparison of Theory and Experiment	75
5.1. Determining Simulation Parameters	75
5.1.1. Free Energy Parameters from Experiment	77

5.1.2. Parameters Determined From Numerical Simulations	78
5.1.3. Discussion of Parameter Choices	80
5.2. Comparison of Data	80
5.2.1. P granule Distribution	82
5.3. Later Cell Divisions	86
6. Summary and Conclusions	89
6.1. General Summary	89
6.2. Future Outlook	90
A. Determining the Diffusion Coefficient of P granules	95
A.1. Advection	95
A.2. Size and Intensity	96
B. Flory-Huggins Free Energy	99
C. Balance of Droplet Growth with Exterior Particle Flux	101
D. Derivation of Background Monomer Field for Droplet Growth	105
Glossary of Terms	107
Bibliography	111

1. Introduction

“Man is foolish: he cannot make a worm, yet he will make gods by the dozen.”

– M.M.

An essential process for the existence of a biological organism is the coming together of different components. A particularly interesting region for this pattern formation occurs in a region that is far from extremes, 10^{-9} to 10^{-7} meters, we have a panoply biological molecules. Where mysteriously, almost magically, we journey from the world of physics, with descriptions of forces on particles, to complex living biological organisms, which at least seemingly to our naive eyes, appear to be much more than the sum of their parts. This biological regime, except for a few cases, has only been open to biologists, where its sheer complexity has kept it rather intractable to a physical approach and understanding. Significant technological advances in the last 50 years has slowly changed this; with the innovation of computers and a significant improvement in analytical tools, biology has become a realm that physicists can also explore.

The goal of this work is to take a physical approach to biological pattern formation. Specifically, to the question of how a molecular gradient can effect patterns on the intracellular level. In this thesis, we investigate in detail the segregation of P granules within the *C. elegans* embryo. Non only do these granules present an excellent system to study using basic physical principles, but they also provide an interesting and novel non-equilibrium system.

1.1. Cellular Organization

The cell is a highly complex object. In simple terms, it can be described as a semi-permeable membrane (plasma membrane), the enclosed fluid medium (cytoplasm), and a nucleus. Within the cytoplasm are macromolecules, such as proteins, nucleic acids, lipids, and larger structures, such as polymers made of these components. There are also many highly organized compartments, organelles, often specialized to do certain tasks.

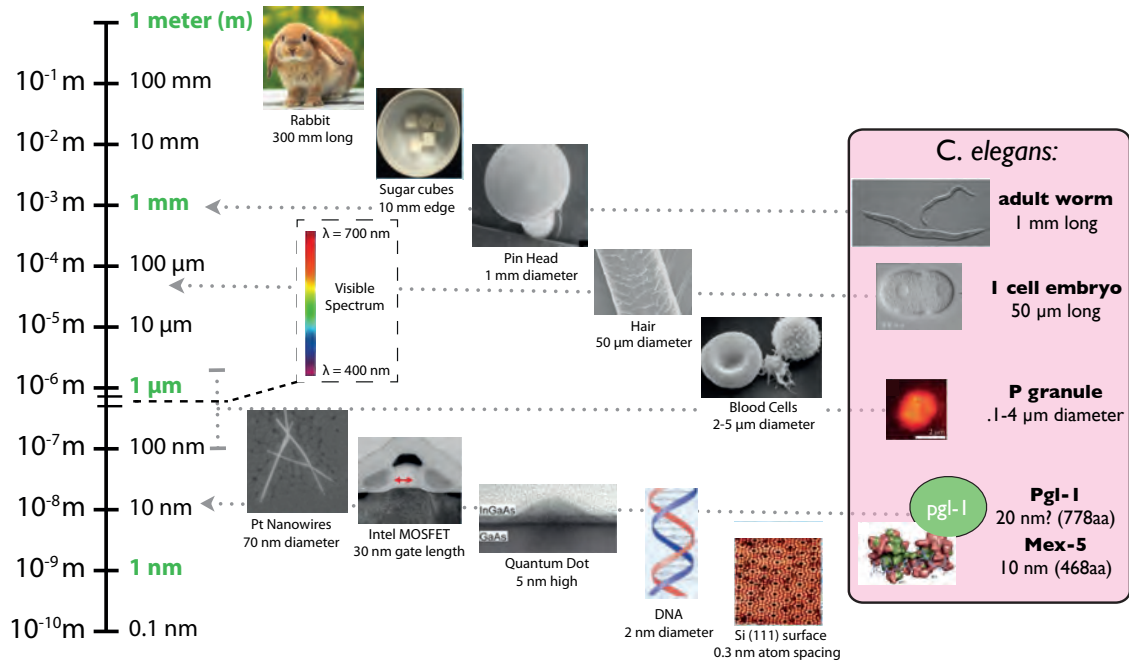


Figure 1.1.: The length scales of life, and how *C. elegans* compares to them. No conclusive data exists for the size of the protein Pgl-1, the size is guessed from the length of its amino acid sequence. Original image edited from Tyndall National Institute. *C. elegans* worm image from Dr. M.C. Leaver (MPI-CBG), Single cell and P granule image by Dr. C.P. Brangwynne (MPI-CBG), and Mex-5 image from Pagano et al. (2007).

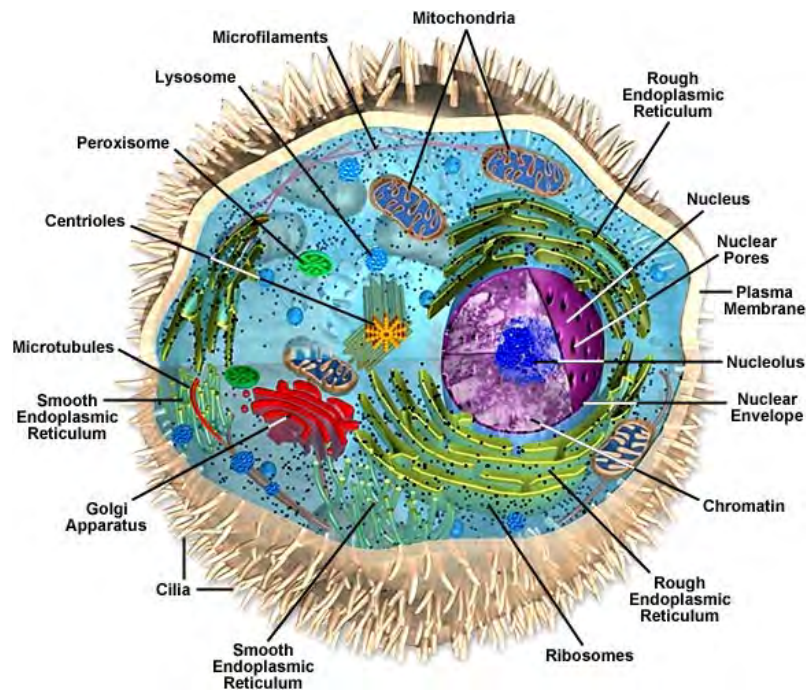


Figure 1.2.: Drawing of a typical animal cell, with many labeled organelles. Michael W. Davidson, Florida State University

Figure 1.2 is a drawing of a representative animal cell, where the most common organelles are labeled. Although they do not exist in every cell, the major organelles of a typical eukaryotic animal cell are considered to be a Nucleus, which contains the DNA of the cell, and is the location for DNA replication and RNA transcription; Ribosomes, the location for protein translation; Endoplasmic Reticulum (ER), location for protein folding, protein modification, and lipid creation; Golgi Apparatus, location for additional protein modifications and protein sorting; Mitochondria, the energy production organelle of the cell; and Vacuoles, the cells garbage bin, which break down highly ordered structures into small pieces for possible reuse or removal [2]. These distinct organelles can, and often are spatially connected when they perform similar or complimentary tasks, e.g. the ribosomes, that translate membrane bound proteins, sit directly on the ER and feed proteins they are translating directly into the ER to be modified [2].

All organelles so far mentioned, except the ribosomes, are surrounded by lipid membranes, which separate them from the cytoplasm. In addition to giving organelles clear boundaries, lipid membranes are necessary for other tasks, where their roles can depend on their lipid composition, and on proteins embedded inside or attached on the surface of these membranes. These processes can be highly varied. The membrane of the nucleus creates a clear separation between the interior and exterior of the nucleus, strongly regulating which molecules can pass through, the membrane of the endoplasmic reticulum is the location for protein folding, and the membrane of the mitochondria is the location of energy production, where the proteins in the membrane of the mitochondria act in a fashion not so dissimilar to connecting the two ends of a battery, which would be the two sides of the membrane in this case. One last benefit of the membrane which is worth mentioning, is that they give nice and tidy closed objects, making it oftentimes easier from a practical standpoint to identify and define individual organelles. Without a membrane, it is not always obvious where the boundary of an organelle actually is, and one must make use of some new metric to define and distinguish the organelles surface.

Non-membrane organelles are, as per the original definition of the word, not in fact organelles. But as science has progressed, and more and more membraneless structures in the cell have been discovered which encompass the criteria of organelle (excluding this one fact), the term has gained some popularity. These membraneless organelles can be highly varied in properties. Centrosomes, for example, are complex protein structures made mostly of microtubule structures. The greater part of this structure “appears” rather disorganized. Also, no clear boundary exists between it and the cytoplasm, as microtubules jut out in all directions from the centrosome into the cytoplasm [27]. Germ granules (which are the focus of this work), and nucleoli do in fact have clear boundary with the cytoplasm. Both these organelles display liquid properties, with constant fluid like rearrangement of proteins in their interior. As fluids, they both form droplets with a measurable surface tension within the cytoplasm [7]. Ribosomes, which are large complex protein structures, have both a very organized interior, and a distinct boundary with the cytoplasm. As this work

is primarily concerned with germ granules, two organelles without a membrane, the boundaries of membrane-less organelles will be discussed in more detail in later sections.

1.1.1. The Nematode *Caenorhabditis elegans*

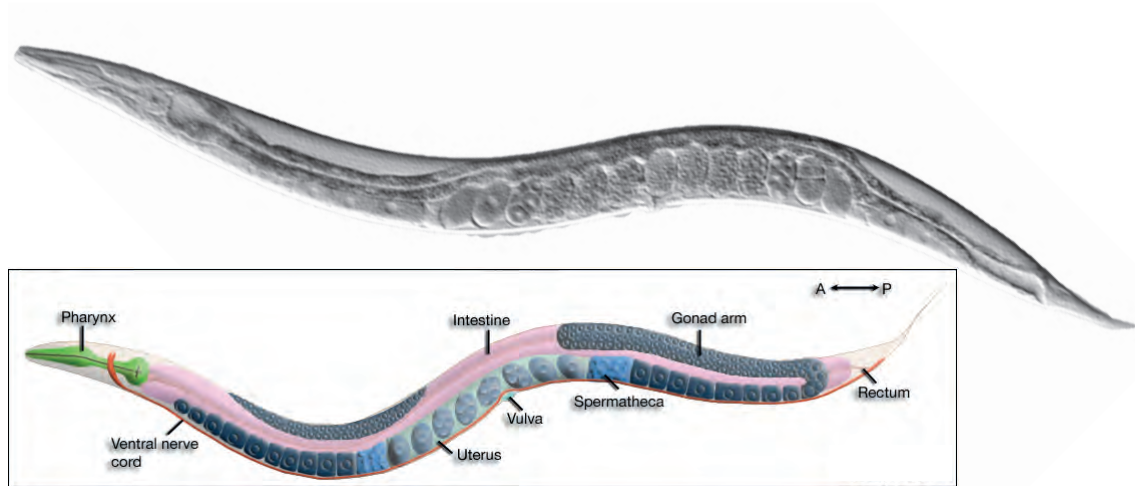


Figure 1.3.: DIC image of a mature hermaphroditic *C. elegans* worm and a schematic drawing of its anatomical structures. DIC image courtesy of Dr. M.C. Leaver from the Max Planck Institute for Cellular Biology and Genetics (MPI-CBG), and schematic drawing from worm atlas (www.wormatlas.org).

Considering that all experimental results presented in this text were performed on the embryo of the model organism *Caenorhabditis elegans* (*C. elegans*), a bit should be said about this tiny creature. Measuring about a millimeter, this small nematode can be found throughout the world [15]. Research upon this organism was mainly started by Sidney Brenner in the 1970's, due to its rather fast life cycle [9] and translucence, such that one could observe *C. elegans*' inner-workings even in the living worm (figure 1.3). Since that time, it has been a popular model organism and at the forefront of many biological advances. It was the first multicellular organism to have its entire genome mapped out [4], all 959 cells of the worm during development have been determined [60], and RNA interference (RNAi) was first discovered in the *C. elegans* [17].

C. elegans has two sexes, hermaphroditic and male. The hermaphroditic is the more common type and can reproduce by self-fertilization or by becoming impregnated by a male [15]. A large volume of the worm is devoted to reproduction. Due to the *C. elegans*' translucence, developing oocytes (eggs), the many round structures on the bottom half of the worm, can be observed (in figure 1.3). These oocytes are pushed through the germline of the worm by contractions of muscles around the germline. During the passage of the oocyte through the spermatheca, they are

injected by sperm and start developing within the parent worm. The worm can at this point be dissected, and these developing embryos can be studied.

1.1.2. Germ Granules

An important theme of this thesis is to understand germ granule segregation. In a nutshell, germ granules are “large, non-membrane-bound, ribonucleoprotein organelles found in the germline cytoplasm of most, if not all, animals.” (Updike, Strome 2009 [78]). In mammals, these germ granules are typically referred to as perinuclear material, and in the nematode *C. elegans*, they are referred to as P granules. There have been many studies on germ granules in the last quarter century in many different organisms, and there is much understanding with regards to individual proteins within the granules, but to this day these as a whole, structures are not fully understood [70, 25]. Most of this knowledge comes from research done on invertebrate model organisms, particularly *C. elegans*. Since this work is based on experiments performed on the *C. elegans* worm, the term P granule and germ granules will be used synonymously throughout this text.

Composition and Function

Even though there is much known about many of their individual components, P granule function is still essentially a mystery. What is known, is that they are highly varied in their number and size. Both number and size distributions change dramatically during the development of the embryo [33, 6]. It is also known that during the cell divisions of a *C. elegans* embryo, the granules consistently localize to the P-lineage cells, which are the precursor cells to the germline of the fully developed worm.¹ Preventing the formation of P granules, or inhibiting one of their main components, typically leads to a dysfunctional germline, e.g. a sterile worm [3, 36, 66, 67]. It can thus be said that P granules are necessary for the formation of a functioning germline, and the formation of totipotent cells within said germline: cells which have all the genetic material of the organism, and can differentiate into all cell types.

P granules are mainly comprised of proteins and mRNAs (messenger RNA). There have been, so far, 41 proteins discovered within the P granule [78]. A majority of them are involved in RNA modification. Several of the proteins, which belong to the multi-gene family GLH (germline helicase), have regions rich in the amino acid glycine (G) [29, 40]. More specifically they have so called FGG repeats, where F refers to the amino acid phenylalanine. Generally these repeats are known to localize the protein to the nuclear pore complex [71, 21, 1]. This phenomenon has also been observed in the *C. elegans*, where from the 4 cell stage of embryogenesis and on, P granules localize to the nuclear membrane. In the mature worm, 75%

¹In fact, the reason germ granules are referred to as P granules in the *C. elegans* is due to the observation that they localize to the P-lineage cells.

of the nuclear pores in the germline are associated with P granules [54]. Another protein family, PGL (P Granule abnormality), also has glycine rich repeats, RGG repeats (R refers to Arginine) [37, 36]. These repeats are known to function as RNA binding domains [39]. The PGL proteins are a constitutive component of P granules which are localized within the granules throughout all cell stages [36, 37], and thus a common marker to observe granules.

In addition to proteins, mRNAs make up the other major component of P granules. In the developing embryo these mRNA are maternally inherited, while in the adult germline, as observed by Schisa et al.(2001), they are made locally and are concentrated within the P granules [61]. Some of the maternally inherited mRNA strands in the P granules do in fact initially exist throughout the cell, but they are quickly broken down in the cytoplasm and in P granule deficient cells [63]. Comparing concentrations of six mRNAs required for gonadogenesis with actin and tubulin mRNAs, Schisa noted that the gonadogenesis mRNAs were concentrated in the P granules, while the actin and tubulin mRNAs showed no significant levels of enrichment.

Early in embryogenesis, transcription is significantly inhibited throughout the embryo. Later in development, when transcription begins to take place in the somatic cells, it continues to be inhibited throughout all development in the primordial germline cells [38, 59]. Thus this maternal mRNA contained within the P granules could be a significant source of RNA, until transcription starts up in the hatched larvae.

Since most known activities of the P granules components are related to RNA metabolism, and it is likely that the granules provide RNA, it is believed the P granule's main function is post-transcriptional regulation.

Localization

In *C. elegans*, primordial germ granules are inherited maternally, as opposed to mammals where they are formed by epiblast cells through inductive signals [32]. Figure 1.4 shows a simple

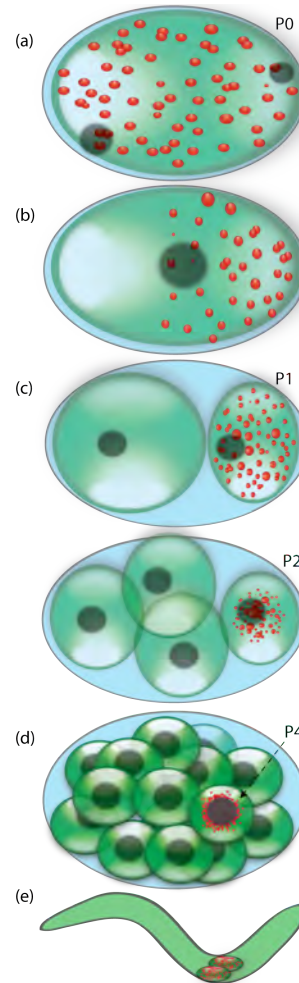


Figure 1.4.: P granule Segregation during *C. elegans* development. P granules (red) localize to one side of the cell, which becomes the P-lineage cell after cell division. At the P4 cell stage, the P-lineage cell undergoes symmetric cell divisions to eventually form the germline of the developed worm. See text for more details.

overview of the P granule localization behavior. Initially, prior to symmetry breaking these granules (red) are evenly distributed throughout the ovum (fig.1.4a). Once the egg is fertilized, the symmetry of the cell is broken along the antero-posterior (AP) axis: the polarity proteins (PAR) appear on the cortex, cortical and cytoplasmic flows develop, and the P granules localize to the posterior side of the cell as the two parental pro-nuclei (black) join (fig. 1.4b) [62]. Once cell division occurs, only the single precursor to the primordial germ cells, i.e. P-lineage cells: P1, P2, P3, P4, contains the granular material (fig. 1.4c and 1.4d). [70, 69] Thus after the first cell division, all granules are in the P1 cell, leaving its sister somatic cell P granule deficient. As cell divisions progress, the granules fuse and become larger and progressively more concentrated, primarily due to the smaller size of the new daughter cell, since there is no new P granule material being made at the time. At the P2 cell stage, granules start associating more with the nucleus of the cell, and can be easily observed within proximity of the nucleus. At the 16 cell stage, where the P granules are contained in the P4 cell, they localize completely to the nucleus of the cell, and the general behavior of the P granules change (fig. 1.4d); The P4 cell divides symmetrically into the two primordial germ cells, Z2 and Z3 (not shown), which both contain germ granules. These two primordial germ cells eventually undergo many symmetric cell divisions until they form approximately 1000 germ cells in the adult gonad of the *C. elegans* worm (fig. 1.4e).

The major reason why the P granules have been so extensively studied, and a primary interest of this work, is due to this segregation behavior. Their consistent segregation to P-lineage cells have been a helpful factor in investigating cell polarity and asymmetry, and P granule components are commonly marked to monitor and determine the effectiveness of these asymmetric cell divisions under different experimental conditions [70].

1.2. Pattern Formation by Phase Separation

A typical characteristic of non-equilibrium systems is the spontaneous growth of spatial and temporal non-uniformities under homogeneous external conditions, i.e. pattern formation. The study of pattern formation has been a major focus of physicists for the last half century, where its study emerged as an outgrowth of material scientists' interest in phase transitions [24]. In fact, many well known examples of pattern formations occur when a system changes from one phase to another, e.g. a liquid converts to a geometrically patterned solid, or a uniform mixture of constituents phase separates into a pattern of precipitates.

A central concept to the understanding of pattern formations is instability. Where a relatively uniform system, near equilibrium, is driven to an unstable state. That is, it is driven to a state that demonstrates large deformations in response to infinitesimal perturbations. Some intrinsically nonlinear mechanism is then required to move the system to a new state that may, or may not, resemble the unstable

deformation of the original state [23]. The mechanism of the instability depends on the details of the system, where a detailed understanding of these mechanisms can only be achieved if the system is well characterized by its microscopic equations. Although instabilities of the system may not be exactly known, their properties can be estimated and often related to the system. Instabilities are typically classified into three simple types [13]: 1) Spatially periodic temporally stationary instabilities often lead to spatially regular patterns, such as squares and hexagons, where typically only a single structure type is stable. 2) Spatially uniform temporally oscillatory instabilities typically lead to uniform states with uniform oscillations. 3) Spatially periodic and temporally oscillatory instabilities can lead to traveling wave trains; where more complex patterns, or standing waves, can also emerge due to the superposition of multiple waves.

Pattern forming systems are generally described by nonlinear partial differential equations, such as the Navier-Stokes equations for fluids, and diffusion-reaction equations for the chemical systems [24]. Due to Alan Turing’s seminal paper on morphogenesis in 1952 [77], these diffusion-reaction systems are often referred to as Turing mechanisms. In his description of morphogens, Turing suggested that chemicals reacting and diffusing could form spatially heterogeneous patterns. Turing mechanisms have many types of steady state solutions, including periodic and traveling waves [23]. As one would expect, these type of systems can start from near uniform initial conditions and lead to spatially distinct structures, a characteristic often seen in differentiating cells in e.g. developmental biology. These type of systems can describe a rather broad range of phenomena, with many examples in biology, e.g. formation of spots on a leopard [52], and growth control of tissues, such as the wings of a fruit fly [81]. To study P granule localization, in this work, we will be concerned with pattern formation due to spatial instabilities in the boundary of a phase transition.

1.2.1. First Order Phase Transition in a Binary Fluid

In the study of phase transitions, binary mixtures have been one of the most researched systems, both experimentally and theoretically, e.g. [5, 18, 26, 31, 43, 53]. In addition to the actual study of phase transitions, phase transitions in binary fluids have been used to model many physical systems, such as droplet collection within clouds and warm rain formation [48]. To completely understand phase transitions properly, one would ideally develop a full microscopic theory of their kinetics. Since this effort would be quite frankly futile, we focus on a coarse-grained description of the system; a small set of semi-macroscopic variables are identified, whose dynamics are slow with respect to the remaining microscopic degrees of freedom of the system. We then use phenomenological arguments to write dynamic equations for our new slow variables, where the fast variables enter the description as random forces.

In the case of a binary fluid, one component, the solute (component “b” or the granule component as presented later), is considered to diffuse within the other com-

ponent, the solvent (component “a” or cytoplasmic component). As the amount of solute is significantly less than the solvent, when the system is in a single mixed state, it is considered to express the characteristics of the solvent. The semi-macroscopic variables of interest would be the concentrations of the two components. Since the biological system which will be studied in forthcoming chapters is a closed system, and what we assume to be an incompressible system, the local volume fraction of the solute is sufficient to describe the system (since the fraction of the volume not taken up by the solute is taken up by the solvent). We thus define the volume fraction within some volume V , as the volume fraction of the solute,

$$\phi \equiv \frac{N^b v^b}{V}, \quad (1.1)$$

where the N^b is the number of solute molecules and v^b is the molecular volume of the solute. The volume fraction also plays a dual role. It is the order parameter for the phase transition from the single mixed state, to a bistable de-mixed state². Thus, for a set of fixed control parameters, the volume fraction of the system tells whether the system would be in a single or 2-phase state at equilibrium.

Quenching experiments are a typical method used to study 1st order phase transitions. The system is initially started at a sufficient temperature to be in a single mixed state. It is then cooled (quenched) to below the critical temperature, such that the system becomes either metastable or unstable, and phase transitions are observed. The arrows shown on the phase diagram, figure 1.5, illustrate these quenching experiments. The saturation volume fractions, ϕ_0^s, ϕ_1^s , are the two points on the coexistence curve for some given temperature T , i.e. the minimum (or maximum) volume fraction required to have two phases. Although the phase diagram for a generic binary fluid is symmetric, as per the definition of solute and solvent, we are only interested in a small concentration of solute within a mostly solvent mixture. Thus, only the left half of figure 1.5 is relevant, and the saturation point will always refer to ϕ_0^s , the minimum solute volume fraction required for two-phase coexistence at a fixed temperature. The supersaturation, δ , how far the system is from the single-phase region, is then unambiguously,

$$\delta \equiv \phi - \phi_0^s, \quad (1.2)$$

where the system exists in a two-phase state only for $\delta > 0$.

Of particular interest to this work, are the dynamics involved with moving from the single state phase, to the metastable binodal region. That is, the formation of a (droplet) minority phase by quenching a single mixed phase system to the binodal region (see left arrow in fig.1.5). Initially, many droplets of a critical size form through localized fluctuations of the granule component. This critical size

²The order parameter of a 2-phase binary fluid is typically presented as the difference of volume fractions between the two components, but for a closed incompressible system, the volume fraction of a single component is again sufficient.

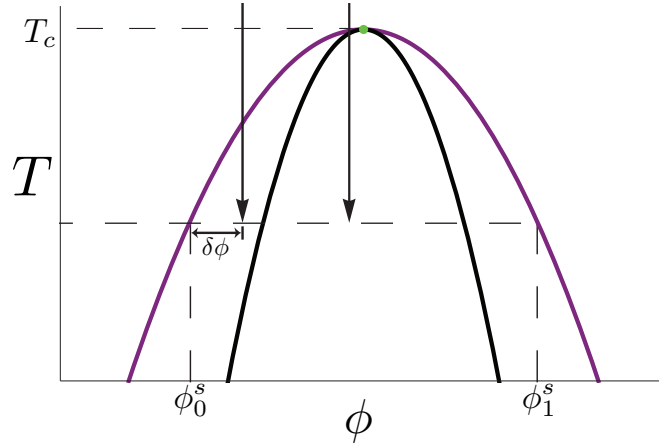


Figure 1.5.: Phase diagram of a binary fluid with order parameter ϕ . The coexistence curve (purple) separates the mixed single phase and the binodal region, while the spinodal curve (black) separates the binodal and spinodal regions. The arrows show quenches, where a system is moved from a single phase state, to below the critical temperature T_c , such that it is in a metastable region (left arrow), or an unstable region (right arrow), with a supersaturation $\delta\phi \equiv \phi - \phi_0^s$.

is set by competition between a stabilizing bulk term, and a destabilizing surface term and thus a property of the free energy of the system. Once these critically sized droplets are formed, the system then coarsens through droplet growth and eventually Ostwald Ripening to its final equilibrium state; which for a finite system, would be a single droplet of a specific size set by the free energy and initial supersaturation of the system. This nucleation of critically sized droplets, and growth behavior is in distinct contrast to the kinetics of the spinodal region (see right arrow in fig. 1.5), where fluctuations of all orders of magnitude occur in the formation of the new phase, and no critical size is observed [64].

Equilibrium Description of a Binary Fluid

To give a continuous description of a binary fluid, we follow the Cahn-Hilliard formalism [10]. We assume a “nonuniform” system with a small composition gradient as compared to the inverse of the intermolecular distance, such that ϕ and its gradients can be considered independent variables. To a first order approximation about $f(\phi)$, the free energy of the system is given by the Ginzburg-Landau free energy functional,

$$F[\phi] = \int d^3r \left(\frac{1}{2} K (\nabla\phi)^2 + f(\phi) \right), \quad (1.3)$$

where $f(\phi)$ is the free energy density for a spatially uniform state (which will be discussed shortly). The gradient term is the 1st order correction from the uniform state, which accounts for short range molecular interactions, and higher order terms have been ignored.

This is a coarse-grained free energy which can be derived in multiple ways with respect to the microscopic variables of the system [35]. We consider a system with microscopic states, $\{\phi_\alpha\}$, such that the probability to be in the state, $\{\phi_\alpha\}$ is given by the Boltzmann distribution,

$$P\{\phi_\alpha\} = e^{-H\{\phi_\alpha\}/k_B T} Z^{-1}, \quad (1.4)$$

where $H\{\phi_\alpha\}$ is the Hamiltonian as a function of the microscopic variables, and Z is the partition function. A common method to define the coarse-grained free energy, suggested by VanKampen (1964) [35], is to divide the system into semi-macroscopic cells, where ϕ_i is the average volume fraction of cell i ,

$$\phi_i = L^{-1} \sum_{\alpha \in i} \phi_\alpha \quad (1.5)$$

and is defined as the volume fraction at the center of the cell, where the continuous volume fraction, $\phi(\mathbf{r}_i) \equiv \phi_i$ at the center of the cell. Then choosing a proper cell edge size L , such that $\phi(\mathbf{r})$ varies slowly over the cell length, allows us to write a coarse grained free energy, such that this new probability distribution for some state ϕ_i is,

$$e^{-F[\phi_i]/k_B T} \equiv \sum e^{-H\{\phi_\alpha\}/k_B T}, \quad (1.6)$$

where the summation is over all constrained microscopic configurations $\{\phi_\alpha\}$ consistent with the state ϕ_i .

Since these microscopic variables are still for practical purposes intractable, they are ignored [44]. The coarse grained free energy is assumed ad-hoc to have the Cahn Hilliard form as initially stated, equation 1.3, with an additional requirement on the free energy density, $f(\phi)$; that for a two phase system, below the critical point, the free energy density is required to have two minima. This is commonly presented as [31],

$$f(\phi) = -\frac{1}{2}a\phi^2 + \frac{1}{4}b\phi^4 + \dots, \quad (1.7)$$

where $f(\phi)$ is usually cut off at the 4th order term, and the parameters of the free energy are phenomenologically fit to experiment. It is also possible to choose some energy density that satisfy our requirements, such as the regular solution, which was the initial free energy density analyzed by Cahn and Hilliard [10], or as in our case, the Flory-Huggins energy (see Appendix B).

To understand the dynamics of binodal growth, we start first by examining the equilibrium state of a two phase system. In a system near or at equilibrium, concentration gradients within the bulk of the system become negligible. In addition, we assume that the size of each phase is significantly larger than the width of the interface between them. The thickness of the interface is thus neglected, and the gradient across the interface replaced by a surface tension parameter, γ . The free energy of this system can then be written as a piecewise addition of the free energy of each phase and interface. Thus, the free energy for a system with a single droplet

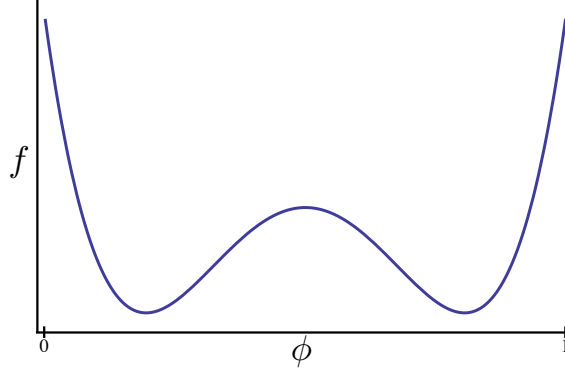


Figure 1.6.: Sample free energy density below the critical point, symmetric with two minima.

would be the energy of a droplet phase of volume fraction ϕ_1 and radius R , and a solution phase of volume fraction, ϕ_0 , and volume V_0 is,

$$F(\phi_1, R) = V_0 f(\phi_0) + 4/3\pi R^3 f(\phi_1) - 4\pi R^2 \gamma, \quad (1.8)$$

where the first two terms on the right hand side refer to the bulk free energies of the solution and droplet phase respectively, and the final term is the interfacial energy between two phases. For a closed system with total volume V , and initial volume fraction $\bar{\phi}$, the solution volume V_0 , and solution volume fraction ϕ_0 , are dependent variables due to conservations of volume and molecule number,

$$V_0 = V - 4/3\pi R^3 \quad (1.9)$$

$$\phi_0 = (\bar{\phi} V - \phi_1 4/3\pi R^3) / V_0. \quad (1.10)$$

The global parameters, V and $\bar{\phi}$, with the free energy, are then sufficient to determine all the equilibrium properties of the system. By allowing the system to relax with respect to droplet size and volume fraction, that is,

$$\frac{\partial F}{\partial \phi_1} = 0 \quad (1.11)$$

$$\frac{\partial F}{\partial R} = 0 \quad (1.12)$$

the critical size and equilibrium properties of the system can be determined from the conditions³,

$$\mu_1 = \mu_0 \quad (1.13)$$

$$\frac{2\gamma}{R} = f(\phi_1) - f(\phi_0) - \mu_1(\phi_1 - \phi_0), \quad (1.14)$$

³Although it appears that one could determine R from basic algebra, depending on the form of $f(\phi)$, equation (1.14) is quite often an implicit equation for R with no analytical solution.

where the chemical potential, μ , is defined as,

$$\mu_0 = \left. \frac{\partial f}{\partial \phi} \right|_{\phi=\phi_0} ; \quad \mu_1 = \left. \frac{\partial f}{\partial \phi} \right|_{\phi=\phi_1}. \quad (1.15)$$

A graphical representation of the minimization conditions, eqns. (1.13) and (1.14), are shown in figure 1.7. The equilibrium volume fraction along a flat interface (droplet of infinite size) defines the saturation volume fraction, $\phi^s \equiv \phi_0(R \rightarrow \infty)$, shown in the left plot, and corresponds to ϕ_0^s on the phase diagram in figure 1.5. For

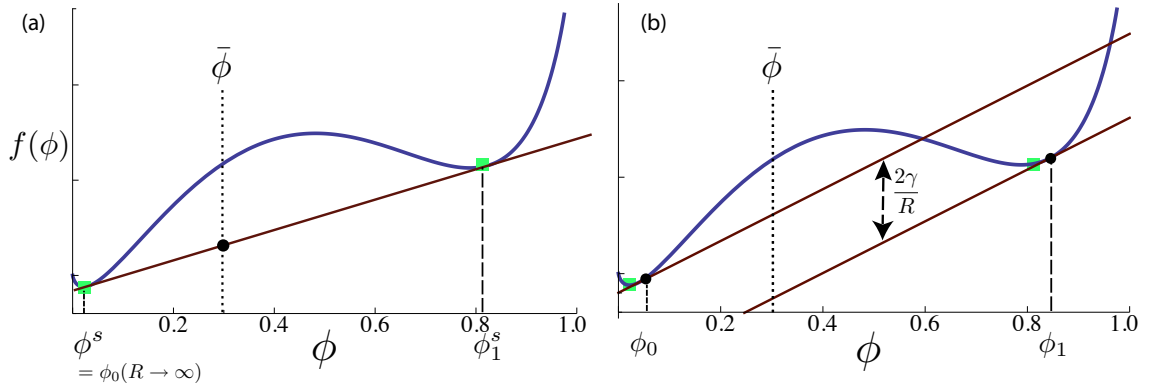


Figure 1.7.: Graphic representation of the equilibrium conditions, equations (3.11) and (3.12), along a sample free energy density double well $f(\phi)$. For some starting volume fraction $\bar{\phi}$, the system relaxes to a minimum free energy state, which is a linear combination of the 2 phases, solution and droplet, corresponding respectively to the left and right wells. a) In the case of an infinite size droplet ($R \rightarrow \infty$), this figure is the well known Maxwell Diagram. The solution is represented by a single line close to the minima of each well, which defines the saturation volume fraction of the system, ϕ^s (shown as green squares). For a finite size drop, b) the minimum volume fractions, ϕ_0 and ϕ_1 , are shifted by a factor dependent on the surface tension and the equilibrium droplet size, the lines through both points are still parallel.

finite size droplets, both ϕ_0 and ϕ_1 are shifted due to the Laplace pressure ($2\gamma/R$) generated by the surface of the droplet, figure 1.7b. Comparison of ϕ^s , and ϕ_0 for a finite size droplet at equilibrium, demonstrates the competing effects between bulk and surface. Although the system may be supersaturated, $\delta > 0$, and thus the lowest energy configuration is a two phase system, formation of a stable droplet phase can only occur by overcoming the destabilizing surface effects, i.e. forming a droplet of at least critical size, where initially δ must be greater than the equilibrium ϕ_0 .

This critical size is a local maximum in the free energy, which can be seen by plotting the free energy for some fixed ϕ_1 (fig.1.8a). Thus equation (1.12) can be solved for the critical size,

$$R_c = \frac{2\gamma}{f(\phi_1) - f(\phi_0) - \mu(\phi_1 - \phi_0)} ; \quad \left(\text{where } \frac{\partial^2 F}{\partial R^2} < 0 \right), \quad (1.16)$$

where μ (without indices) is chemical potential of the system at equilibrium. Using

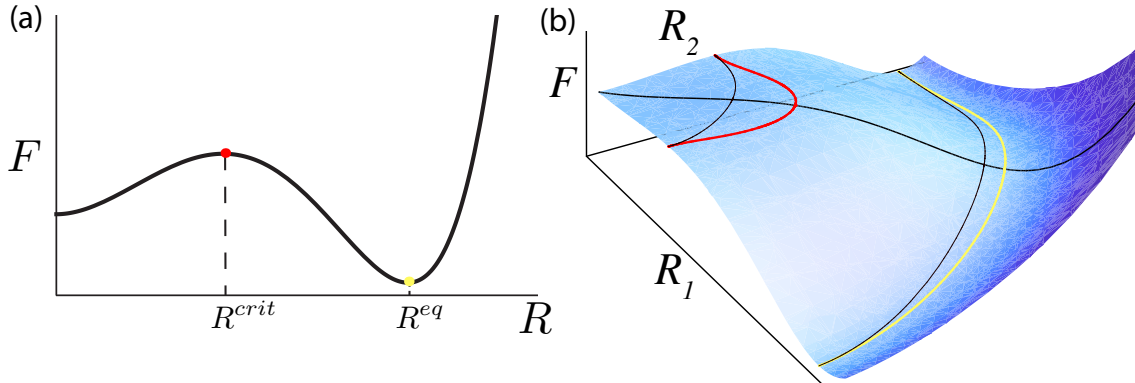


Figure 1.8.: Free energy with respect to drop size, for fixed volume fraction. The red and yellow points(lines) refer to the droplet size(s) at the energy extrema; the critical size and the equilibrium size, respectively. (a): Free energy for a single droplet. The critical size corresponds to the energy barrier that must be crossed to form a stable droplet. (b): Free energy landscape for 2 droplets with sizes R_1, R_2 . The equilibrium size, where the size of both droplets are equal, i.e. $\frac{dF(R,R)}{dR} = 0$, is a saddle point, with ∇F pointing radially, and the global minimum is at $F(R^{eq}, 0)$ and $F(0, R^{eq})$. There is also a saddle point at $F(R^{crit}, 0)$, where ∇F is in the θ direction. This point corresponds to the red point on plot (a), and is lowest energy barrier that must be crossed to form a stable droplet. Black lines correspond to fixed R and θ in polar coordinates to assist in reading the plot.

the same formulation as equation (1.8), one can write the free energy for a two droplet (or multi-droplet) system, $F(\phi_1, \phi_2, R_1, R_2)$ close to equilibrium. Fixing both volume fractions, and plotting the free energy as a function of the two droplet sizes, figure 1.8(b), insight can be gained into the multi-droplet problem. Although there is still a valid equilibrium size, it can be observed that there is a saddle point at the equilibrium size where $R_1 = R_2$. Thus, one can see that a two-droplet system is in fact never stable, and the absolute minimum of the free energy lies at the point where one of the radial coordinates goes to 0. This saddle point is due to the surface tension γ , and for the (hypothetical) case of no surface tension, the minimum of the free energy would in fact be the entire yellow curve in figure 1.8(b). Although this is not as easily shown graphically for the more general multi-droplet case, the fact still holds; due to surface tension, a single droplet is the absolute minimum of the free energy, and thus the lowest energy state of the system.

Kinetics of a Binary Fluid

There is to this to this day no single model that can accurately describe all aspects of first order phase transitions in binary fluids, particularly far away from the critical point. Thus, many phenomenological models exist to describe different aspects of phase transitions away from the critical point, e.g. for spinodal decomposition [31]. In the binodal region, a mean-field approach has been rather successful in describing the kinetics of a binary fluid. As mentioned before, the dynamics of the phase separation of a new “minority” phase can be described by the processes of nucleation

and growth. Nucleation is the formation of a solute droplet of critical size through thermal fluctuations of molecules, and growth is the diffusion limited growth of each droplet by the influx of solute molecules. Using a mean-field approach, the rates for nucleation and growth can be determined with respect to observable thermodynamic parameters and bulk transport coefficients [44].

This system can be described by a general dynamic model with a continuity equation for the probability distribution functional [41],

$$\frac{\partial}{\partial t} \rho(\phi; t) = - \int d^3\mathbf{r} \frac{\delta J}{\delta \phi(\mathbf{r})} \quad (1.17)$$

$$J(\mathbf{r}) = -\nabla \cdot D \nabla \left(\frac{\delta F}{\delta \phi(\mathbf{r})} \rho + k_B T \frac{\delta \rho}{\delta \phi(\mathbf{r})} \right) , \quad (1.18)$$

where $J(\mathbf{r})$ is the probability current, D is the diffusion, which can be dependent on ϕ , and δF is the functional derivative of the coarse grained free energy, which is the aforementioned Landau-Ginzburg free energy, eqn.(1.3). We approximate the probability current to be the first moment of eqn.(1.17) [42]. The density fluctuations in ϕ , which is replaced by a Gaussian noise term in the Langevin formulation, disappears, such that the probability current is

$$J(\mathbf{r}) = -D \nabla^2 \frac{\delta F}{\delta \phi}, \quad (1.19)$$

making the first moment to be,

$$\frac{\partial}{\partial t} \langle \phi(\mathbf{r}) \rangle = \int \delta \phi \phi(\mathbf{r}) \frac{\partial \rho}{\partial t} = \int \delta \phi J(\mathbf{r}) = \nabla \cdot \left\langle D \nabla \frac{\delta F}{\delta \phi} \right\rangle. \quad (1.20)$$

If the distribution in the above equation is infinitely sharp, this equation becomes,

$$\frac{\partial \phi}{\partial t} = -\nabla \cdot \mathbf{j}(\mathbf{r}) \quad (1.21a)$$

$$\mathbf{j}(\mathbf{r}) = -D \nabla \frac{\delta F}{\delta \phi}, \quad (1.21b)$$

which is referred to as the Cahn-Hilliard equation. The local chemical potential is then defined as,

$$\mu(\mathbf{r}) = \frac{\delta F}{\delta \phi(\mathbf{r})}. \quad (1.22)$$

With the addition of Gaussian white noise, due to thermal fluctuations, equation (1.21) is the Langevin equation equivalent to the previously stated mean-field Fokker-Planck formulation, equation (1.17). Without a thermal noise term, the magnitude of the equilibrium order parameter is reduced. Since thermal fluctuations are negligible on the large scale, we can use a renormalized potential which takes into account this reduced magnitude, and continue to work with the “noise-free” Cahn-Hilliard equation [8].

Droplet Nucleation in a Binary Fluid

Nucleation is the formation of a stable new phase, due to concentration fluctuations within the medium. Droplet nucleation in a fluid can be either homogeneous or heterogeneous. In homogeneous nucleation, formation occurs purely through random fluctuations, which bring a sufficient amount of material together such that a stable droplet of critical size is formed. Heterogeneous nucleation, on the other hand, occurs through this localization around some impurity (seed) within the system. Although in real world scenarios heterogeneous nucleation is the more commonly observed phenomenon, with rates orders of magnitude larger than those observed for comparable homogeneous nucleation events [5], only homogeneous nucleation exists in a binary fluid. The theory of nucleation as presented here, is a field theoretic approach, for small supersaturation within a binary fluid. This section is a simplified synopsis of the work of Langer [42], presented in a similar manner as Gunton [31], with recent corrections [30, 57, 72].

To study nucleation, we again consider a quenching experiment: A single phase system at equilibrium which is then quenched into the binodal region, such that the free energy density becomes a double well, and the free energy landscape is similar to the one presented in figure 1.8. Now in a metastable state, the system, without any external forces or internal thermal fluctuations, will stay at its local minimum. The formation of a second state requires that an energetic barrier to be crossed. What is shown in figure 1.8(b), for the two droplet free energy (and implied for multidimensional R -space), is that the point $(R_c, 0)$, is a saddle point in R -space. That is, it is the lowest energy barrier needed to be crossed for the formation of a new droplet. This saddle point does not literally have to be in R -space as shown here, but more generally, in the configuration space of the free energy. The gist of a nucleation field theory is thus, the probability current to cross this saddle point is relative to the probability of nucleation.

The stationary equilibrium solution to the previously stated Fokker-Planck equation, eqn. (1.17), has the form,

$$\rho[\phi] \propto e^{-F[\phi]/k_b T}. \quad (1.23)$$

To create a stable droplet, the probability current must flow through the aforementioned saddle point, ϕ^* . An artificial steady state current is created at ϕ^* by keeping the distribution function at equilibrium on the metastable side of the barrier, and at "0" on the stable side of the barrier. This is done by imposing certain boundary conditions: all drops of larger than R_c are removed as they are created, and the metastable side is continuously replenished. The steady state distribution at the saddle point is then,

$$\rho[\phi] = E[\phi] e^{-F^*[\phi]/k_B T}. \quad (1.24)$$

The free energy can then be expanded about the saddle point, and the steady state flux from equation (1.17) is used to determine ρ in proximity of the saddle point

[42]. This distribution is then used in the full, non-stationary flux equation (1.17), to determine the nucleation rate [58],

$$J = \frac{1}{\tau} \Omega_0 e^{-\Delta F^*/k_B T}. \quad (1.25)$$

The term τ , is the time scale for the macroscopic fluctuations, Ω_0 is the volume of phase space accessible for fluctuations, and $e^{-\Delta F^*/k_B T}$ is the Boltzmann probability factor for the nucleation of a droplet of size R_c .

We can write these quantities in dimensionless variables by using the capillary length l_c , and the characteristic time t_c [58],

$$l_c \equiv (d-1) v^b \gamma / k_B T \quad (1.26)$$

$$t_c \equiv l_c^2 / (D \phi^s v^b), \quad (1.27)$$

where d is the number of dimensions, and D is the monomer diffusion coefficient. The nucleation energy can be written in dimensionless parameters using the time dependent supersaturation, and the dimensionless parameter, $(\delta_0)^{d-1} = v \gamma l_c^{d-1} (\phi_1 - \phi^s) / k_B T$, where $v = \frac{\pi^{d/2} j}{\Gamma(d/2+1)}$,

$$\frac{\Delta F^*}{k_B T} = \left(\frac{\delta_0}{\delta} \right)^{d-1} \quad (1.28)$$

In three dimensions, δ_0 is typically of order one (see Gunton for exact value [31]). The total nucleation rate, per unit time, per unit volume can be written in dimensionless coordinates in three dimensions as [58],

$$J = A \left(\frac{\delta}{\delta_0} \right)^{2/3} \beta \exp \left[- \left(\frac{\delta_0}{\delta} \right)^2 \right], \quad (1.29)$$

where the constants are, $\beta = (1 + \delta/\delta_0)^{3.55}$, and $A = 3(\delta_0)^6 / (4\pi)$.

Growth

After the formation of droplets through nucleation, the minority phase grows in size until the system reaches equilibrium through a process called coarsening. This can occur in two different ways, by coagulation, the fusion of droplets to form larger drops; and droplet growth, the flow of monomer components into droplets. We neglect coagulation and focus on growth.

As mentioned in the prior section, only droplets larger than a critical size grow where the stabilizing bulk phase of a droplet dominates over the destabilizing surface tension. In effect, droplet growth is driven by the curvature of the droplet. Monomers flow into droplets of low curvature, $R > R_c$, and flow out of droplets with a large curvature $R < R_c$. For short times after nucleation, when the level of

supersaturation is high, most droplets tend to be larger than the critical size and grow ⁴.

As the system coarsens, it eventually reaches levels of low supersaturation, where the average drop size, $\langle R \rangle$, continues to increase, while the number of drops, $N(t)$, decreases, through a process called Ostwald ripening. In this regime, larger drops grow at the expense of smaller drops, leaving the systems supersaturation effectively constant. The theory to describe this process, Late Stage Growth (LS growth) was initially developed by Lifshitz and Slyozov [46], and Wagner [80] in the early 1960s. Ostwald ripening has been a heavily studied phenomenon, both experimentally [47] and theoretically [44, 82].

LS theory is one of the few well established theories within first-order phase transitions [31, 43, 82, 45]. It describes the limiting case of small supersaturation, in which the minority phase (droplet) is purely 1 component, and the component of the minority phase tends to zero in the cytoplasm, i.e. $\delta \ll 1$, $\phi_1 = 1$, $\phi_0 \rightarrow 0$. The last condition implies that the droplet density is low enough such that direct droplet-droplet interactions can be neglected. The theory is based on three coupled equations which describe the droplet growth rate $\frac{dR}{dt}$, the time evolution of the distribution function, $f(R, t)$ and the conservation of solute molecules.

LS growth occurs after the formation of the droplet phase, ϕ is close to equilibrium, and thus diffusion gradients are negligible. The diffusion equation, which can be obtained from equation (1.21),

$$\frac{\partial \phi}{\partial t} = D \nabla^2 \phi \quad (1.30)$$

approaches the steady state limit,

$$\nabla^2 \phi = 0. \quad (1.31)$$

At the timescales of interest, the droplet is considered to be spherical due to interfacial tension, and surface fluctuations are negligible. Also, the interior and the exterior of the droplet are considered to be in a local thermodynamic equilibrium, equivalent to the statement that equations (1.11),(1.12) are valid on the interior and exterior boundary of the droplet with some radius R . This local equilibrium fixes the exterior volume fraction, with respect to the equilibrium energy of the system, and the droplet curvature,

$$\phi^R \equiv \lim_{r \rightarrow R^+} \phi(r) = \phi^s + \frac{2\gamma}{R f'' \Delta}, \quad (1.32)$$

where $\Delta \equiv \phi_1 - \phi^s$, and f'' is the curvature of the free energy density at ϕ^s . This is referred to as the Gibbs-Thomson boundary condition. It should be noted that the Gibbs-Thomson boundary condition and the diffusion equation are the

⁴This is statement is somewhat of an over generalization, the regime where all drops grow, is heavily dependent on the nucleation rate, and can be nonexistent in the case where the nucleation sufficiently depletes the supersaturation, see e.g. Sagui et al.[58]

sufficient conditions that induce droplet growth. The curvature, $\frac{1}{R}$, is the driving thermodynamic force, conjugate to the free energy of the surface. This force moves to minimize the surface area, but since drops are already spherical during Ostwald Ripening, material cannot just reorganize on the droplet, but must move through the system to other droplets by diffusion. At steady state, diffusion propagation gives an additional $1/R$ factor. Thus for an overdamped system, where force is proportional to velocity, using phenomenological arguments, one would expect,

$$\frac{dR}{dt} \propto \frac{1}{R^2}$$

and thus the droplet scaling during LS growth would be,

$$R \propto t^{1/3}.$$

To carry out this calculation, we require one additional boundary condition, far from the droplet, ϕ converges to the average cytoplasmic volume fraction,

$$\lim_{r \rightarrow \infty} \phi(r) = \phi_0. \quad (1.33)$$

The radially symmetric steady state solution to the diffusion equation, eqn.(1.31) is,

$$\phi(r) = \phi_0 - \frac{R}{r} (\phi_0 - \phi^R). \quad (1.34)$$

Balancing the flux on both sides of the droplet surface, by setting the steady state diffusion $j(R) = -D\partial_R\phi$ to the droplet growth, gives the deterministic droplet growth rate (see Appendix C),

$$\frac{dR}{dt} = \frac{D}{R} \frac{1}{\phi_1 - \phi^R} \left(\delta - \frac{2\gamma v^b}{R f'' \Delta} \right). \quad (1.35)$$

Setting this equation to zero, one can calculate the time dependent critical radius,

$$R_c(t) = \frac{2\gamma v^b}{f'' \Delta \delta(t)} \quad (1.36)$$

The growth rate is then,

$$\frac{dR}{dt} = \frac{D}{R} \frac{2\gamma v^b}{f'' \Delta (\phi_1 - \phi^R)} \left(\frac{1}{R_c(t)} - \frac{1}{R} \right), \quad (1.37)$$

with respect to the time dependent critical size, consistent with the previously given phenomenological $1/R^2$ behavior. In dimensionless variables, the critical radius, R_c/l_c , is,

$$R_c(t) = \frac{1}{\delta(t)}, \quad (1.38)$$

which shows that the critical size increases and eventually diverges as the supersaturation tends to 0. We define a droplet distribution function, $f(R, t)$, such that for some quantity A , the expectation is,

$$\langle A \rangle = \frac{\int dR f(R, t) A}{\int dR f(R, t)}, \quad (1.39)$$

with the normalization that,

$$\int dR f(R, t) = N(t), \quad (1.40)$$

where $N(t)$ is the total number of drops. From the distribution, we determine the other two equations for LS theory, the continuity equation for the distribution function [46],

$$\frac{\partial f(r, t)}{\partial t} + \frac{\partial}{\partial R} \left(\frac{dR}{dt} f(R, t) \right) = 0 \quad (1.41)$$

and the conservation of particles,

$$\delta + \int dR \frac{4\pi}{3} R^3 f(R, t) = \bar{\phi} V \quad (1.42)$$

From the asymptotic limit of coarsening, the average droplet scales as,

$$\langle R(t) \rangle^3 = \frac{4}{9} D \alpha t \quad (1.43)$$

where $\alpha = 2\gamma/\mu$. This is the same scaling determined through only phenomenological argument. With new work on this scaling behavior [76, 74, 75], the general form of R is determined to be,

$$\langle R(t) \rangle^3 = \langle R(0) \rangle^3 + K(\phi) t \quad (1.44)$$

where $K(\phi)$ is a monotonically increasing function of ϕ , called the coarsening coefficient. Related to the average size, through the conservation equation (1.42), the scaling for the number of droplets follows,

$$N(t) \propto t^{-1}. \quad (1.45)$$

Using the continuity equation, eqn. (1.41), Lifshitz and Slyozov were also capable to calculate an analytical asymptotic distribution function [46],

$$f(R, t) = g(z) / \langle R \rangle^4 \quad (1.46)$$

where the scaled quantity $z = R / \langle R \rangle$ converges as $t \rightarrow \infty$, to the scaled normalized distribution function,

$$g(z) = \begin{cases} \frac{3^4 e}{2^{5/3}} z^2 \exp\left(\frac{-1 - \frac{2}{3}z}{(z+3)^{7/3} (\frac{3}{2}-z)^{1/3}}\right); & z < \frac{3}{2} \\ 0; & z > \frac{3}{2} \end{cases}$$

Quite impressively, this distribution $g(z)$ (figure 1.9) and scalings were calculated prior to the advent of computers, and have been reliably measured in both numerical and experimental settings.

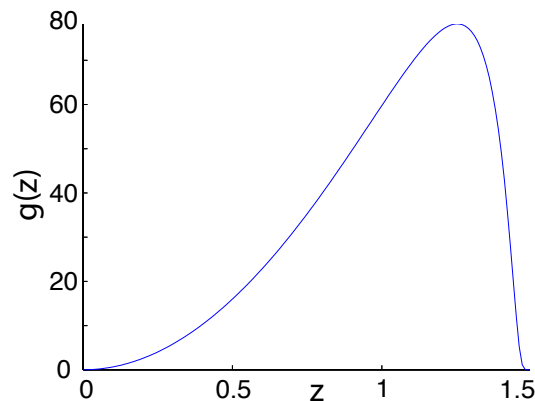


Figure 1.9.: Normalized Scaled distribution function, $g(z)$, from LS theory, where $z \equiv R/\langle R \rangle$ is scaled droplet size.

1.3. Overview of This Work

This work is a theoretical study of how compartmentalization of cellular components occurs within the cytoplasm of a developing embryo with the influence of a protein gradient. A theoretical approach is combined with biological experiments to study a system within the *C. elegans* embryo which use gradients to organize.

In the single cell embryo, a gradient of the protein Mex-5 along the anterior-posterior axis of the cell is required to localize germ granules (referred to as P granules within the *C. elegans*) to one side of the cell. This gradient adds a spatial dependence to the saturation point of a 1st order liquid-liquid phase transition. This spatially changing saturation point, in turn, causes P granules to preferentially condense and grow in the posterior of the cell, while simultaneously shrinking and dissolving in the anterior of the cell.

In chapter 2, we analyze experimental data of P granule behavior in order to identify the driving forces of the segregation process. The data shows the primary factors that lead to P granule localization, liquid properties of the granules, and the spatial effects of the Mex-5 gradient and how it effects P granule growth dynamics.

Based on the experimental data from the prior chapter, a theoretical model for granule segregation is developed in chapter 3. The system is described as a metastable binary fluid which undergoes a 1st order liquid-liquid phase transition. In accordance with prior studies in this field, dynamic equations for granules are given, which include nucleation, diffusion, fusion, and individual granule growth dynamics. An additional level of complexity is added to the system by allowing each term to have either an intrinsic or extrinsic spatial dependence, due to the Mex-5 protein gradient. A mean-field approach is used to analyze the now inhomogeneous background field. This theoretical model is based on previously studied droplet growth models, with the addition of a spatial growth dependence due to the gradient, and the inhomogeneous background field.

To study the properties of the theoretical model, Langevin dynamic simulations were performed. Two new types of behavior are observed due to the spatial gradient: an initial slow growth regime, and a cyclical steady state where nucleation can occur at late times. The analyses of these two behaviors are presented in chapter 4.

In chapter 5, the theoretical model is used to analyze the P granule system. Simulations are performed which emulate P granules at the first and second cell divisions. Through these simulations, the growth behavior of P granules are studied, and better estimations of P granule properties are determined.

The work presented here has been accomplished in close collaboration with experimentalists, whose data and results have heavily influenced and guided the direction of this thesis. Thus, a significant amount of this experimental work has also been included here. All experiments on the P granule system have been performed by Doctor Clifford T. Brangwynne, from the lab of Anthony Hyman, at the Max Planck Institute for Cellular biology and Genetics (MPI-CBG).

2. Germ Granule Segregation in the *C. elegans* Embryo

The segregation of germ granules has been a topic of much interest for scientists since their discovery. In the *C. elegans* worm, germ granules are referred to as P granules. As mentioned in the introduction, the strongest impetus so far to learn more about P granules, has been their localization behavior.

A general overview of the process to be studied is presented in figure 2, which shows an image of the segregation of the P granules (in green) during the 1 cell stage of the *C. elegans* embryo. The times shown are with respect to pro-nuclear meeting (pnm). Initially the maternally derived P granules are evenly distributed throughout the cell. Once the symmetry of the cell is broken, the P granules start localizing to the posterior (right) side of the cell as the maternal and paternal pro-nuclei (red circles) approach each other. A short time after the pro-nuclei have joined, the P granules are completely localized to the posterior side.

In prior works, two processes, which can be complementary, have been proposed to segregate P granules to the posterior side of the cell:

1) After symmetry is broken in the single cell embryo, PAR polarity proteins organize on the cortex of the cell, these PAR proteins induce contractions along the actomyosin cortex which then generate cytoplasmic flow to the posterior of the cell. This flow is then thought to move the germ granules to the posterior side of the cell [34, 33, 11] and 2) The remaining P granules in the anterior of the cell are then degraded or disassembled [33, 11, 14, 68, 83].

Although some evidence for these processes have been observed, they have not been conclusively studied. In this chapter, experimental results are presented giving details of the properties P granules and dynamics of their segregation. This material will then be further utilized in the next chapter to develop a theoretical model of germ granules.

This chapter is heavily based on the paper by Brangwynne et al., 2009 [6]. All experiments were performed by Dr. Clifford T. Brangwynne.

To observe the size and position of P granules, experiments were performed which entailed the observation of the protein PGL-1, tagged with green fluorescent protein (GFP::PGL-1). As PGL-1 is a constitutive component of P granules [36, 37], it is reasonable to assume that the granules follows similar dynamics as PGL-1. Typically one should perform correlation experiments to demonstrate that the GFP intensity is in fact proportional to the protein concentration. These experiments, in vivo, can be disproportionately demanding, and so are often not, or cannot be, done. To vindicate

the assumption that GFP correlates with PGL-1, and that PGL-1 correlates with P granule size, similar experiments were performed using other essential P granule proteins, e.g. GFP::GLH-1 [6].

2.1. Mechanism of Localization

The bulk cytoplasm can be considered an incompressible fluid. This entails that the divergence of the velocity field must vanish: $\nabla \cdot \vec{v} = 0$, where \vec{v} is the velocity field of the bulk cytoplasm. As a consequence of this incompressibility, cytoplasmic material that flow into the posterior of the cell must also be accompanied by an equal amount of flow out of the posterior, to ensure conservation of volume. This means that any flow of material which segregates due to the bulk flow, must exhibit deviations from the cytoplasmic flow field, i.e. if P granules localize to the posterior by flow, they must exhibit different flow behavior as compared to the bulk cytoplasm, possibly due their binding of local posterior structures.

Movies of the cell cytoplasmic flows were made using differential interference contrast (DIC) microscopy (see fig.2.2 left), the bulk flow fields were measured using particle imaging velocimetry (PIV). Comparison of bulk field flow and P granule flow (fig.2.2 right) show similar behavior. Measurements were also made using 3D particle tracking of fluorescently labeled P granules (GFP::PGL-1), shown in figure 2.3. Again, in a similar fashion to the cytoplasmic bulk flow, granules flow to the posterior in the interior of the cell and flow back to the anterior in the region close to the cortex (fig.2.3b), exhibiting no net movement of P granules (fig.2.3c). Even though granules are affected by advection, there appears to be no net flux of P granules due to cytoplasmic flow, thus making it an unlikely cause for P granule segregation.

In addition to experiencing advective motion, P granules undergo dynamic changes of size. Figure 2.4 shows the growth dynamics P granules. Each trajectory represents the size of an individual P granule, where the color denotes its spatial position. The

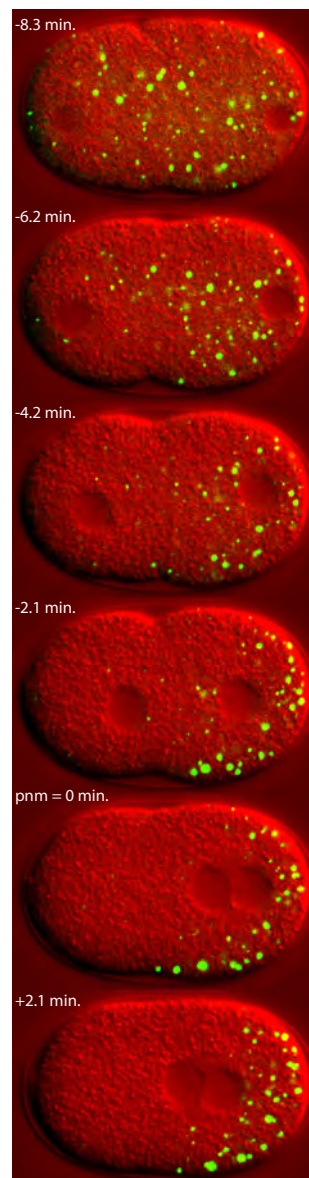


Figure 2.1.: P granule segregation in the 1 cell stage of the *C. elegans* embryo. GFP labeled PGL-1 (green), a P granule protein, overlaid on a DIC image (red). Time is with respect to pnm. Brangwynne et al.(2009)

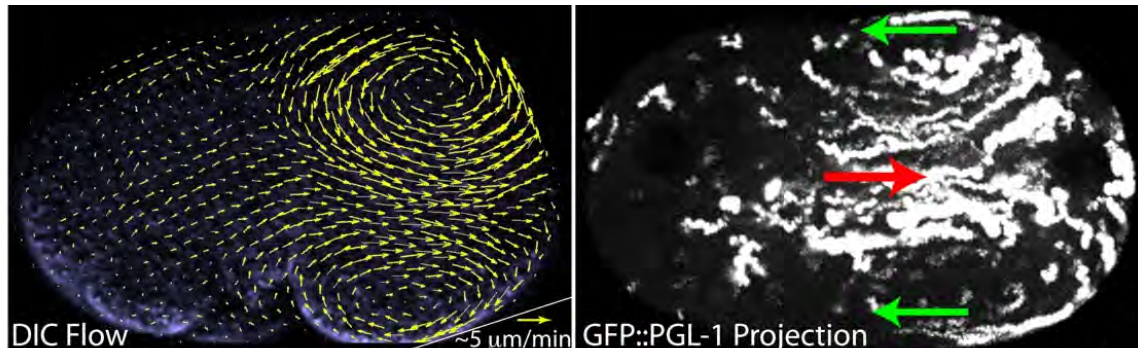


Figure 2.2.: Flow fields: (left) DIC image with bulk cytoplasmic flow, the 2-D vector field is generated using PIV tracking, as compared to (right) P granule flow: Maximum intensity projection of confocal stacks of GFP::PGL-1, P granules, in the one cell embryo during symmetry breaking; first frame -8.12 minutes pnm, last frame -3.5 minutes pnm. P granules in center move towards the posterior (red arrow), and P granules near the cortex move towards the anterior (green arrows). GFP::PGL-1. Brangwynne et al.(2009)

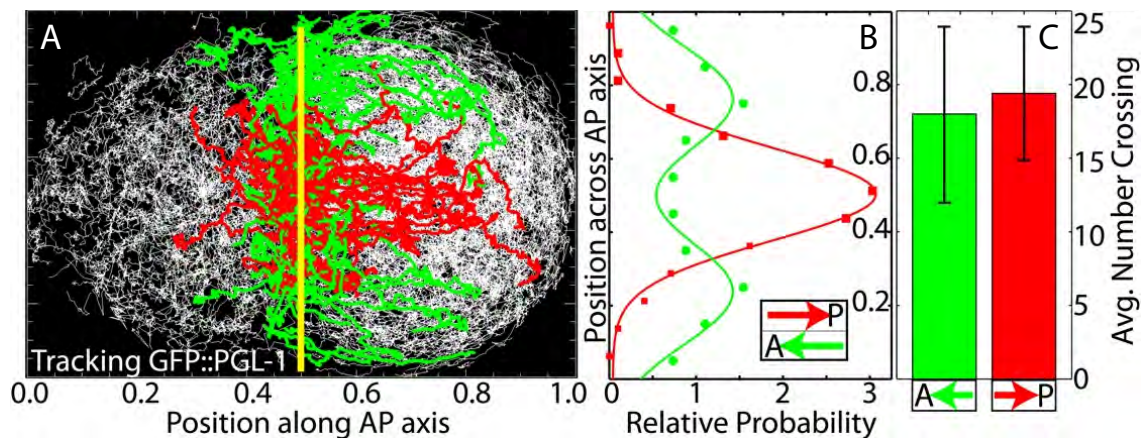


Figure 2.3.: 3D particle tracking of P granules. A) Overlay of P granule trajectories (white) from five GFP::PGL-1 embryos. Trajectories that cross the midplane (yellow line) into the posterior are marked in red, while into the anterior are marked in green. B) Probability distribution of the location perpendicular to the AP axis of P granules crossing the midplane into the anterior (green) vs. the posterior (red). P granules tend to move from the anterior to the posterior in the center of the cell, while they move in the opposite direction closer to the boundary of the cell. C) The average flux per embryo. $N = 5$, error bar shows the standard error of the mean. Brangwynne et al.(2009)

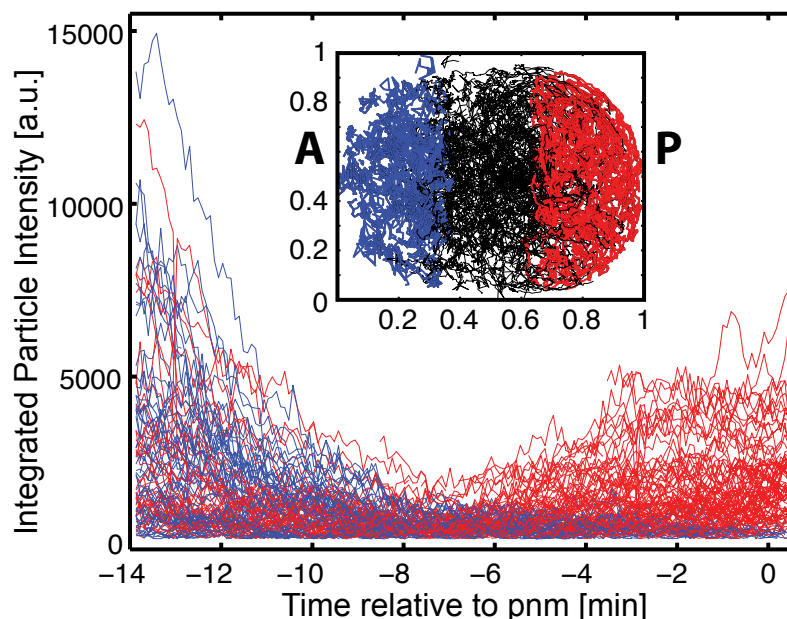


Figure 2.4.: Tracking the sizes of individual P granules. Trajectories correspond to the integrated particle intensity (GFP::PGL-1) of distinct P granules over time. Colors refer to the location of the P granule within the embryo; blue are ones in the anterior, black is from the center (omitted for clarity), and red are P granules in the posterior. Brangwynne et al.(2009)

total integrated intensity of GFP::PGL-1 within the granule is plotted as a function of time. Assuming that the total integrated intensity GFP::PGL-1 is proportional to the size of the P granule, the plot shows the relative size of individual P granules. Prior to the symmetry breaking of the cell, all granules decrease in size. At approximately 6.5 minutes prior to pnm the dynamics change; as the granules in the anterior of the cell continue to shrink, the ones in the posterior start to grow, i.e. P granules initially exhibit uniform diminution, but then convert to a state where they exhibit asymmetric growth.

By measuring the average P granule material in each region (figure 2.5), one sees that P granule material throughout the cell (in cytoplasm and P granules) is initially homogeneous, and continues to be so throughout the period that P granules exhibit uniform diminution. Once P granules exhibit asymmetric growth, P granule material becomes localized to the posterior and depleted in the anterior. Binning granules with respect to their position along the AP-axis, one sees (see red curve, fig. 2.6) a net growth of P granules in the posterior and a net decay in the anterior of the cell. This data suggests that localization of P granule material to the posterior is associated with asymmetric growth.

Disruption of gene activity through RNA interference (RNAi) is a useful tool to perturb biological processes. The relationship between growth and flow are further examined by RNAi. Both PAR-1 and SPD-5 are essential proteins involved in symmetry breaking of the cell. Generation of cytoplasmic flows and the transi-

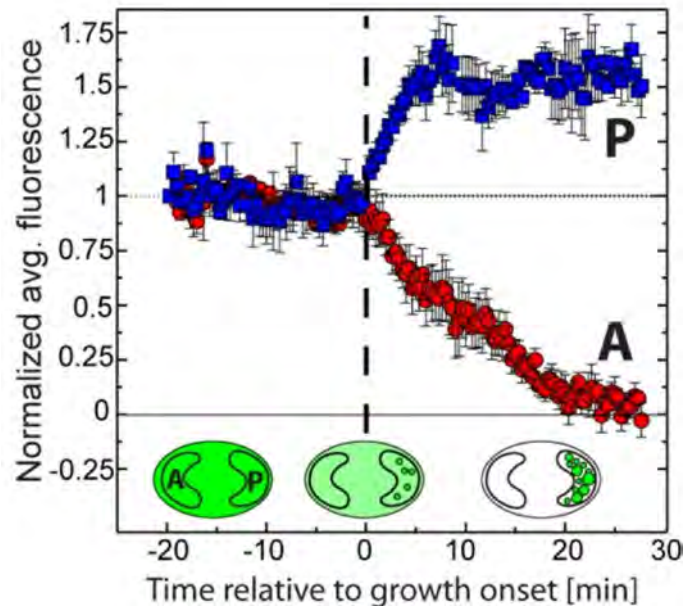


Figure 2.5.: Average fluorescence intensity of GFP::PGL-1 in the anterior and posterior of the cell over time, with respect to the onset of asymmetric growth (shown in figure 2.4), Data is normalized by the initial values of each region. Brangwynne et al.(2009)

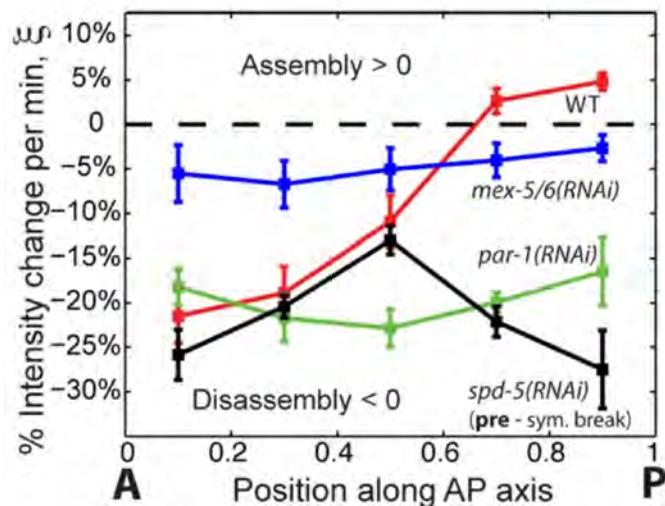


Figure 2.6.: Intensity change of GFP::PGL-1 (growth rate) as a function of position. The cell is binned into 5 equal bins along the AP axis. Data is shown for the wild type (red), and several RNAi conditions noted on the figure. Brangwynne et al. (2009)

tion of P granules from uniform diminution to asymmetric growth, are events that require symmetry breaking, and are thus prevented by RNAi of either protein. Figure 2.6 shows the growth rate of P granules for different RNAi conditions. Both *par-1*(RNAi) (green) and *spd-5*(RNAi) (black) show that P granules continue to decrease in size across the entire cell, as compared to the wild type (red) for the same time, which undergoes asymmetric growth. Interestingly, there is a delightful nuance to *spd-5*(RNAi) which provides an additional detail to the P granule localization problem. As opposed to *par-1*(RNAi), which completely abolishes symmetry breaking, *Spd-5*(RNAi) only delays it. This delay allows for all granules to shrink until they completely disappear. Once symmetry breaking does occur, a delayed growth phase is observed in which there is de novo formation and growth of P granules the posterior of the cell. *spd-5*(RNAi) exhibits a much sharper initial growth rate (fig. 2.7), which then slows down and exhibits behavior similar to the wild type. Delayed symmetry breaking by *spd-5*(RNAi) suggests that flow is not necessary for P granule localization, and that preferential formation and growth is sufficient to accomplish the task. This reinforces the prior experiments; P granules and P granule material localizes to the posterior of the cell through spatially preferential growth of P granules, where advection has a negligible effect on the process.

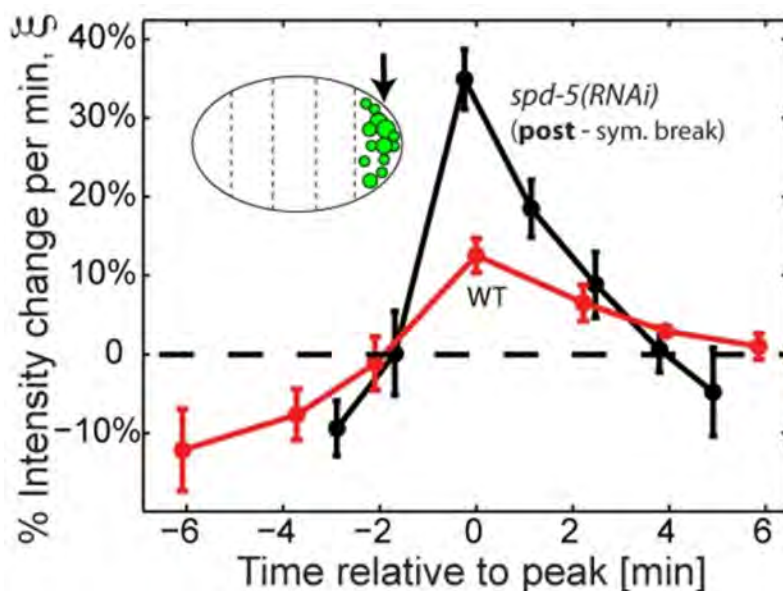


Figure 2.7.: % Intensity change (growth rate) of GFP::PGL-1 in the posterior of the cell after symmetry is broken, wild type (red), and *spd-5*(RNAi) (black). Brangwynne et al.(2009)

2.2. Properties of Germ Granules

With a reasonable understanding of the dynamics of the P-granules, one must now dive into the physical properties of these membrane-less organelles to gain further insight in to how localization of P granule material can occur through growth, and to determine physical parameters which will be of interest to the theory presented in the next chapter.

P granules exhibit liquid droplet like properties in a system with shear induced flow (see supplemental material of [6] for movies): Individual P granules appear round, when two of them fuse (which is commonly observable), the new, larger P granule rounds out to a spherical shape. In later cell stages, when P granules localize to the surface of the nucleus, they exhibit wetting behavior. In the induced flow system, they can be seen “de-wetting” from the nucleus and even the fission of two smaller spherical P granules can be observed.

As this thesis is more focused on the theoretical study of P granules and their dynamics, details of additional experiments demonstrating the liquid droplet like properties of P granules will not be presented here, only the basic elements have been presented to be incorporated into the theory. The reader is encouraged to reference Brangwynne et al. [6] for a more comprehensive analysis of the subject.

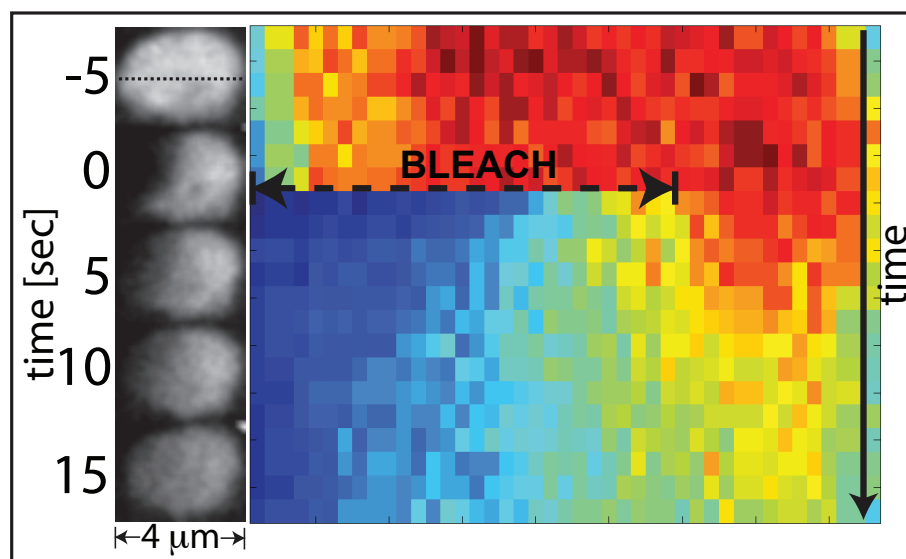


Figure 2.8.: Photo Bleaching of a P granule which is attached to the nucleus of the cell at the 8 cell stage, and kymograph of its recovery. Brangwynne et al. (2009)

2.2.1. Diffusion of Granule Components

Using FRAP (Fluorescence Recovery After Photo-bleaching) of GFP::PGL-1 within the P granule, the fluorescence recovery time, τ , the elapsed time required for the

photo intensity of the area to recover half of its original intensity, was measured (see figure 2.8). With the relation, $D = \mathcal{A}/\tau$ where \mathcal{A} is the area which was photo-bleached, the diffusion coefficient of GFP::PGL-1 was determined, $D \approx 2\mu m^2/s$.

Using tracking data, the mean squared displacement of P granules of different intensities were measured (figure 2.9), as per the method described in appendix A. Using a linear fit, the diffusion coefficient of each set of intensities was determined.

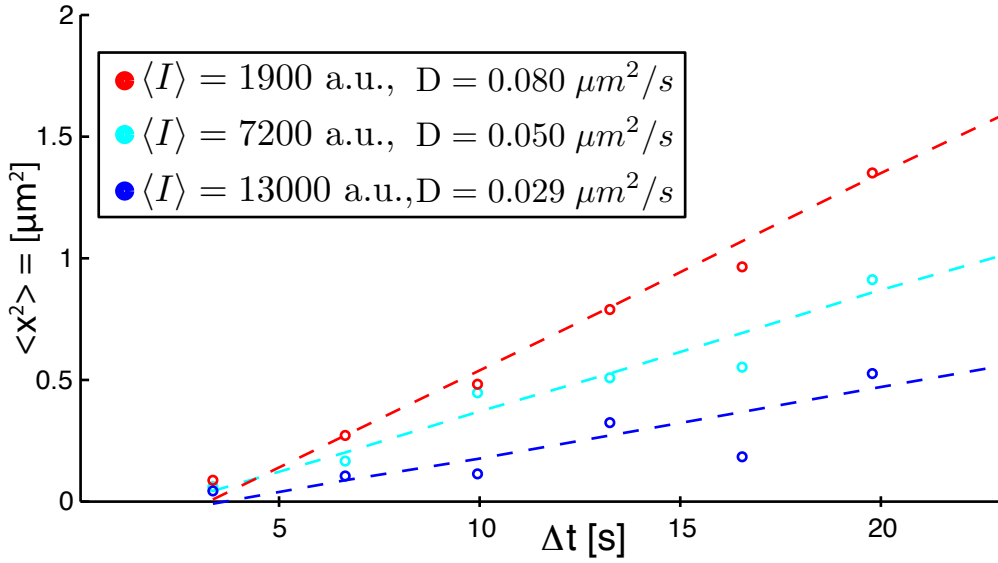


Figure 2.9.: Diffusion of P granules. Measurement of the mean squared displacement of P granules of different intensities. P granules were binned with respect to their effective intensity (see appendix A.2). Only the three smallest (of 10) bins are shown, since there were not a sufficient number of P granules in the larger bins to quantify. The standard deviation for each point is between 200% – 400% of the mean value, error bars were left out for the purpose of clarity.

Due to the lack of sufficient experimental data, this comparison of diffusion coefficients is more a qualitative comparison. Considering this, and the assumption that the intensity is proportional to P granule volume, the data still supports the observation that P granules are in fact spherical, where their diffusion appear to obey the Stokes-Einstein relation, i.e. $D \propto \frac{1}{R}$; or more specifically, $(\langle I \rangle^{1/3} \cdot D) \approx \text{constant}$.

Applying the Stokes-Einstein relation in the same manner to see what size a P granule with the diffusion coefficient of Pgl-1 ($2\mu m/s$) would have, we see that it would be roughly 100th the size of the smallest observed P granules. The smallest observed granules are within the order of $.1 - 1\mu m$, this places Pgl-1 at the $1 - 10nm$ scale. For a 700 amino acid long protein, this is reasonable.

2.3. Effects of the Mex-5 Protein Gradient on Growth

What causes P granules to initially shrink, and what then causes them to later grow asymmetrically? Mex-5 is an RNA associated protein that is known to co-localize with P granules [22]. Concurrent with the change of growth behavior and localization of P granules, Mex-5 undergoes a transition where it is initially homogeneous throughout the cell, to forming a gradient across the embryo (fig.2.10). The formation of this gradient is particularly interesting, considering that there is

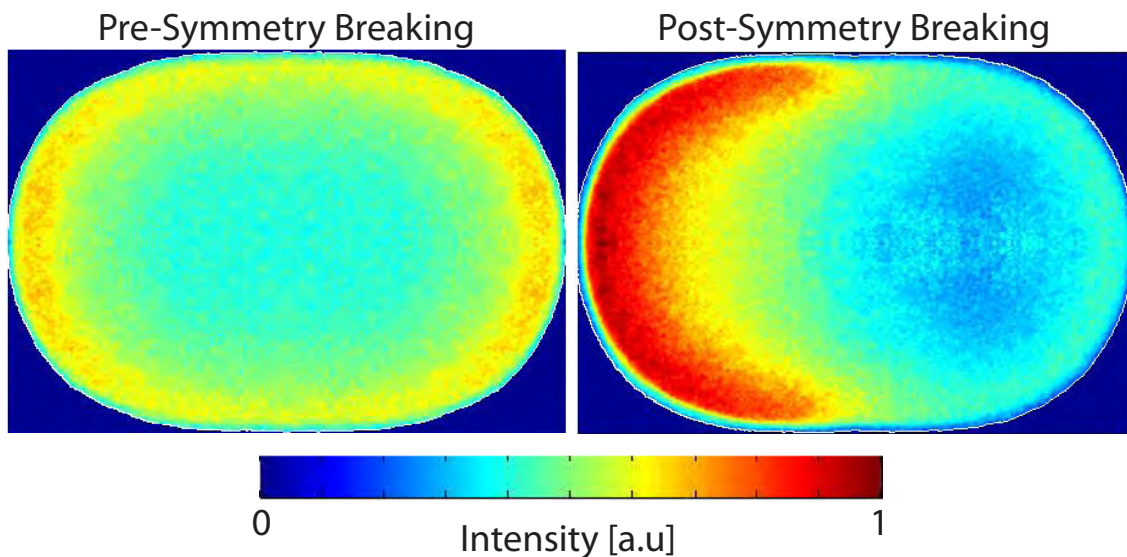


Figure 2.10.: Mex-5::GFP intensity profile. Prior to symmetry breaking, (left) Mex-5 is homogeneous throughout the cell. After symmetry breaking (right), Mex-5 has a concentration gradient, with high concentration in the anterior of the cell. C.P.Brangwynne

no source (protein translation) or sink (protein degradation) at work so early on in embryogenesis. It has been shown that this gradient can form with a diffusion reaction mechanism, where there exist two forms of Mex-5 with different diffusion coefficients [28]. There is a slowly diffusing Mex-5, which once phosphorylated converts into a fast diffusing protein. It has been suggested that this could be due to the unphosphorylated form interacting with the cytoskeletal structure of the cell, or other large molecular complexes to effectively lower the diffusion of Mex-5 [73].

Allowing the embryo to undergo symmetry breaking, but preventing the formation of the Mex-5 gradient by RNAi (blue curve fig.2.6), also prevents P granules to transition to asymmetric growth. Uniform diminution continues in a similar manner as if symmetry breaking never occurred. Thus the Mex-5 gradient is necessary for P granule asymmetric growth. We postulate that the Mex-5 directly effects the stability of P granules, and that higher concentrations Mex-5 allows P granules to break down within the cytoplasm, while at lower concentrations, where Mex-5 localization to P granules is still observed, the concentration is not sufficiently to

induce their breakdown.

2.4. Chapter Summary

In conclusion, P granules are liquid like droplet structures which travel through the cytoplasm by advection and diffusion. P granules that touch, can fuse into a single larger droplet (rounded) body. Through induced shear, they can also fission into smaller droplets.

Although affected by convection, P granules localization occurs through their asymmetric growth. Initially they are found in uniform concentrations throughout the cell and decreasing in size, but certain mechanisms cause the P granules to preferentially form and grow in the posterior while simultaneously diminishing in size in the anterior. This asymmetric growth leads to the localization of both P granules and the P granule material into the posterior of the cell.

As one would expect, P granules diffuse slower with size. This appears consistent with the Stokes-Einstein relation, although this has not been clearly proven and needs to be further explored.

It is believed that this preferential growth is induced by the Mex-5 gradient. Mex-5 is a protein that co-localizes with P granules, while also forming a gradient across the long axis of the embryo. The gradient formation is concurrent with the asymmetric growth of P granules. Prevention of the formation of this gradient also prevents the transition of P granules into their asymmetric growth phase, which thus prevents their localization. Mex-5 is a likely candidate as the protein which directly induces this asymmetric growth, by possibly stabilizing interactions with the cytoplasm at higher concentrations, allowing P granules to dissolve.

3. Droplet Kinetics in Presence of a Gradient

In this chapter, a theoretical model that can describe the aggregation of germ granules in the single-cell embryo is developed, the gradient droplet growth model. In a similar manner as presented in the introduction, section 1.2.1, a binary fluid droplet growth model will be developed in a stepwise manner that can describe the dynamics of interest within germ granules. Although this theory is presented in a similar fashion as the introduction, two key assumptions are avoided here that make this theory distinct: the droplet volume fraction is not fixed, allowing for fluctuations in droplet densities, and the external volume fraction is not uniform, allowing for spatial inhomogeneities that can affect growth.

The basis of the theory is a binary fluid model, which allows for the general properties experimentally observed for P granules from the prior chapter: this binary fluid undergoes a first-order phase transition, from a single mixed cytoplasmic state, to a metastable 2 phase state; consisting of the cytoplasm and droplet like germ granules.

New also to this model, is a spatially dependent saturation point. The saturation point, which defines the phase boundaries and effects both growth and nucleation, is allowed to change to emulate the effects of the Mex-5 cellular gradient (see section 2.3), i.e. spatially control phase transition and growth. This addition to previously studied droplet growth models allows for inhomogeneous growth and localization of the granule droplets, which in turn create a non-homogeneous diffusive monomeric background field, in contrast to a homogeneous field. In addition, spatial dependence of the saturation point prevents the system from relaxing to equilibrium, leading to a final oscillatory non-equilibrium steady state (see next chapter).

3.1. The Cytosol as a Binary Fluid

As mentioned in the introduction, the single cell *C. elegans* embryo is surrounded by a rigid shell. Although there are some fluctuations in the size of the single cell within the shell, these are relatively small as compared to the cell size; the fluctuations are thus considered negligible, and the system volume, V , is constant. The system is considered to be made up of two components: component a is the solution (or cytoplasmic component), and component b is the solute (or germ granule component). Since no protein synthesis or degradation occurs in early embryogenesis[78], the

number of molecules of each component, N^a, N^b , is conserved. Making the common approximation that the system is an incompressible Newtonian fluid ¹, the volume fraction of component b ,

$$\phi \equiv \frac{N_i^b v^b}{V_i}, \quad (3.1)$$

in some volume V_i , is sufficient to describe the concentrations of both a and b , where v^b is the molecular volume of component b . The volume fraction of the system, $\bar{\phi}$, is then a fixed constant, which can be used in place of the total number of molecules of each component, N^a, N^b , and with the system volume, V , defines the global parameters of the system.

From this point on, the P granule system lends itself quite naturally to a droplet growth model. Monomer components of a and b both diffuse and are carried by cytoplasmic flows within the cell. Although these flows do definitely carry monomer components, cytoplasmic flow is considered negligible because there is no net flow of material (see section 2.1). Prior to symmetry breaking, P granules are observed throughout the cell, the system is undersaturated, and thus P granules dissolve throughout the system. After symmetry is broken, nucleation events and granule growth are observed in the posterior, while simultaneous dissolution is observed in the anterior. The system is observed to fluctuate between undersaturated and supersaturated, but it does not give the appearance of undergoing any type of spinodal decomposition. That is, when ϕ is below the saturation point ϕ^s , droplets dissolve, and when above ϕ^s , droplets condense (grow) and nucleation of new droplets occurs. The cytoplasmic volume fraction is never so large as to cause it to undergo spinodal decomposition, and thus the system is always either in the single phase or binodal region. Figure 3.1 shows an illustration of where the cell is hypothesized to lay on the phase diagram. Since we are only interested in de-mixing of the cytosol, which is “ ϕ poor” (see next section), the value of ϕ^s is uniquely defined by the left side of purple coexistence curve for a fixed position along the cell.

3.2. Single Droplet Growth Dynamics

Considering convection negligible, we start with the Cahn-Hilliard equation (1.21),

$$\frac{\partial \phi}{\partial t} = \nabla \cdot \left(D \nabla \frac{\delta F}{\delta \phi} \right), \quad (3.2)$$

which describes the dynamics of the system, where D is the monomer diffusion coefficient of the granule component. The Ginzburg-Landau free energy,

$$F[\phi] = \int d^3x \left(\frac{1}{2} (\nabla \phi)^2 + f(\phi) \right), \quad (3.3)$$

describes our two phase system consisting of droplet and solution.

¹Incompressibility is defined here such that the molecular volumes, v^a, v^b , are constant.

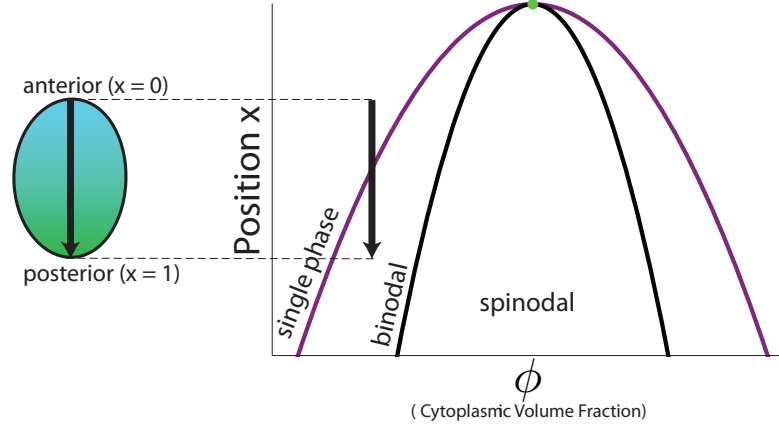


Figure 3.1.: Phase diagram for a binary fluid, with the volume fraction ϕ as the order parameter. An illustration of where the germ granule system lies in the phase diagram is also shown. The region between the purple and black line represents the binodal region, and the interior of the black line is the spinodal region. The cell lies along the black arrow. Due to the spatial protein gradient within the cell, there is a position dependent “quench” along the long axis of the cell, causing the anterior of the cell to be in a single state, while the posterior is in a mixed, metastable, state. The green point refers to the critical point, which is assumed to be far from the germ granule system.

For a bistable system, the free energy density, $f(\phi)$, is required to be a double well potential. In this case, the left and right well describe the energy of the cytoplasm and droplet respectively (see section 1.2.1). The specific form of $f(\phi)$ will be discussed later (section 3.4.1), where spatial dependence will also be introduced. This free energy describes a two-phase system with the volume fraction as the order parameter for a first order transition between a droplet phase, considered ϕ “rich”, and a cytoplasmic phase, considered ϕ “poor”.

As presented in the introduction, for small supersaturation, gradient terms are considered negligible in the bulk of the free energy, and the droplet interface is replaced by the surface tension parameter γ , in the free energy,

$$F[\phi] = \int d^3r f(\phi) - \gamma \int_{Interface} d\mathcal{A}. \quad (3.4)$$

For a single spherical droplet with radius R and volume fraction ϕ_1 , where ϕ for each phase is relatively homogeneous, the free energy can be written,

$$F(\phi_1, R) = V_0 f(\phi_0) + 4/3\pi R^3 f(\phi_1) - 4\pi R^2 \gamma. \quad (3.5)$$

The system is closed, with volume, V , and initial volume fraction $\bar{\phi}$. Conservation of the number of particles and conservation of volume, requires that the cytoplasmic size and volume fraction be dependent variables,

$$V_0 = V - 4/3\pi R^3, \quad (3.6)$$

$$\phi_0 = (\bar{\phi} V - \phi_1 4/3\pi R^3) / V_0. \quad (3.7)$$

For the dynamics, the concentration field can be described by the diffusion equation,

$$\frac{\partial \phi}{\partial t} = D \nabla^2 \phi. \quad (3.8)$$

Although the system is not at equilibrium, as per the Gibbs-Thomson condition, the interior of the droplet, and directly outside of the droplet are assumed to be at a local equilibrium at all times. The volume fraction of the interior, ϕ_1 and directly exterior $\phi^R \equiv \phi_0(r \rightarrow R^+)$, are governed by the equilibrium conditions,

$$\frac{\partial F}{\partial \phi_1} = 0 \quad (3.9)$$

$$\frac{\partial F}{\partial R} = 0 \quad (3.10)$$

which imply,

$$0 = \left. \frac{\partial f}{\partial \phi} \right|_{\phi=\phi_1} - \left. \frac{\partial f}{\partial \phi} \right|_{\phi=\phi^R} \quad (3.11)$$

$$\frac{2\gamma}{R} = f(\phi_1) - f(\phi^R) - (\phi_1 - \phi^R) \left. \frac{\partial f}{\partial \phi} \right|_{\phi=\phi_1}. \quad (3.12)$$

The saturation volume fraction of the cytoplasm, ϕ^s (saturation point), is defined in a similar manner as ϕ^R for the case $R \rightarrow \infty$, in equation 3.12. Figure 1.7 illustrates graphically how ϕ^s (left figure) and how ϕ^R, ϕ_1 (right figure) are determined. The saturation point is a property of the system, while ϕ^R, ϕ_1 are set by the curvature of the droplet, $\propto 1/R$.

Droplets larger than some critical size $R > R_c(t)$ grow, while droplets smaller than R_c undergo diminution. We assume that droplet growth is a relatively slow motion of interest, as compared to the relaxation of ϕ . We thus make the quasi-stationary approximation, that in addition to the local equilibrium between the interior and exterior of the droplet, the background field outside of the droplet relaxes to a steady state, and the interior of the droplet has a homogeneous. The background field is then,

$$\phi(r) = \begin{cases} \phi_1; & r < R \text{ (drop)} \\ \phi_0 - \frac{R}{r} (\phi_0 - \phi^R); & r > R \text{ (cytoplasm)}, \end{cases} \quad (3.13)$$

where cytoplasmic volume fraction is the radially symmetric steady state solution of eqn.(3.8), with Dirichlet boundary conditions,

$$\lim_{r \rightarrow R^+} \phi(r) = \phi^R \quad (3.14a)$$

$$\lim_{r \rightarrow \infty} \phi(r) = \phi_0. \quad (3.14b)$$

The interior boundary condition is the aforementioned Gibb-Thomson local equilibrium, and ϕ_0 is the time dependent average volume fraction of the solution phase.

In addition to the diffusion of the monomer background field, the finite size droplet is also considered to diffuse as a single body. Using the Stokes-Einstein relation,

$$D(R) = \frac{k_B T}{6\pi\eta R}, \quad (3.15)$$

where η is the viscosity of the medium, we see that droplet diffuse proportionately to size, as the droplet diffusion coefficient decreases with drop radius. Thus the droplet's diffusion coefficient is,

$$D(R) = \left(\frac{3v^b}{4\pi}\right)^{1/3} \frac{D}{R}. \quad (3.16)$$

where $D(R) \propto 1/R$, as compared to the monomer diffusion coefficient D . Droplet diffusion is thus considered negligible with respect to droplet growth, since growth occurs on the order of monomer diffusion.

Balancing the interior and exterior of the droplet by setting the change of droplet size, $(\Delta\phi)dR/dt$, equal to the outside diffusion flux, $J(R) = -D\nabla\phi|_{r=R}$, determined from eqn.(3.13), a dynamic equation for growth is determined,

$$\frac{dR}{dt} = \frac{D}{R} \frac{\phi_0 - \phi^R}{\phi_1 - \phi^R}. \quad (3.17)$$

The droplet growth is proportional to monomer diffusion, and dependent on the local volume fractions, ϕ_1 , ϕ^R , and the background volume fraction, ϕ_0 . Figure 3.2 shows these volume fractions in the neighborhood of a single droplet in a supersaturated medium.

In most studies of droplet growth, as per LS theory (see section 1.2.1, the droplet phase is considered to be constant and just pure granule component. This simplifies analytical calculations, since the prior energy minimization with respect to volume fraction becomes only an energy minimization of the cytoplasmic phase. For this work, the volume fraction of the droplet phase is allowed to vary; for simulation purposes a full minimization is carried out, and eqn.(3.17) is used for droplet growth. But a good deal of insight into the workings of the droplet model can be gained by fixing the droplet volume fraction. To simplify analytical calculations, and to gain a simpler physical understanding of the system, for the rest of this section the free energy density of the droplet phase is considered sharply peaked about ϕ_1 , such that as a first order approximation, ϕ_1 , and thus $f(\phi_1)$ are fixed for all minimizations.

For fixed ϕ_1 , eqn.(3.12), the surface volume fraction can then be written with respect to the saturation volume fraction,

$$\phi^R = \phi^s + \frac{2\gamma}{\mu R}. \quad (3.18)$$

Substituting in the supersaturation of the solution phase, $\delta \equiv \phi_0 - \phi^s$, a time dependent critical radius is determined by setting eqn.(3.17) to zero,

$$R_c = \frac{2\gamma}{\delta}. \quad (3.19)$$

As expected, the critical radius diverges as the supersaturation goes to zero. The droplet growth can then be written with respect to the critical size as,

$$\frac{dR}{dt} = \frac{D}{R} \frac{2\gamma}{\Delta\phi\mu'} \left(\frac{1}{R_c} - \frac{1}{R} \right), \quad (3.20)$$

where $f'' = \frac{\partial^2 f}{\partial \phi^2}$ is the curvature of the energy at the saturation point. It can thus be

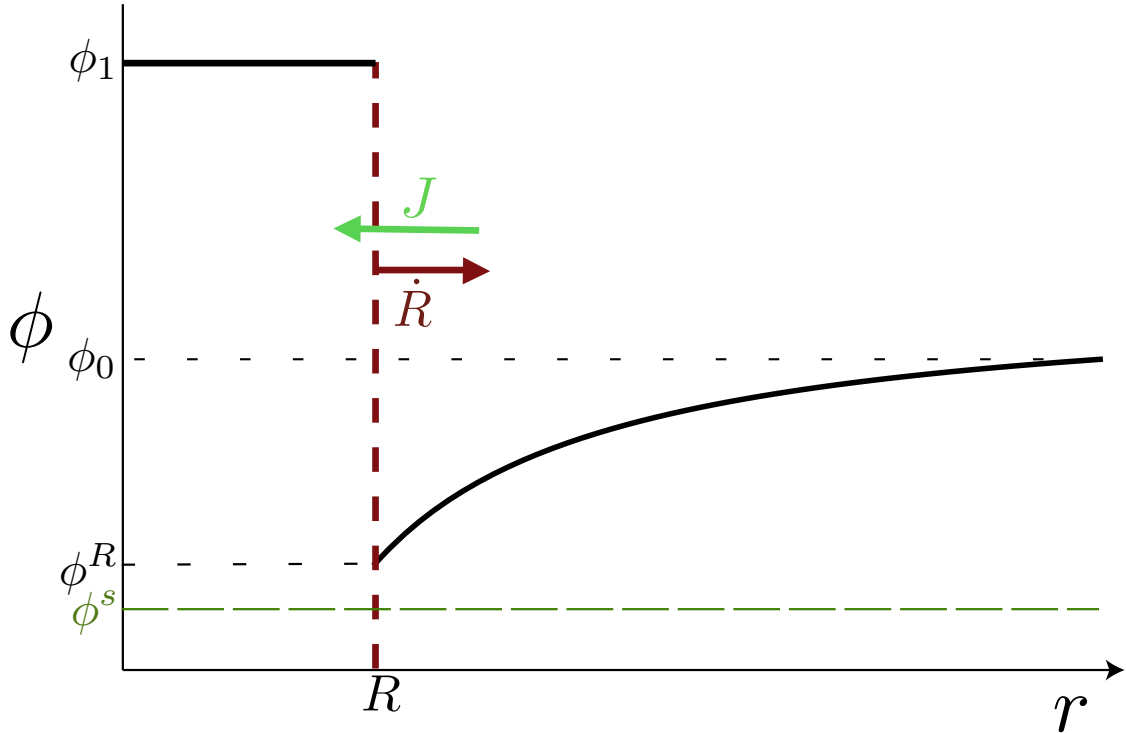


Figure 3.2.: Illustration of volume fraction distribution, going radially outward from the center of a growing droplet of radius R . The droplet interior has a uniform volume fraction, ϕ_1 . The volume fraction directly outside of the droplet, ϕ^R , is in equilibrium with the interior of the droplet. ϕ then quickly plateaus to the average volume fraction ϕ_0 . The growth of the droplet is driven by the diffusion flux from the outside of the droplet, $\dot{R} \propto D(\phi_0 - \phi^R)$.

seen that droplets below a critical size, $R < R_c$, shrink, while droplets larger than R_c grow, due to the volume fraction flux outside of the droplet (figure 3.2).

For a supersaturated medium, $\delta > 0$, there is a probability, due to density fluctuations, that monomer components collude to one local region to spontaneously form a droplet. One can calculate the energy required for this event to occur, and thus form a new drop of size V^* ,

$$\Delta F(V^*) \equiv F_{new} - F \quad (3.21)$$

$$= V_0^* f(\phi_0^*) + V^* f(\phi^*) + \gamma S^* - V_0 f(\phi_0), \quad (3.22)$$

where all starred quantities refer to quantities after the new drop has formed. The new dependent variables are,

$$V_0^* = V_0 - V^* \quad (3.23)$$

$$\phi_0^* = (V_0\phi_0 - V^*\phi^*)/V_0^*. \quad (3.24)$$

The free energy has a maximum at $R = R_c$, the critical size. Thus, ΔF has a maximum at $R^* = R_c^*$ which is the critical size after the formation of a new droplet (see section 1.2.1). The probability per unit volume per unit time of creating a stable droplet ($R^* > R_c^*$) is given by equation (1.29). Since this rate is valid only for small supersaturation, the coefficients for the rate are allowed to be free parameters, and the nucleation rate per unit volume is approximated by a Kramer's rate,

$$J_0 = \alpha e^{-\Delta F(R^*)/k_B T}, \quad (3.25)$$

where α and $k_B T$ are parameter that are chosen to reflect observations from experimental results, and $\Delta F(R^*)$ is the change in free energy to form a droplet of critical size.

3.3. Dynamics of the Model for Multiple Droplets

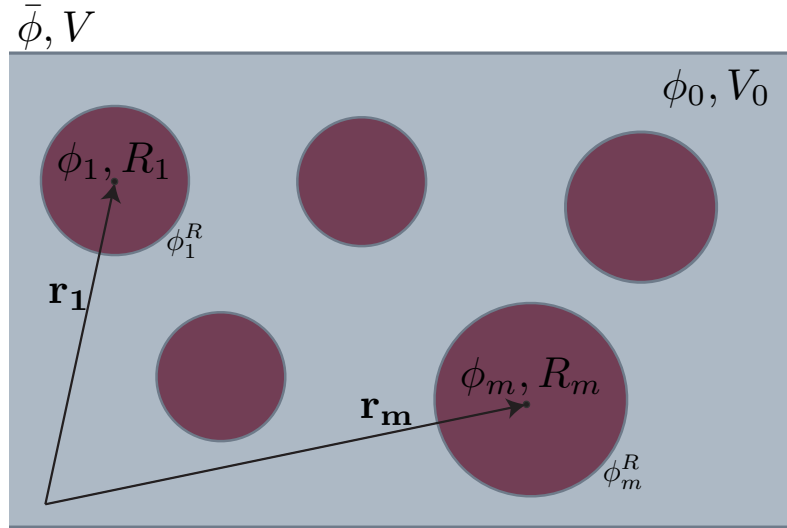


Figure 3.3.: Binary fluid model for m droplets. The droplet position, volume fraction, and size, are the model's independent variables, i.e. \mathbf{r}_i , ϕ_i , and R_i respectively. The global parameters are the system's average volume fraction, $\bar{\phi}$, and the system size, V . The background (cytosolic) volume fraction, ϕ_0 , and cytosolic volume, V_0 , are dependent variables, determined by conservation equations, 3.26 and 3.27.

The current model presented can be generalized for multiple droplets. For LS theory and nucleation we also require that the average the average distance between

each droplet is much larger than the average drop size and that nucleation events cannot occur within proximity of other droplets to prevent zones of depletion.

For a system with $m(t)$ droplets, the variables of the system are then,

$$\begin{aligned}\phi_1 &\rightarrow \phi_i \\ \phi^R &\rightarrow \phi_i^R \\ R_1 &\rightarrow R_i \\ \mathbf{r} &\rightarrow \mathbf{r}_i\end{aligned}$$

and the global constraints of the system become,

$$V_0 = V - \sum_{i=1}^{m(t)} 4/3\pi R_i^3 \quad (3.26)$$

$$\phi_0 = \frac{V\bar{\phi} - \sum_{i=1}^{m(t)} 4/3\pi R_i^3 \phi_i}{V - \sum_{i=1}^{m(t)} 4/3\pi R_i^3}. \quad (3.27)$$

An illustration of the model for multiple droplets is shown in figure 3.3. The total free energy is then a function of the volume fraction and size of all the droplets,

$$F_m(\{\phi_i\}_i^m, \{R_i\}_i^m) = V_0 f(\phi_0) + \sum_{i=1}^m (4/3\pi R_i^3 f(\phi_i) - 4\pi R_i^2 \gamma) \quad (3.28)$$

3.4. Droplet Dynamics in a Saturation Gradient

To implement spatially asymmetric growth, a gradient is induced into the saturation point of the system. This is done by explicitly introducing a spatial dependence into the free energy density. While having no “direct” effect on the background volume fraction, this allows for the supersaturation δ , to vary throughout the system,

$$\delta = \phi_0 - \phi^s(r). \quad (3.29)$$

In prior studies of droplet growth, the background monomeric field in the cytoplasm is assumed to relax to a steady state at a faster timescale than the growth of the droplet. This approximation has already been used in equation (3.13) to derive the equation for droplet growth (eqn.(3.17)). In a homogeneous growth field, or in the case of a single droplet, this is a fairly reasonable assumption which has been examined by others quite extensively, both theoretically and experimentally (e.g. See [46, 8, 57, 12, 51]). With asymmetric growth, the approximation of a homogeneous background field also comes under scrutiny. A more general approach which takes into account the monomeric background field, is utilized to make the quasi-static growth theory still valid, and to simultaneously allow us to test the validity of a homogeneous background field approximation in the case of inhomogeneous growth.

3.4.1. Spatially Dependent Free Energy Density

Since the molecular details of the P granule system are not known, a good deal of assumptions are made to determine the free energy density, $f(\phi)$. The only requirement, that has so far been stated, is that below the critical point, the free energy density must have two minima such that the system has two metastable states. In addition, we now require that $f(\phi)$ have a free parameter which can change the energy difference between these two minima, in a manner such that the saturation volume fraction, ϕ^s , changes monotonically with respect to this parameter. For simplicity, this free parameter is given an explicit linear spatial dependence along the x-axis of the system. For this work, two different free energies have been utilized. A generic double parabola, to simplify analytical calculations, and a Flory-Huggins free energy, that is grounded in a molecular derivation, which could in fact contain parameters that may be determined experimentally in the future. An example of each type is shown in figure 3.4.

Parabolic Free Energy Density

Two parabolas are utilized as Taylor approximations of the double well potential. The parabolic free energy density is defined as,

$$f(\phi) = \begin{cases} \frac{K_0}{2} (\phi - \psi_0)^2 & \phi \text{ cytoplasm} \\ \frac{K_1}{2} (\phi - \psi_1)^2 + B & \phi \text{ droplet} \end{cases} \quad (3.30)$$

where the cytoplasmic volume fraction and droplet volume fractions are respectively proximal to ψ_0 and ψ_1 , the base of the wells, where $0 \leq \psi_0 < \psi_1 \leq 1$. This energy corresponds to two Taylor expansions, where the derivative is not always continuous. Although figure 3.4 shows the parabolic free energy as a piecewise continuous function for $\phi \in [0, 1]$, it is only a reasonable approximation for ϕ close to the base of the wells, e.g. small levels of supersaturation. The region far from the base of the wells is not of interest, and so should not introduce any foreseeable problems in the lack of a clearer definition for equation 3.30. The droplet phase should have a more stable (constant) volume fraction as compared to the solution phase, thus the droplet curvatures should be greater than the cytoplasmic curvature, i.e. $0 < K_0 < K_1$. The parameter B , which sets the difference in height between the wells, is considered to be spatially dependent. As the phenomenological parameter to describe the gradient of the system, B is a monotonically increasing function of position, $B(x) \geq 0$; $dB(x)/dx \geq 0$.

Flory-Huggins Energy Density

For a better physical representation of the system, the Flory-Huggins free energy has been implemented for all simulations,

$$f(\phi) = \eta^a (1 - \phi)^2 + \eta^b \phi^2 + \chi (1 - \phi)\phi + (1 - \phi) \ln(1 - \phi) + \nu \phi \ln \phi. \quad (3.31)$$

This free energy density is derived, from an entropic and an enthalpic term, from molecular interactions (see appendix B for details). The molecular volume of the solution (water/cytoplasmic component) is typically smaller than molecular volume of the solute (P granule protein component) molecular volume, thus the ratio between molecular volumes of different species, ν , is constrained to, $0 < \nu \leq 1$. The bond energies between the monomers of the same type are, η^a and η^b . We hypothesize that what the Mex-5 protein gradient does to influence P granule formulation, is to stabilize the interaction between the two species, thus droplets dissolve in the region of high concentration, and condense in the region of low concentration. This is implemented in the interaction energy between the two species, χ , which is now the monotonically increasing, spatially dependent variable.

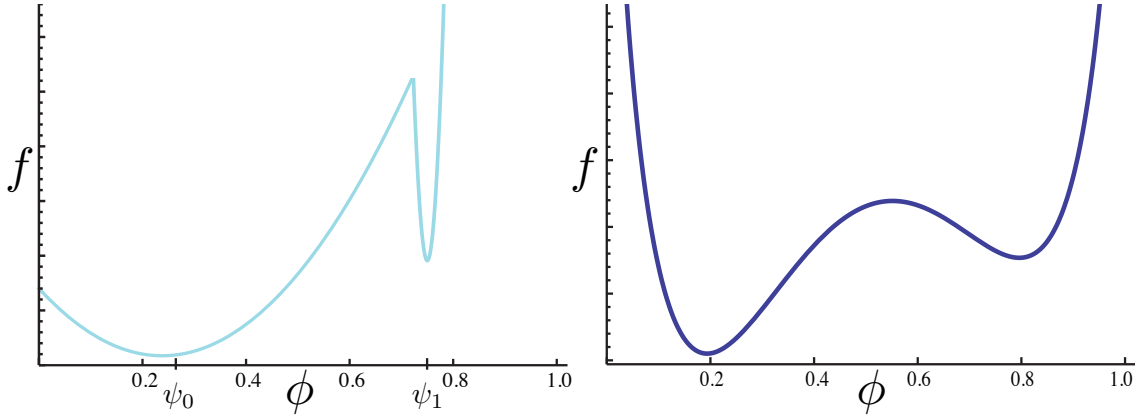


Figure 3.4.: Free energy density. In both plots the left well (ϕ poor) corresponds to the free energy of the cytoplasmic phase, and the right well (ϕ rich) corresponds to the droplet phase. (Left)Parabolic free energy density with parameters: $K_0 = 50, K_1 = 10000, \psi_0 = 0.25, \psi_1 = 0.75, B = 0.20$. (Right)Flory-Huggins free energy density with parameters: $\eta^a = 1.0, \eta^b = 1.1, \chi = 2.6, \nu = 0.75$.

3.4.2. Monomeric Background Field

In the case of multiple droplets undergoing asymmetric spatially mediated growth, the veracity of a homogeneous background field approximation is put into question. To test this, a more general assumption needs to be made: that the diffusion steady state (eqn. 3.13) is not necessarily valid globally, but is still valid within the neighborhood of each individual droplet. In other words, there is still a steady state ϕ^R about each droplet, but ϕ_0 is not necessarily isotropic throughout the system, and can be locally changed due to droplet growth, nucleation, and dissolution. These droplet dynamics are then treated, in an approximation, as point sources and sinks fixed in space at positions \mathbf{r}_i , for each droplet i . We first state the homogeneous case in this section, prior to developing the inhomogeneous case in the next section. In the case of infinite diffusion, and thus a homogeneous background field, ϕ_0 changes

only due to droplet growth. Treating the source/sink for each droplet as a point source, the equation for the background field with $m(t)$ droplets is,

$$\frac{\partial}{\partial t} \phi_0(\mathbf{r}, t) = - \sum_i^{m(t)} (\phi_i - \phi_0) Q_i \quad (3.32)$$

where Q_i is the strength of the source/sink term due to the growth of droplet i , with radius R_i .

$$\phi_0(\mathbf{R}_i) = \phi^R(\mathbf{R}_i) \quad (3.33)$$

The strength of the source/sink term is given then by the diffusive flux of droplet growth (see appendix D for derivation),

$$Q_i = \frac{4\pi R_i^2}{V - \frac{4}{3}\pi R_i^3} \frac{dR_i}{dt}. \quad (3.34)$$

3.5. The Droplet Growth Model Within a Gradient

In this section we develop the gradient droplet growth model. That is, we derive the dynamic equations for the background field and droplet growth in the spatially dependent free energy landscape described in the previous section. Due to this gradient, spatial dependence of all fluxes and volume fractions must be taken into account. We first create a continuous description of the gradient droplet growth model, and then develop a discrete model which is used in computer simulations presented in later chapters.

3.5.1. Continuum Description of Growth

Using mass balance, the total volume growth rate, V_i , of a droplet i is dependent on the volume fraction flux into the droplet (see appendix C for derivation),

$$\frac{dV_i}{dt} = \int_{\partial V_i} \frac{\mathbf{J}_i}{\phi_i - \phi_i^R} \cdot d\mathcal{A}, \quad (3.35)$$

Ignoring time scales where surface fluctuations occur, and assuming thus, that the droplet is at all times spherical with a fixed center of mass during growth, the droplet growth rate is,

$$\frac{dR_i}{dt} = \frac{1}{4\pi R_i^2} \int_{\partial V_i} \frac{\mathbf{J}_i}{\phi_i - \phi_i^R} \cdot d\mathcal{A}. \quad (3.36)$$

The flux on the boundary, \mathbf{J}_i , the background field, ϕ_0 , and the surface volume fraction, ϕ_i^R , are all now spatially dependent terms, due to the spatial gradient of the free energy.

The ϕ field on the interior and exterior surface of droplets, is set by a local equilibrium, the Gibbs-Thomson boundary condition, and the interior of the droplet

is assumed to be homogeneous (see section 3.2). Since the surface volume fraction ϕ_i^R , is set by a local equilibrium, it is not explicitly dependent on time, in contrast to the average background field, ϕ_0 (whose explicit time dependence we will derive shortly using mass conservation). The effect of time on ϕ_i^R is slightly more subtle. As a droplet increases in size, its curvature decreases. Since, $\lim_{R \rightarrow \infty} \phi_i^R(\mathbf{r}) = \phi^{(s)}(\mathbf{r})$, this ϕ^R also effectively decreases with droplet growth.

We now determine the background field starting from the local conservation equation,

$$\frac{\partial \phi_0}{\partial t} + \nabla \cdot \mathbf{J} = 0 \quad (3.37)$$

which can be written as an integral over some volume, \mathcal{V} as,

$$\int_{\mathcal{V}} d^3r \frac{\partial \phi_0}{\partial t} = - \int_{\partial \mathcal{V}} \mathbf{J} \cdot d\mathcal{A}, \quad (3.38)$$

where \mathbf{J} is the volume fraction flux through the surface of the volume. For an m droplet system, we distinguish between two types of fluxes: the droplet flux, which is the flux of material out of \mathcal{V} into droplets, and the bulk flux, which is the flux of material out of \mathcal{V} but still staying in the cytoplasm (or bulk),

$$\int_{\partial \mathcal{V}} \mathbf{J} \cdot d\mathcal{A} = \int_{\partial \mathcal{V}_0} \mathbf{J} \cdot d\mathcal{A} + \sum_{i=1}^m \int_{\partial V_i} \mathbf{J} \cdot d\mathcal{A}. \quad (3.39)$$

This equation points out the two types of fluxes that we are in fact interested in examining but at two different length scales. As we let the volume \mathcal{V} go to infinity, \mathcal{V}_0 scales proportionately, while each droplet volume, V_i , goes to 0. In this fashion we can study the bulk flux on longer length scales while neglecting the droplet surface.

We now consider the situation where droplet size is vanishingly small as compared to the system size. We thus define a new arbitrary volume element which is comparable to the system size, $\tilde{\mathcal{V}} \sim V$, and write down a new equation for the background,

$$\int_{\tilde{\mathcal{V}}} d^3r \frac{\partial \tilde{\phi}_0}{\partial t} = - \int_{\partial \tilde{\mathcal{V}}} \tilde{\mathbf{J}} \cdot d\mathcal{A} - \int_{\tilde{\mathcal{V}}} d^3r \sum_{i=1}^m \tilde{Q}_i \delta(\mathbf{r} - \mathbf{r}_i). \quad (3.40)$$

This equation is equivalent to equation (3.38) in the limit where the system size goes to infinity, while the droplet size is kept fixed. Each droplet is treated as a point source/sink term, where Q_i is the strength of the source/sink due to droplet growth. On this ‘‘long’’ length scale, we have only a bulk flux, where we impose no flux boundary conditions on the system boundary, V . As before, the bulk flux is written as a volume integral, and then converted it into a local equation. Using Fick’s law, $\tilde{\mathbf{J}} = -D\nabla \tilde{\phi}_0$, the differential equation equivalent to (3.40) is,

$$\frac{\partial \tilde{\phi}_0}{\partial t} = D\nabla^2 \tilde{\phi}_0 - \sum_{i=1}^m \tilde{Q}_i \delta(\mathbf{r} - \mathbf{r}_i). \quad (3.41)$$

Thus we have a diffusion equation with point source/sinks, to study the long range diffusive behavior of the system. Simultaneously, to maintain mass conservation, Q_i must still be determined from the short range droplet flux. Since we have collapsed the entire droplet into a single point, the rate of the source sink term becomes the total flux into the droplet,

$$\tilde{Q}_i = \int_{\partial V_i} \mathbf{J} \cdot d\mathcal{A}, \quad (3.42)$$

where \mathbf{J} is the droplet flux from equation (3.39), which is responsible for droplet growth, equation (3.36).

To arrive at the LS droplet growth flux,

$$J(\mathbf{r}_i) \approx \frac{D}{R} (\phi_0 - \phi_i^R), \quad (3.43)$$

for each droplet, we need to make several additional assumptions. As per LS theory, we assume that the average droplet size is much less than the average distance between droplets, and thus on average, droplet-droplet interactions are ignored. In line with our previous assumption, we make the additional assumption that the size of the droplet is sufficiently small such that the change in flux around the droplet does not change significantly from one point on the surface of the droplet, to another point on the same droplet. We have already implemented this with respect to system size, but this is now also important with respect to the implemented gradient, which effects the free energy landscape, and thus sets the volume fraction over each droplet surface. That is, we assume the effect of the free energy gradient is small enough such that the relation,

$$\nabla\phi(\mathbf{r}_i - R_i\hat{x}) - \nabla\phi(\mathbf{r}_i + R_i\hat{x}) \approx \mathbf{0}, \quad (3.44)$$

holds. This last condition would mean that we have a spherically symmetric flux into each droplet. The system is now simplified such that there is inhomogeneous growth across the entire system, but the flux into each droplet is isotropic, and so, the droplet growth is directly proportional to the flux.

Although the background field is clearly not at equilibrium, the spherically symmetric flux into each droplet suggests that at least within some neighborhood of each droplet, the field has relaxed to some local spherically symmetric steady state field, which has boundaries set by the quasi-static droplet growth on one side, and an average volume fraction background diffusion field on the other. We thus return to the growth flux of the homogeneous LS-theory, which now has spatial dependence, equation (3.44). That is, each droplet i , has a local steady state ϕ field which can be used to determine the flux into the droplet. This droplet flux still has spatial dependence, in that distinct drops have a distinct flux, but the flux into each droplet is isotropic. This flux used in the equation for droplet growth (3.36), gives now the previously discussed LS growth, equation (3.17), which is now spatially dependent.

We have so far discussed spatially dependent droplet growth and the background field of the m -droplet system with a gradient, our new contributions to the droplet

growth model. To study this system, we also require droplets to move throughout the system. We thus add noise to the system to allow for the diffusion of droplets. Overdamped Langevin dynamics (Brownian Motion) are used to describe the motion of each droplet,

$$\frac{d\mathbf{r}_i}{dt} = \sqrt{6D(R_i)}\boldsymbol{\xi}_i(t), \quad (3.45)$$

where ξ is Gaussian white noise with the properties,

$$\begin{aligned} \langle \boldsymbol{\xi}_i(t) \rangle &= 0 \\ \langle \boldsymbol{\xi}_i(t), \boldsymbol{\xi}_j(t') \rangle &= \delta(t-t')\delta_{i,j}. \end{aligned} \quad (3.46)$$

As stated before, equation 3.16, the droplet diffusion coefficient is determined with respect to the droplet component's monomeric diffusion coefficient, D , and molecular volume, v^b , using the Stokes-Einstein relation for a sphere,

$$D(R_i) = \left(\frac{3v^b}{4\pi}\right)^{1/3} \frac{D}{R_i}. \quad (3.47)$$

We now summarize the continuous gradient droplet growth model. For a system of m droplets, we have a set of $2(m+1)$ self consistent dynamic equations. The local diffusion of droplets occurs with a stochastic Langevin equation (3.45), where the diffusion coefficient of the droplet is set by Stokes-Einstein relation, as compared to its monomeric components. Spatially dependent droplet growth, equation (3.36), is determined by the short range volume fraction flux into the droplet, where the droplet boundary is set by a local equilibrium conditions of the Gibbs-Thomson relation, and thus dependent on the free energy landscape. The background field, equation (3.41), describes the long range diffusive behavior of the system, while treating droplets as point source/sinks. With this model we have a spatial growth gradient due to the imposed saturation gradient, but allow each droplet to grow isotropically and have negligible size. To derive these equations, we have made the assumption that there is a local equilibrium about each droplet as per LS theory, and that the size of each droplet negligible as compared to the system size, such that we can separate the system into two length scales, where we observe the long range bulk diffusion in the background, but describe the droplet growth with the short range diffusion through the droplet surface.

With an additional assumption, we can simplify the growth to the same (but spatially dependent) form as previously derived for homogeneous LS theory, equation (3.44). With the additional assumption that the droplet size is also negligible as compared to the effect of the newly induced gradient in the free energy. In practice, this final assumption will be unnecessary in this thesis, where in the discrete model presented in the next section, we allow for finite size droplets with anisotropic surface fluxes into each droplet.

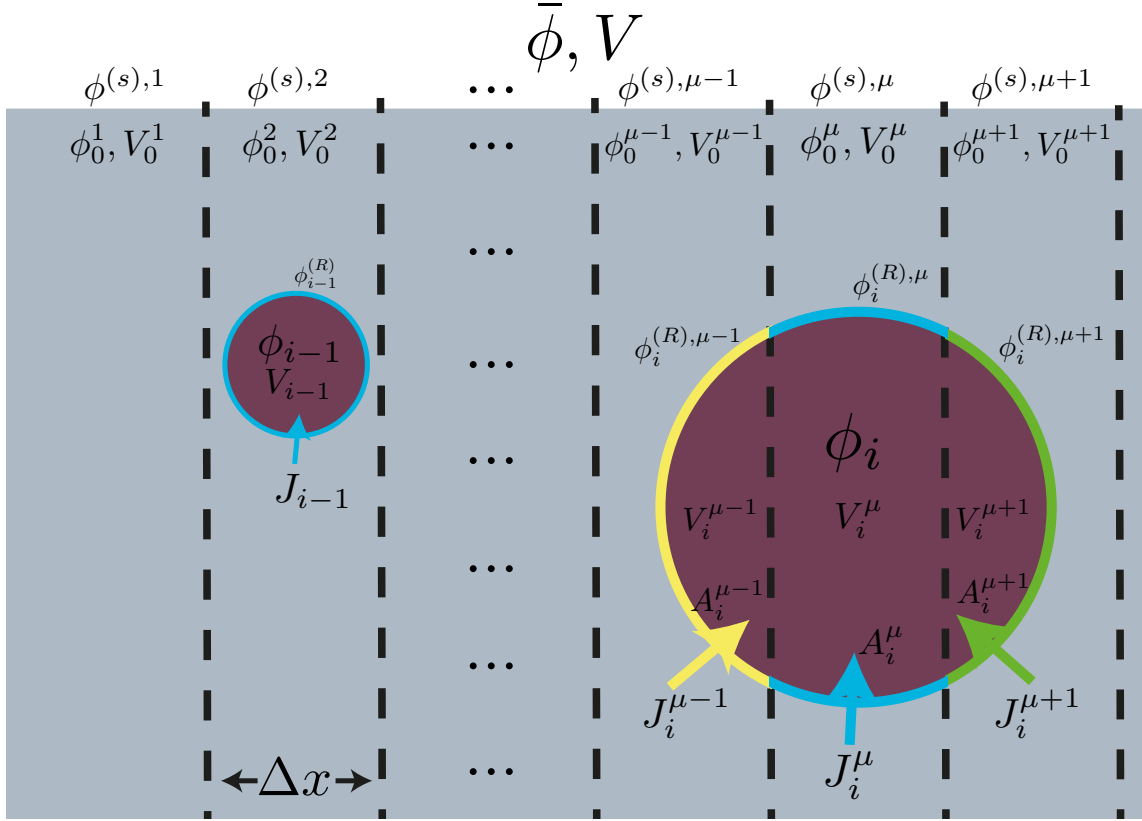


Figure 3.5.: Illustration of system discretization and the growth of droplets $i - 1$, and i . The system is discretized into grid volumes, where droplet growth occurs per grid. For small drops in only a single grid volume (drop $i - 1$), the droplet grows uniformly. For larger droplets (i), although the droplet still grows uniformly, the material flux into the droplet is not the same from each grid space, and is in fact proportional to droplet surface area A_i^μ within that grid space.

3.5.2. 1-D Discrete Model

We now describe the spatially discretized droplet growth model, where the background field is discretized. Since we implement a saturation gradient in only 1 direction, any new inhomogeneities should only appear in that direction. Thus, during droplet growth and nucleation within a gradient, as per LS growth, we continue to consider the inhomogeneities in the y and z direction as negligible, and only discretize the background in the x direction, as seen on figure 3.5. Each grid space μ , has two dynamic properties: a grid space volume V_0^μ , which corresponds to the total volume of the grid space not occupied by a droplet; and a grid space volume fraction ϕ_0^μ , the average volume fraction of volume V_0^μ (see figure 3.5). In addition to the system volume fraction $\bar{\phi}$ and system volume V , each grid space has an additional parameter, its saturation volume fraction $\phi^{(s),\mu}$, which is determined by the free energy as discussed before.

Droplets on the other hand, are considered continuous spherical objects, which

can be contained in a single grid space, or be partially in several grid spaces. Droplet growth is calculated per grid space for each droplet. As per LS growth, the ϕ flux into a droplet i , from a grid space μ is,

$$J_i^\mu = \frac{D}{R_i} (\phi_0^\mu - \phi^{R,\mu}). \quad (3.48)$$

This flux leads to an uneven volume growth rate G_i^μ , stemming from each grid space, where this rate is proportional to the surface area of the droplet within the space, A_i^μ ,

$$(\phi_i - \phi_i^{R,\mu}) G_i^\mu = J_i^\mu A_i^\mu, \quad (3.49)$$

where the total change in size of the droplet is the sum of this growth rate,

$$\frac{dV_i}{dt} = \sum_{\mu} G_i^\mu, \quad (3.50)$$

leading to the total change in volume for a droplet i ,

$$\frac{dV_i}{dt} = \sum_{\mu} \frac{J_i^\mu A_i^\mu}{\phi_i - \phi_i^{R,\mu}}. \quad (3.51)$$

Although a real droplet could grow anisotropically due to this spatially dependent flux (G_i^μ), we assume that the droplet relaxes to a spherical shape for the timescale of interest, and ignore all fluctuations of the droplet surface boundary. We thus take into account the volume change due to the uneven flux, but calculate a uniform growth rate for a spherical droplet,

$$\frac{dR_i}{dt} = \frac{1}{4\pi R_i^2} \sum_{\mu} \frac{J_i^\mu A_i^\mu}{\phi_i - \phi_i^{R,\mu}}, \quad (3.52)$$

To reiterate, although we take into account the anisotropic flux into the droplet from each grid space, the droplet is considered to grow uniformly outwards ($dR^\mu/dt = dR/dt$) from its center of mass. The actual change in volume of the droplet within each grid space, dV_i^μ/dt , is then proportional to the droplet surface area within that space,

$$\frac{dV_i^\mu}{dt} = A_i^\mu \frac{dR}{dt}, \quad (3.53)$$

where again we note, although

$$\frac{dV_i}{dt} = \sum_{\mu} \frac{dV_i^\mu}{dt}, \quad (3.54)$$

G_i^μ does not have to equal V_i^μ , where these two terms correspond to the anisotropic flux and symmetric growth discussed in the continuous case. As in the homogeneous

case in the previous section, we can write a source/sink term for the background field, due to the growth of a droplet i as (see appendix for derivation D),

$$\frac{\partial}{\partial t} \phi_{0(drop)}^\mu = \frac{\phi_i - \phi_0^\mu}{V_0^\mu} \frac{dV_i^\mu}{dt}. \quad (3.55)$$

In addition to a source/sink on the surface of each droplet, we allow diffusion to occur between neighboring grid spaces,

$$\frac{\partial}{\partial t} \phi_{0(diff)}^\mu = D \frac{\phi_0^{\mu+1} - 2\phi_0^\mu + \phi_0^{\mu-1}}{\Delta x^2}, \quad (3.56)$$

where a second order central difference scheme is used for the diffusion. Thus for an m droplet system, the corresponding monomer background field is,

$$\frac{\partial \phi_0^\mu}{\partial t} = D \frac{\phi_0^{\mu+1} - 2\phi_0^\mu + \phi_0^{\mu-1}}{\Delta x^2} - \sum_{i=1}^m (\phi_i - \phi_0^\mu) Q_i^\mu, \quad (3.57)$$

where Q_i^μ is,

$$Q_i^\mu = \frac{A_i^\mu}{V_0^\mu} \frac{dR}{dt}, \quad (3.58)$$

and $A_i^\mu = 0$ for bins that droplet i is not in. In contrast to the homogeneous background field, equation (3.32), diffusion in the x -direction has now been incorporated to deal with the inhomogeneities in ϕ , due to the saturation gradient. Equations (3.48) (3.52), (3.57), and (3.58), are now the equations to describe the $1 - D$ discrete droplet growth model. We will add nucleation and diffusion to the model in the next section.

3.5.3. Model Implementation

To analyze the discrete m -droplet problem with a gradient, we thus require a set of $(2m + 1)$ dynamic equations. In addition to the monomeric background field of the system, there is a stochastic equation of motion and a deterministic growth equation for each droplet.

These equations are now spatially dependent due to the imposed spatial dependence on the free energy density, $f = f(\phi, \mathbf{r})$; which effects volume fractions and the critical size, since $\phi_i(\mathbf{r})$ and $\phi_i^R(\mathbf{r})$ are determined by the local minimization of the free energy. That is, for a drop i of size R_i , the volume fractions are now determined from the two implicit equations with respect to the spatially dependent free energy density,

$$0 = f'(\phi_i, r_i) - f'(\phi_i^R, r_i) \quad (3.59a)$$

$$\frac{2\gamma}{R_i} = f(\phi_i, r_i) - f(\phi_i^R, r_i) - (\phi_i - \phi_i^R) f'(\phi_i, r_i), \quad (3.59b)$$

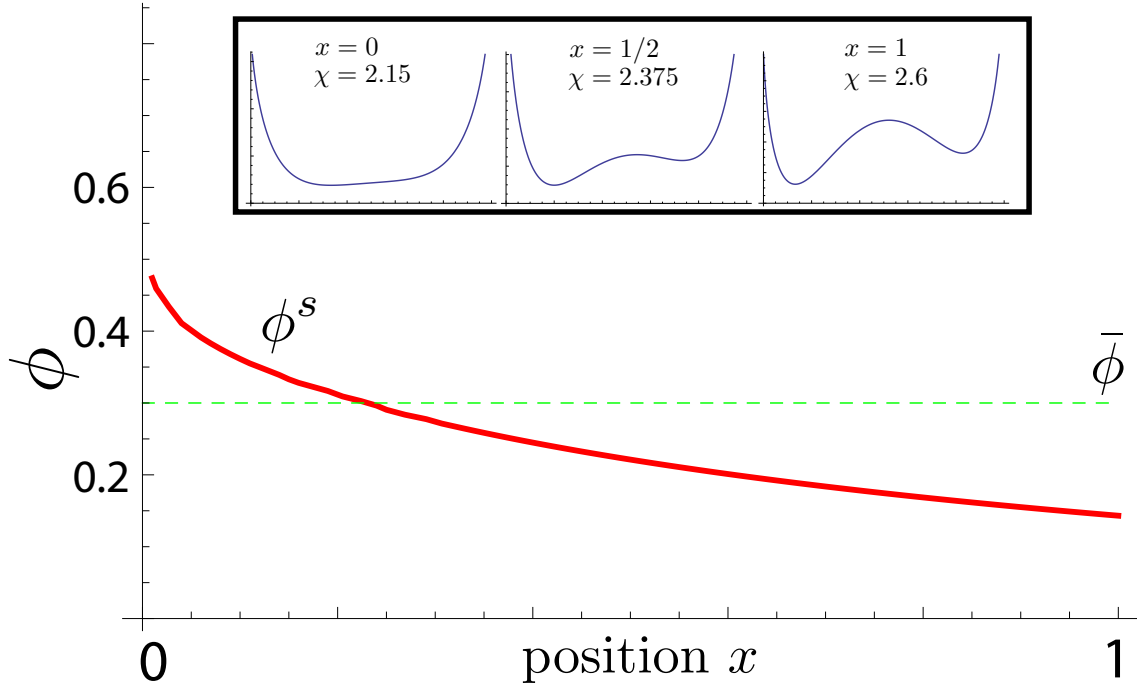


Figure 3.6.: Spatially dependent saturation point (ϕ^s). The interaction energy parameter, χ , of the free energy density is changed linearly along the long axis of the system. This effectively changes the ϕ^s , such that for a system with a uniform volume fraction $\bar{\phi}$ (green dashed line), only the part of the system where, $\bar{\phi} - \phi^s > 0$, is supersaturated. The plots on top show the free energy density $f(\phi)$ for the anterior, center, and posterior of the system respectively.

where $f'(\phi_i, r_i) \equiv \partial f / \partial \phi|_{(\phi=\phi_i, r=r_i)}$. The free energy is chosen to induce a growth preference along the long axis of the system, such that the droplets are most likely to nucleate and grow on one side (see figure 3.1), while in turn, the other side of the system is in a single phase state, and droplets, in or diffusing to this side, dissolve. As discussed previously, this growth preference is implemented into the free energy of the system through the spatially dependent component, as prescribed in section 3.4.1. By linearly changing this spatially dependent parameter along the long axis of the system, $\phi^s(x)$ decreases, which allows the system to be simultaneously oversaturated and undersaturated for the same background volume fraction, ϕ_0 (See figure 3.6). Using this continuous saturation point, each grid space is assigned the saturation point that corresponds to the midpoint of that grid space, i.e. grid space μ , which spans from $x_{\mu-1}$ to x_μ , has the saturation volume fraction of $\phi^{(s),\mu} \equiv \phi^s(\frac{x_\mu + x_{\mu-1}}{2})$. $\phi^{(s),\mu}$ is then a fixed parameter of grid space μ . Thus, a droplet that spans several grid spaces, has a different surface volume fraction per grid space, $\phi_i^R(\mathbf{r}) = \{\phi_i^R(x_\mu), \phi_i^R(x_{\mu+1}) \dots\}$, which is dependent on $\phi^{(s)}$ of the grid space, and the size of the droplet.

Although it has been implicitly stated, it should be noted that the number of droplets m is not fixed. If two drops touch, they are considered to instantly fuse

in a manner such that the total number of particles in each droplet and the total droplet volume is conserved. Surface fluctuations are completely neglected, and this new drop is assumed to be a sphere with center at the center of mass of the two original colliding droplets. The number of drops can thus decrease through fusion events, or if the droplet becomes unstable due to its size and/or position, such that it dissolves by droplet growth. The number of drops can also increase due to nucleation which will be implemented after time discretization.

For the discretization of time, we use an Euler discretization scheme, with varying time steps. That is, for some general time dependent function, $h(t)$, its time evolution over a single time step can be determined using,

$$h(t_n + \Delta t) = h(t_n) + \Delta t h'(t_n), \quad (3.60)$$

where time is discretized in the manner, $t_n = n\Delta t$. There are many, more sophisticated time schemes that one may choose. Due to the complex nature of this system, with the time evolution of several equations, both deterministic and stochastic; although not efficient, the Euler time scheme is a reasonable and reliable choice, which is quite stable for sufficiently small Δt . In this system, a constant Δt is also quite impractical. In time intervals with large supersaturation, where there are many droplets and nucleation occurs, fine time steps are required. In contrast, the interesting dynamics of coarsening regimes typically occur on time intervals which are several orders of magnitude larger. The time step, Δt , is chosen as the smaller of five time intervals. The minimum of: time required for a nucleation event, time required for the two closest drops to fuse, time required for a droplet to change size on the order of $R_c/10$, the time for a droplet to move into a new grid space, or a threshold minimum time interval.

The corresponding time evolution for the discretized droplet diffusion and droplet growth are,

$$\mathbf{r}_i(t_{n+1}) - \mathbf{r}_i(t_n) = \sqrt{6D(R_i)\Delta t} \boldsymbol{\xi}_i(t_n) \quad (3.61)$$

$$R_i(t_{n+1}) - R_i(t_n) = \frac{1}{4\pi R_i^2} \sum_{\mu} \frac{J_i^{\mu} A_i^{\mu}}{\phi_i - \phi_i^{R,\mu}} \Delta t, \quad (3.62)$$

where the right hand side of both equations are evaluated at $t = t_n$, and ξ is a normally distributed random number with the properties,

$$\langle \boldsymbol{\xi}_i(t_n) \rangle = 0 \quad (3.63)$$

$$\langle \boldsymbol{\xi}_i(t_n), \boldsymbol{\xi}_j(t_{n'}) \rangle = \delta_{t_n, t_{n'}} \delta_{i,j}. \quad (3.64)$$

As mentioned before, the number of drops increases due to successful nucleation events. With the addition of noise to allow for nucleation events, the time discretized

evolution for the background monomer field becomes,

$$\phi_0^\mu(t_{n+1}) - \phi_0^\mu(t_n) = \left(D \frac{\phi_0^{\mu+1} - 2\phi_0^\mu + \phi_0^{\mu-1}}{\Delta x^2} - \sum_{i=1}^m (\phi_i - \phi_0^\mu) Q_i^\mu \right) \Delta t - \frac{(V^*)^\mu}{V_0^\mu - (V^*)^\mu} (\phi^* - \phi_0^\mu) \Theta(\eta - P^\mu \Delta t) \quad (3.65)$$

where the right hand side is evaluated at $t = t_n$, Q_i^μ is the source/sink rate as per equation (3.58), and P^μ is the probability per unit time of a nucleation event to occur in a volume V_0^μ , to create a droplet of critical size, i.e. to create a droplet with volume V^* , and internal volume fraction ϕ^* . The random number η , is in the interval $[0, 1]$, with properties,

$$\langle \eta(t_n) \rangle = \frac{1}{2} \quad (3.66a)$$

$$\langle \eta(t_n), \eta(t_{n'}) \rangle = \sqrt{\frac{1}{12}} \delta_{n,n'}, \quad (3.66b)$$

and Θ is the Heaviside step function. The probability of nucleation has the same form as the nucleation flux (equation 3.25),

$$P^\mu = \alpha V_0^\mu \exp \left(- \Delta F [(R^*)^\mu] / k_B T \right), \quad (3.67)$$

where nucleation events are calculated per grid space as stochastic events. After a successful nucleation event, the center of the newly created droplet is placed randomly within the unoccupied volume of the grid space. Although this newly created droplet could potentially protrude over into several spaces, only the properties of the grid space where the successful nucleation event occurred are used, and only that grid space is depleted of material due to nucleation. After the successful creation of a new droplet, adjacent grid spaces that contain parts of the droplet are then subsequently adjusted.

Thus the set of $2(m + 1)$ equations, which describes the time evolution of the background field, equation (3.65), and the diffusion and growth of each droplet, equations (3.61) and (3.62) respectively, are the fully self consistent equations that describe our simulation model which will be studied in subsequent chapters. In this description, droplets are treated as continuous objects, which are only time discretized, where an equation of motion and a growth equation are used to simulate each droplet. Droplets diffuse continuously in a system with reflective boundary conditions, where their diffusion coefficient is updated after every time step (due to change in droplet size). When two droplets contact each other, they are considered to instantly fuse. This new droplet conserves the total volume of the original droplets, and is placed at the weighted (by mass) midpoint of the original droplets. As droplets diffuse, they move into and out of adjacent grid spaces. The volumes and volume fractions of grid spaces are adjusted accordingly. In our incompressible system, we

assume that the solute, a , moves freely between grid spaces, while b , the granule component, stays within the grid space during the droplet diffusion step. Thus, a droplet diffusing into a grid space μ , causes a decrease in V_0^μ , and an increase in ϕ_0^μ . Droplet growth is calculated per grid space for each droplet, where the fractional surface area of the droplet within each grid space is used to determine the proportionality of growth. As previously discussed, the background field is spatially discretized, see section 3.5. The volume and volume fraction of each grid space is simultaneously updated with the corresponding droplet which caused a change in the given grid space. The discrete diffusion equation is then solved using a finite difference Crank-Nicholson scheme with no flux boundary conditions [55].

4. Effects of a Spatial Gradient

Incorporation of spatially mediated growth within the droplet model allows for the observation of two interesting phenomena. Computer simulations will now be presented and discussed which demonstrate these two novel behaviors of the system: a long time non-equilibrium steady state behavior, and an early stage slow growth regime.

4.1. Long Times, Non-Equilibrium Steady State

In a finite system with uniform growth, it is well known that the system moves to a single droplet state where the final equilibrium size is set by the free energy and the global parameters of the system (see introduction, section 1.2.1). Due to the gradient across the system, this is not necessarily the case here. Over long times, drops can diffuse to the anterior, where they will dissolve. Thus the anterior functions as an absorbing boundary for droplets. This allows for nucleation of new drop(s) in the posterior. Although it is unlikely that germ granules exhibit this type of long time behavior, the physics is nonetheless quite interesting, and some insight into germ granule dynamics can still be shed. With an induced external gradient, the system can be potentially maintained at a non-equilibrium steady state. The goal of this section is to study this long term behavior and observe the properties of the steady state, if it in fact does exist.

Initial Conditions

Since the interest is in the long term behavior, the initial conditions should not play a significant role in these simulations. The two parameters of significance in this case would be for nucleation, to form new droplets, and the diffusion coefficient, since droplets only dissolve when they have diffused sufficiently towards to the anterior. Biologically unrealistic, but practical, parameters are thus chosen for the diffusion coefficient and for nucleation. Extreme values are also chosen for the free energy gradient, which effectively decreases the size of the system where stable droplets of a finite size can exist. This causes droplets to be quite large with respect to the “available” system size. Large droplets with respect to system size add two problems: Boundary effects become more significant, and the rate of droplet fusion increases dramatically. Boundary effects are not of interest in this study, so they are duly ignored. To avoid a droplet growth regime due to fusion, drops are only allowed to interact with each other through the background monomer field, i.e. drops can inhabit the same volume without fusing or repelling each other. Thus even though

Parameter		Description
Global		
ϕ	0.22	System volume fraction
V	31250 (50 × 25 × 25)	System volume [μm^3]
Molecular Properties		
D	20.0	Monomer diffusion coefficient [$\mu m^2/s$]
v^a, v^b	0.001, 0.0013	Monomer volumes [μm^3]
Free Energy		
$\bar{\gamma}$	0.01 (†)	Surface tension coefficient [μm]
η^a, η^b	0.1, 0.1	Bond energies, a-a and b-b
$\chi(0), \chi(1)$	2.0, 2.5	Interaction energy, a-b, at $x(0)$ and $x(1)$
Nucleation		
α	0.001 (†)	Nucleation prefactor [$s^{-1} \mu m^{-3}$]
$k_B T$	10^{-4} (†)	Nucleation Exponential Coefficient
Special:	No Droplet Fusion	
	†: This parameter will change later in this section	

Table 4.1.: Simulation parameters for non-equilibrium steady state simulation

multiple drops can and do inhabit the same volume, drops can be considered to move in their own separate system. Parameters for the simulation are listed in table 4.1.

Results

As hypothesized, the system goes initially to a single droplet state, where the droplet is approximately at its equilibrium size for whatever position it currently occupies. Over long times, this drop eventually diffuses to the anterior of the system, causing the drop to decrease in size as the equilibrium size also decreases. Once the drop moves far enough, such that it dissolves completely, or at least becomes small enough such that a sufficient amount of granule material is released back into the monomeric background field, nucleation events occur again in the posterior. This process repeats itself ad infinitum. Figure 4.1 shows a sample simulation of this process.

This long time behavior can be described as a single droplet state with an absorbing boundary in the anterior and a source in the posterior, figure 4.2 Without imposing any conditions for a single droplet system, one sees that the system naturally evolves to this state at long times. This can be attributed to the fact that the probability of nucleation decreases exponentially with droplet growth, in the same fashion as a system with no gradient, and surface tension still works to minimize the interface between the two phases.

As can be seen in figure 4.3, a clear distribution does emerge over long times.

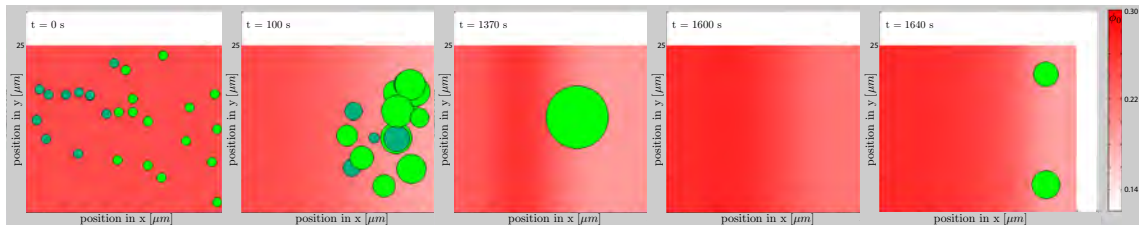


Figure 4.1.: Long time steady state simulation, sample movie. Regardless of the initial conditions, the simulation ends up spending most of its time in the single droplet state (3rd frame). Eventually over long periods, the droplet diffuses far enough to the left such that it shrinks and disappears (4th frame), but as the background is replenished with the dissolution of the droplet, new drops are nucleated (frame 5) and the droplet returns to the single droplet state. As seen in frame 5, multiple nucleation events can even occur. The probability of multiple nucleation events to occur are highly dependent on the nucleation parameters, but the probability of each successive event decreases exponentially.

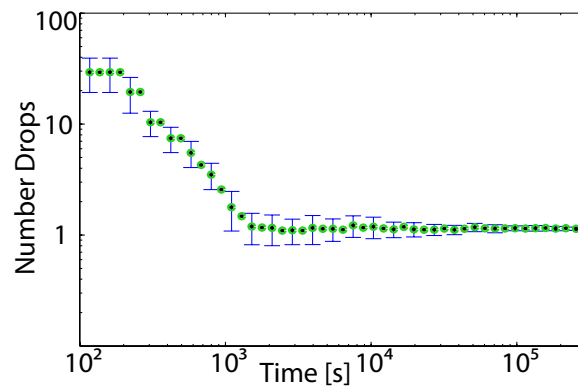


Figure 4.2.: Number of drops vs. time. Averaged over 100 simulations, error bars show the standard error.

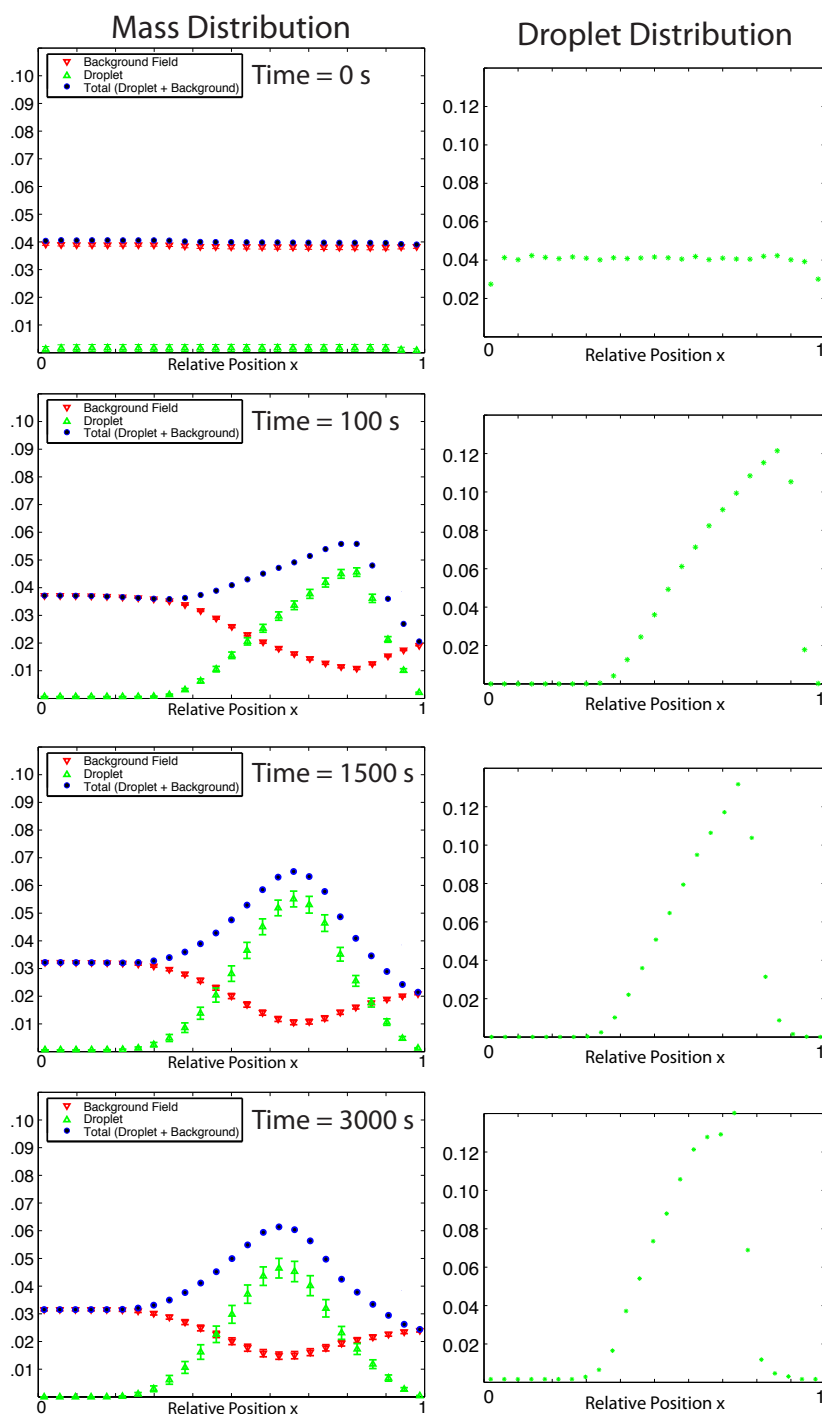


Figure 4.3.: The time evolution of the spatial distribution of granule component and the granule dense droplet phase, for long time the steady state simulations. (left) Mass distribution of granule component: in the monomeric background field (red), within droplets (green), and the sum of both (blue). (right) Droplet distribution. Averaged over 5197 simulations, error bars show the standard error.

Ignoring boundary effects, the distribution of granule material in the posterior is higher than the anterior. The background field shows a complementary distribution, where there is a greater depletion in the posterior. The localization of granule material to the posterior corresponds with the depletion of material from the background, which is compartmentalized into droplets. This localization is affected by the changing diffusion coefficient of the droplet. Since larger drops diffuse slower, using the Stokes-Einstein relation, and have a larger equilibrium size in the posterior, they are “held” within the posterior of the system. As they diffuse more and more into the anterior, they move more rapidly due to their decrease in size.

The droplet spatial distribution at steady state (figure 4.4) shows corroborating information. Droplets are localized to the same x -position as granule material while the background is depleted. In addition, the size distribution of droplets at a given position, figure 4.4 (bottom) is sharp in the posterior, and broadens moving into the anterior. For the slow moving droplets in the posterior, the smaller spatial fluctuations due to diffusion allows the size of the droplet to relax to its steady state size for its current spatial position, while the larger fluctuations in the anterior increase the likelihood that the size of the droplet is further from steady state for that given position. As seen in figure 4.5, the mean size of the droplet is larger in the posterior, and decreases going into the anterior. Conversely, due to the greater diffusion rate of smaller droplets, the standard deviation about the mean increases as the droplet gets smaller. From a physical standpoint, one would expect that the Brownian motion of each droplet would lead to a normal distribution in its size. Due to finite size Euler time steps in the computer simulations, and a larger diffusion coefficient approaching some position x from the anterior side, as compared to the posterior side, the distribution is biased to the anterior.

4.1.1. Multi-Droplet Steady State

As previously mentioned, the single droplet state is due to an exponentially decreasing nucleation rate with respect to the background monomeric concentrations of the granule component, and surface tension. By decreasing the surface tension (10^{-4}), and changing the nucleation such that the prefactor dominates over the exponential term (here we set $k_B T = 1$), it is possible to create a steady state with multiple droplets. Figure 4.6 is a sample configuration of this steady state. With the prefactor of the nucleation dominating in this regime, the nucleation rate does not decrease significantly with each nucleation event, such that multiple nucleation events can occur. It is also necessary that that droplet growth is slow as compared to the diffusion of the droplet, such that the size of each droplet is set by position and the free energy landscape. This means that Ostwald ripening, due to larger droplets, is a negligible effect, since these larger droplets diffuse sufficiently quickly (as compared to their growth) to a region of the system where they themselves also become unstable. From this description and figure 4.6, one can see that this so called “steady state” is highly dynamic. This steady state is an ensemble average where

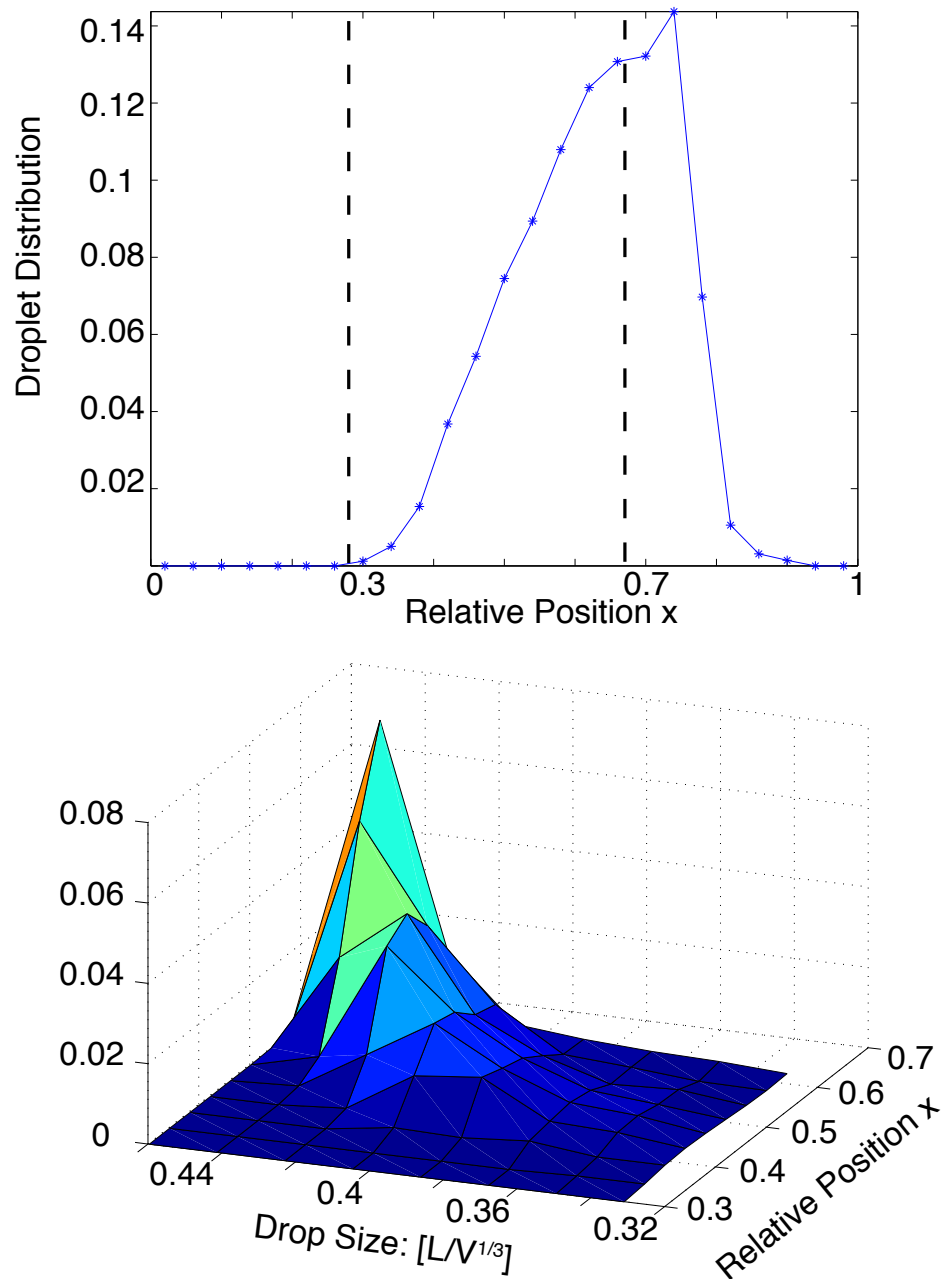


Figure 4.4.: Droplet Distributions. (Top) Spatial drop distribution. The region of interest lies between the two black dashed lines, as outside of this area is affected by system boundaries. (Bottom) Spatial and size distribution. Only the region between the two black dashed lines is displayed

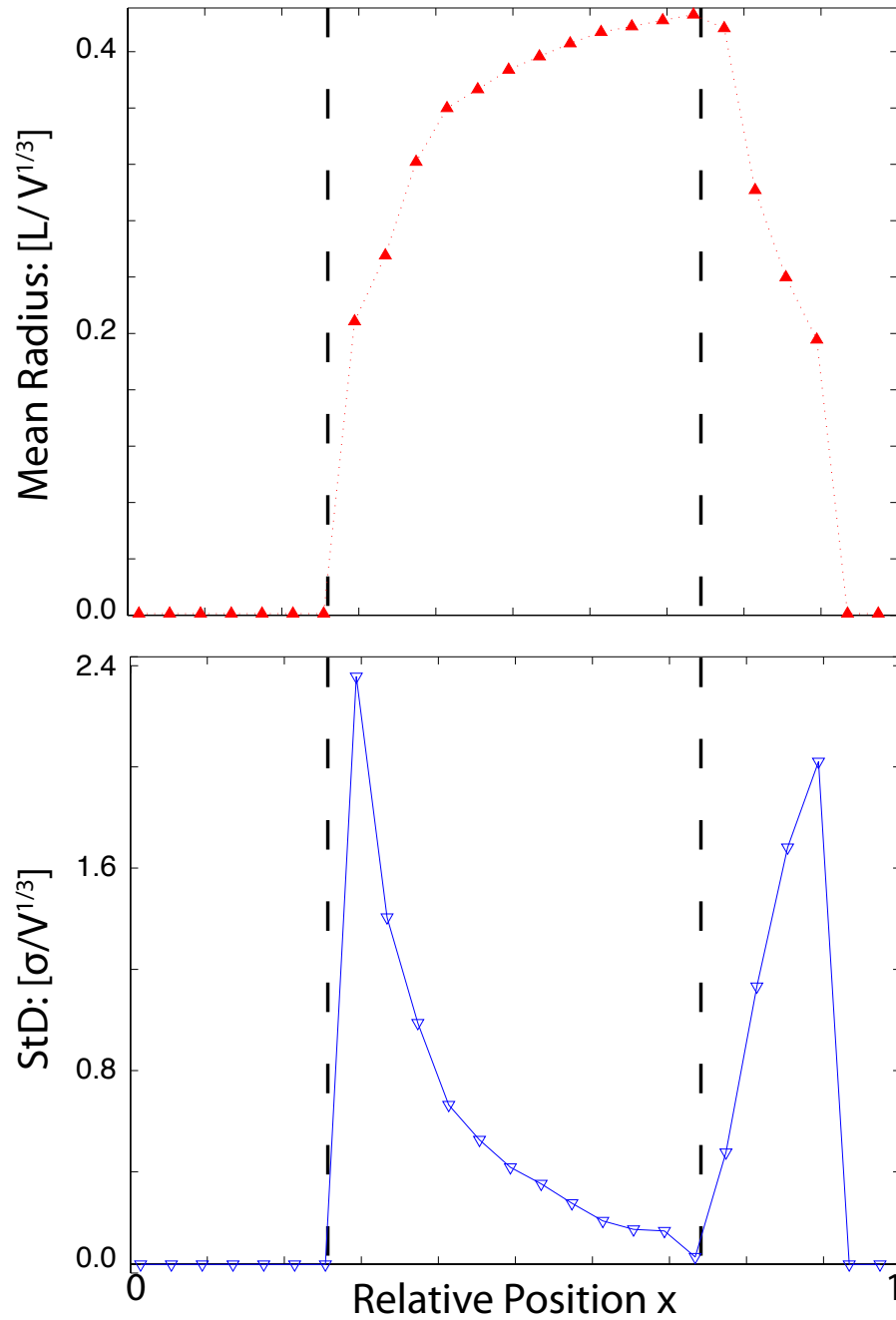


Figure 4.5.: Drop mean radius $\langle R \rangle$ (top) and standard deviation (bottom) of the mean with respect to position within the system, averaged over 15366 simulations. System parameters are shown in table 4.1. Quantities are normalized by the system size. The regions of interest lies between the two black dashed lines as outside of this area is affected by the system boundaries.

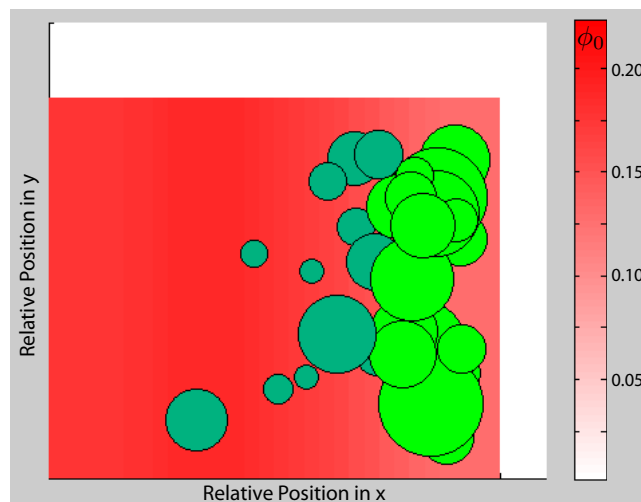


Figure 4.6.: Sample image of a multi-droplet steady state. As droplets diffuse to the anterior and dissolve, new droplets nucleate in the posterior.

the number of droplets and the total droplet volume converges (figure 4.7). Looking at the size distributions, figure 4.8, we observe again that the size distributions at a single point, and across the system appear to be normally distributed about a mean size for that point. Again the distributions appear slightly skewed, which would be due to boundary effects.

Although this multiple droplet steady state appears significantly different as compared to the single droplet steady state, it is in fact quite similar. The mass distributions are indistinguishable, and in fact, the cyclical nature of the system is better elucidated in the multi-droplet case, by looking at the average droplet growth rate, figure 4.9. Due to the strong gradient across the system, droplet nucleation (not shown) and growth is heavily preferred in the posterior. A net growth is thus observed in this region, which depletes the background monomer concentration, as noted in the single droplet case. As the droplets diffuse towards the anterior, this preferential growth decreases, until eventually the droplets completely dissolve and replenish the background. With this gradient in the background concentration, granule components diffuse back to the posterior allowing for growth to continue. It is also interesting to note, with respect to this average growth rate, that although this is a steady state distribution, it looks remarkably similar to the average growth in P granules, figure 2.6.

As this multi-droplet steady state appears to be effectively the same as the single droplet case, it is important to examine the effect of the nucleation prefactor. Particularly, how does the nucleation prefactor α affect the number of droplets at steady state, and how does it affect the time required to reach steady state. Keeping all other parameters fixed, we see that by increasing the nucleation prefactor, the average number of droplets at steady state increases, and the system approaches

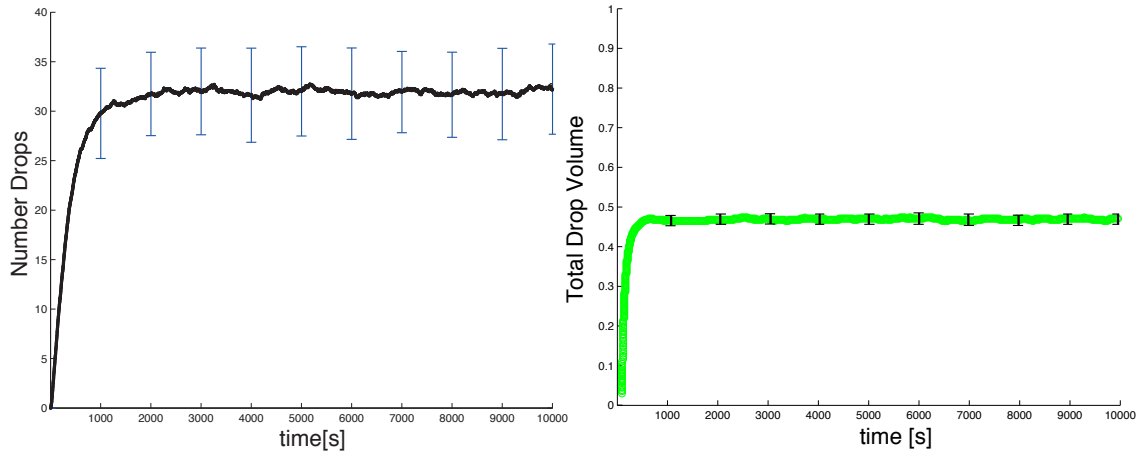


Figure 4.7.: Time evolution of the number of drops (left) and total droplet volume (right) for the multiple droplet steady state. Simulations began with 0 droplets, with the nucleation prefactor, $\alpha = 1$. Data was averaged over 5000 simulations. Error bars show the standard error, and the total droplet volume is normalized using the system volume.

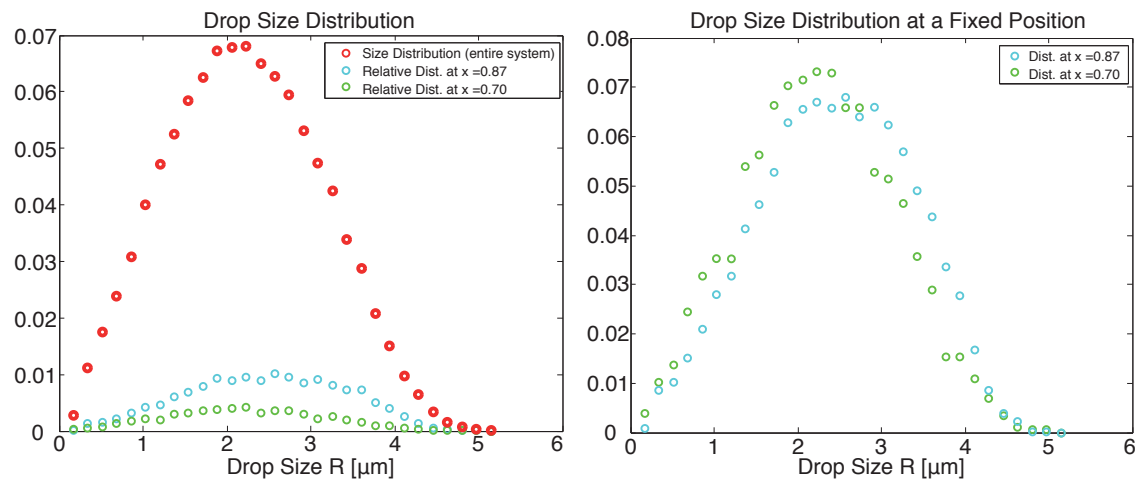


Figure 4.8.: Droplet size distribution. (Left) Droplet size distribution across entire system, and the relative size distributions of two points in the posterior. (Right) Size distribution of droplets at the point in the system with the most droplets ($x = 0.87$), and a point with approximately half the number of droplets.

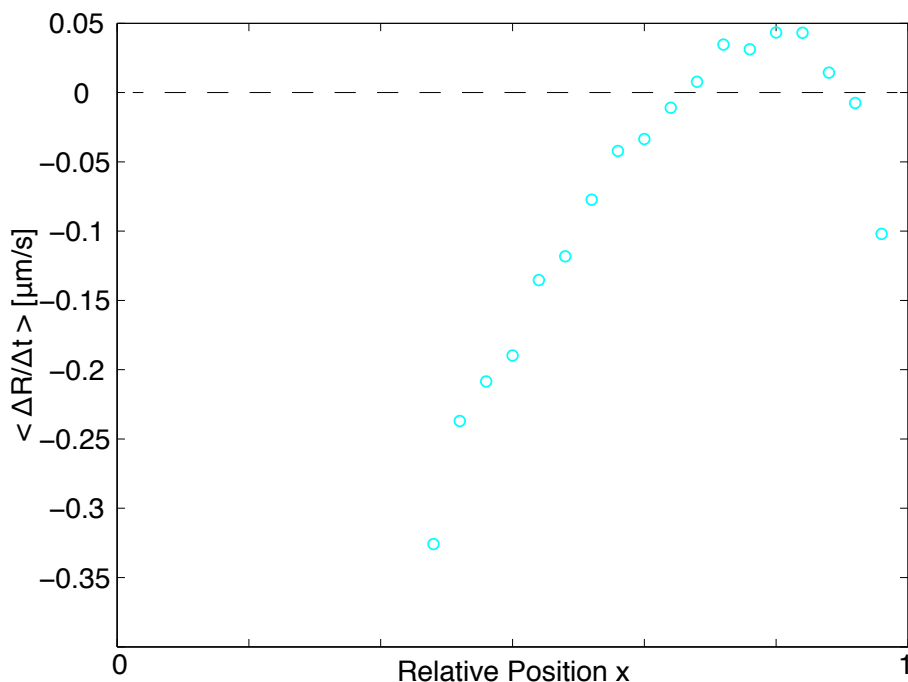


Figure 4.9.: Average growth rate across system at steady state. The growth rate of all drops within a given spatial bin are averaged, where the position of each drop is defined by position of the center of the drop.

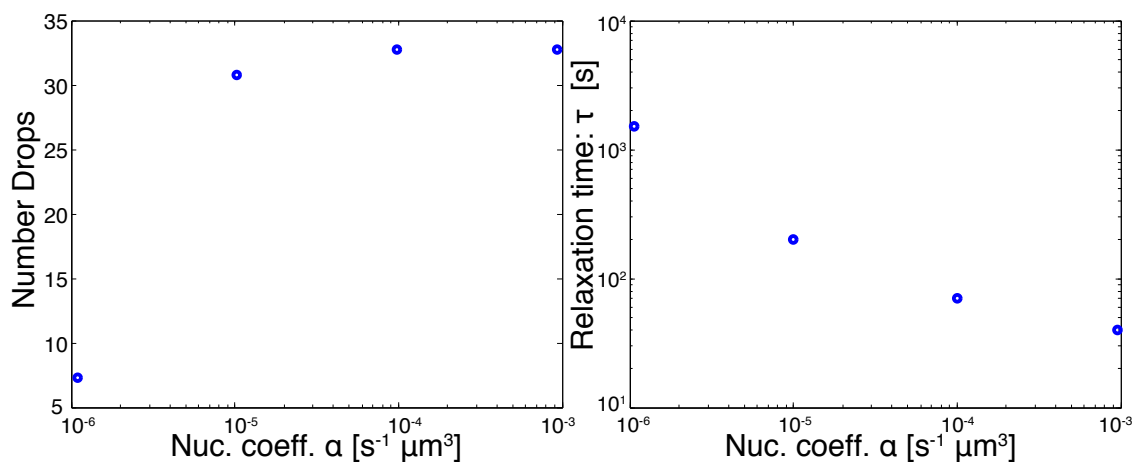


Figure 4.10.: System dependence on nucleation coefficient, α . (left) Average number of droplets at steady state with respect to α . (right) System relaxation time, τ , with respect to α , where the relaxation time is defined with respect to the droplet steady state volume. All system parameters, other than α are taken from table 4.1

steady state at a quicker rate. Both these values plateau for large α . This is in fact due to the local super saturation, and droplet diffusion. For large α , the system is locally depleted such that the local supersaturation goes to 0.

For new droplets to form, the ones that have been created must diffuse to the unstable region of the system, dissolve, and have the background components return. Thus the creation of new droplets can only occur by the destruction of existing droplets. This demonstrates that the number of droplets increases with α , but the free energy sets an absolute maximum number of droplets with the critical size, which diverges with the supersaturation going to 0, equation (3.19). This absolute maximum describes the maximum number of droplets that can be created, and exist at one time. If droplet diffuse sufficiently fast, they will move to an unfavorable region and dissolve, allowing for a new nucleation event; which gives the cyclical nature that is the focus of this section. For low diffusion, droplets will deplete each other through Ostwald Ripening, which would return the system back to the single droplet limit.

Typically nucleation has little to do with a system's relaxation time. Nucleation is a process one observes at very early times, where the majority of the system lifetime is spent with the growth of already nucleated droplets. In this spatially dependent system, this is not necessarily the case. First, the number of droplets at steady state affects the steady state volume. As the average number droplets increase, due to surface effects, the total droplet volume at steady state decreases. In fact, for an ideal choice of free energy parameters, and a large enough droplet diffusion coefficient, it is possible to create a system which arrives at steady state almost entirely through nucleation. New droplets would form and quickly diffuse to an unstable region and dissolve, allowing little time for droplet growth. By again, as decreasing the droplet diffusion, a greater proportion of the system lifetime is spent in a droplet growth regime, which also consequently causes the total droplet steady-state volume to increase.

4.2. Slow, Droplet Growth Regime

The goal of this section is to describe an early growth regime that exists due to the spatial gradient. Most simulation parameters are chosen to emulate the *C. elegans* embryo, but have not as of this section, been seriously compared to experiment to optimize these parameters. The parameter choices here are in fact the starting point for the optimization and comparison to the experiment which will be presented in the next chapter.

Initial Conditions

Initial conditions are chosen such that the growth dominates over nucleation and fusion of droplets. The total number of particles and total volume are set by the parameters, $\bar{\phi} = 0.3$, and $V = 31250\mu m^3$. It should be noted that the chosen

Parameter		Description
Global		
ϕ	0.3	System volume fraction
V	31250 ($50 \times 25 \times 25$)	System volume [μm^3]
Molecular Properties		
D	2.0	Monomer diffusion coefficient [$\mu m^2/s$]
v^a, v^b	0.001, 0.0013	Monomer volumes [μm^3]
Free Energy		
$\bar{\gamma}$	0.01	Surface tension coefficient [μm]
η^a, η^b	0.1, 0.15	Bond energies, a-a and b-b
$\chi(0), \chi(1)$	2.15, 2.6	Interaction energy, a-b, at $x(0)$ and $x(1)$
Nucleation		
α	0.01	Nucleation Prefactor [$s^{-1} \mu m^{-3}$]
$k_B T$	10^{-5}	Nucleation Exponential Coefficient

Table 4.2.: Simulation parameters for slow growth simulation.

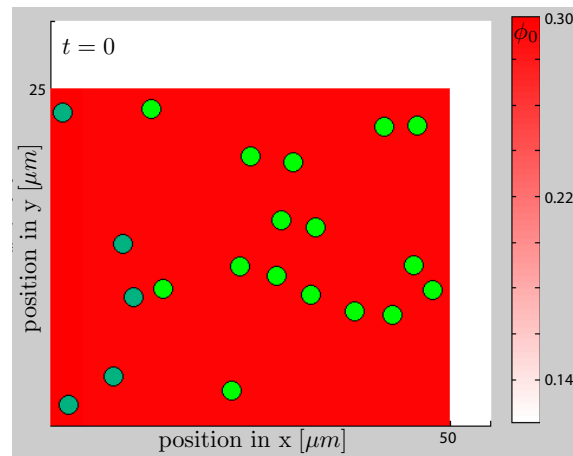


Figure 4.11.: Starting frame of Simulation. Two dimensional projection of a 3-D simulation. Droplets are randomly distributed throughout the system, with a Gaussian distribution about $R_c(\phi, L/2)$ for the size of the droplet. Bright green droplets are growing while aqua droplets are dissolving.

volume is a reasonable estimate of the cell volume, but $\bar{\phi}$ is large, considering that the cell cytoplasm is $\approx 70\%$ water. This extreme value was chosen for two purposes. First, without having any knowledge of the molecular properties of P granules, this value allows for simple choices for the free energy parameters to allow for a phase transition. Second, since all P granule material is simplified into component b , it is not altogether clear how to define the volume fraction, as each individual component does not necessarily appear in the cytoplasm and the droplet in the same ratio. Although the concentration is most likely at least an orders of magnitude smaller, the value 0.3 serves as a clear absolute maximum which can be later reduced with more information pertaining to the system.

Droplets are randomly distributed throughout the entire system, where the droplet radius is a normal distribution ($\sigma = 5\%R_c$) centered around the critical radius at the midpoint of the system, $R_c(\bar{\phi}, 1/2)$. The background is subsequently depleted from the value $\bar{\phi}$, to take into account all the formed droplets, such that there is initially a uniform monomeric field. Figure 4.11 shows a sample 2D graphic representation of the system with the prescribed initial conditions. With an initial homogeneous background monomeric field, $\phi_0(t = 0)$, approximately 2/3 of the system is still supersaturated such that droplets grow (bright green droplets), which is consistent with how the interaction parameter for the free energy was chosen (fig.3.6). The main goal of this work is to use this model to analyze germ granule compartmentalization in the posterior, thus with the chosen initial conditions, nucleation has a negligible effect and observed only for very early times ($t \sim 10s$); the system is in the regime dominated by growth. Even though choice of the spatially dependent interaction parameter for the free energy is somewhat arbitrary, it is chosen in a manner such that the left side of the system, $x = 0$, is always undersaturated for the starting volume fraction $\bar{\phi}$, and that by the middle of the system, $x = 1/2$, the system is supersaturated for the same volume fraction (figure 3.6).

Results

Figure 4.12(left frame) shows a typical sample simulation from the prescribed initial conditions. One can see that implementing a gradient in the free energy along the long axis of the system can be a successful method of organizing the system, localizing droplets to one side. Starting from a state with both a uniform background distribution and a uniform droplet distribution, the system evolves to a state where drops exist and grow only in posterior, with an uneven depletion of the background field. This localization, which occurs through the preferred asymmetric growth of posterior droplets, not only depletes the background field, but also creates a ϕ gradient in the background (fig. 4.12 middle frame); which is opposite to the induced ϕ^s gradient. As the droplets do become localized to the posterior ($t > 1000s$), the background gradient is still existent, but has decreased substantially in magnitude. Concurrent with the depletion of the background and formation of a background gradient, the data shows that not only do the droplets localize to the posterior,

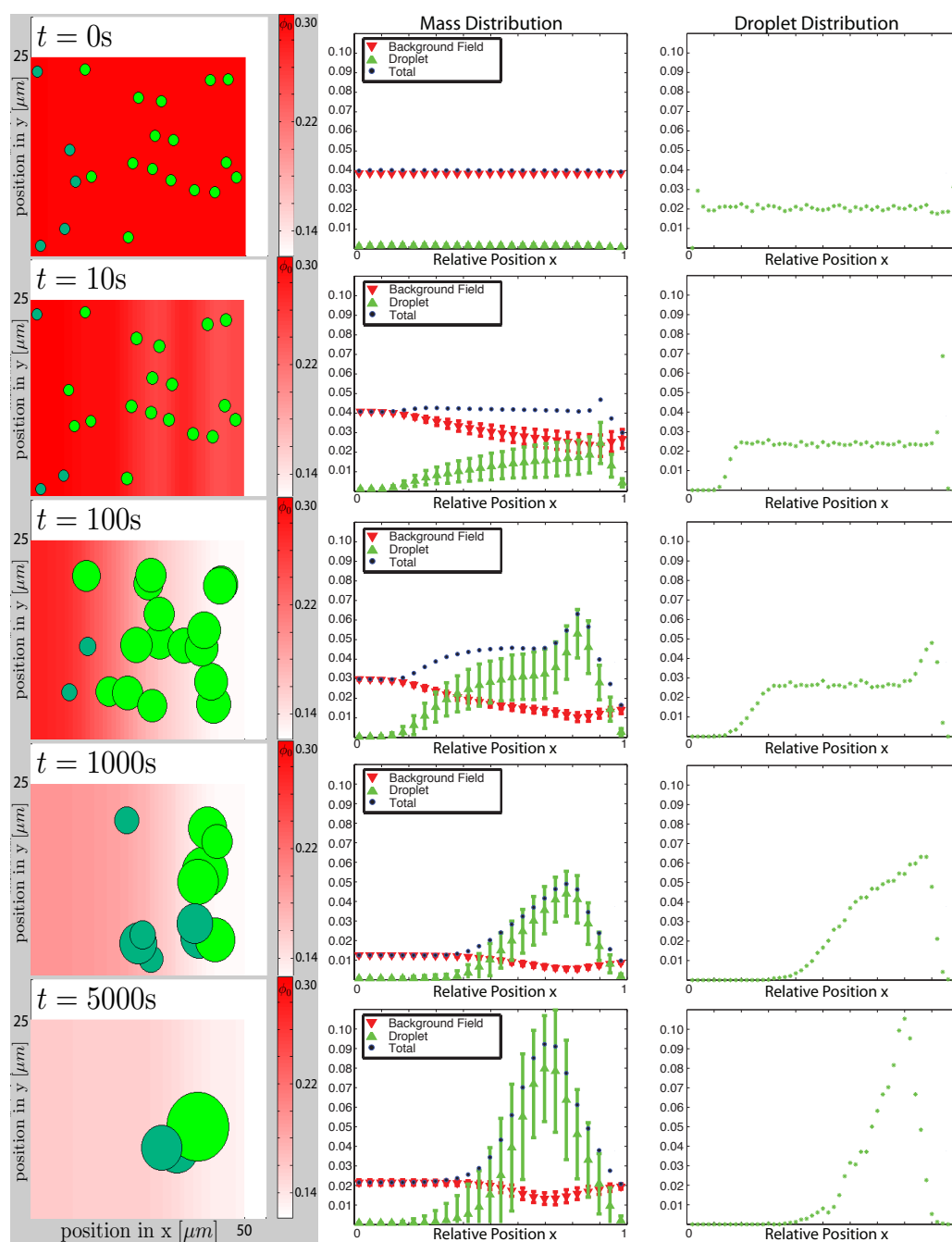


Figure 4.12.: Left: Sample 2-D graphic projection of 3-D simulation. As drops grow (green droplets) and shrink (light blue droplets), they unevenly deplete the monomeric background (red). Middle: The distribution of granule the component, $P(N^b)$, in the background (red), droplet (green), and the sum of both (blue). There is a clear gradient of the background field, which starts to disappear as the system approaches a single droplet. Right: Droplet distribution. As droplets get larger and localized, a few drops take in most of the granule components. Model parameters given in table 4.2. Averaged over 1018 simulations, error bars show the standard deviation.

but via the droplets, the granule components also localize to the posterior. With the chosen parameters, this localization results in $\approx 25\%$ of the granule material remaining in the anterior, while the rest of the material is localized in the posterior, in droplet form. Similar experimental results have been recently presented by Griffin et al.[28].

Although the system is initially in a droplet growth regime, it can be noted that this is not LS growth per se, as the system does not follow LS scaling. Observing the average number of drops over time, only for late times, $t > 1000\text{s}$, does one see the expected scaling for the average number of droplets, $N \propto t^{-1}$, that is known for the case of isotropic LS growth (figure 4.13). From LS theory, this power law is the

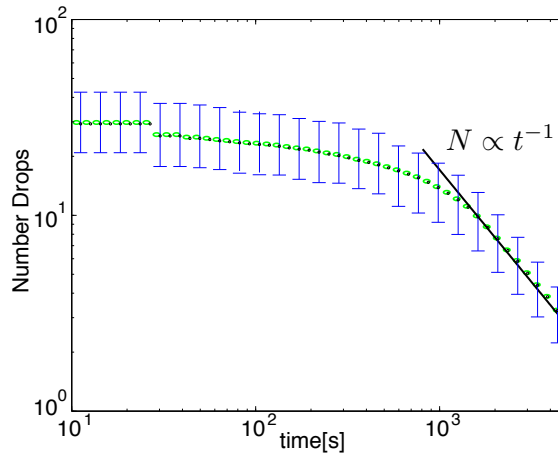


Figure 4.13.: Number drops as a function of time, averaged over 1018 simulations. The error bars show the standard error. The black line is a 2 parameter fit, which shows the power law dependence for the average number of drops at late times.

direct consequence of the average droplet size scaling with time. Examining droplet volumes (figure 4.14), one sees that the total droplet volume plateaus relatively quickly, which indicates that the droplet mean size, $\langle R \rangle$ grows with larger droplets growing through the depletion of smaller droplets. The scaling for the size, $\langle R \rangle t^{1/3}$, is observed again only at later times. Thus, there is a “slow growth” regime, prior to LS growth.

This slow growth regime does in fact make intuitive sense. With asymmetric growth, the background monomeric field is consequently asymmetrically depleted. Although the saturation point, ϕ^s , is lower in the posterior, the supersaturation, $\phi_0 - \phi^s$, is also less as compared to the isotropic case. This observation can be seen in the sample simulation, figure 4.12(left frame). The local depletion of ϕ_0 (background red field) in the posterior is greater in the posterior, which is due to the preferred growth in the same region. Only when the system approaches homogeneous growth, i.e. where the droplets are growing/dissolving at the same supersaturation, at $t \sim 1000\text{s}$, does the system show LS growth behavior. This point is reinforced by comparing this growth with similar simulation with no inhomogeneous background

field. In the case where there is no gradient whatsoever (figure 4.14b), one sees the expected growth behavior. Interestingly though, with a gradient, but where the background field is homogeneously depleted, i.e. monomers are assumed to diffuse infinitely fast (figure 4.14c), there is also no slow growth phase. Similar to the case with no gradient, the system shows LS growth behavior approximately 2 orders of magnitude in time prior than the inhomogeneous case. The slower growth behavior can be observed even within the average drop size for each half of the system. In the case of infinite diffusion, the posterior side shows the same scaling behavior as the system average, while with finite monomer diffusion, the growth of the posterior is slowed.

Looking finally at the size distribution of the droplets, figure 4.15. The theoretical scaling from LS theory [46] (see also introduction 1.2.1), for the distribution function, $g(z)$, where $z \equiv R/\langle R \rangle$, and the mean radius, $\langle R \rangle = (4/9t)^{1/3}$, is compared to the normalized size distribution from simulations. As an initial condition imposed on the system, the simulations were started with droplets' sizes close to the critical size. This means that the system starts as a narrow distribution about $R/\langle R \rangle$. During slow growth, the distribution is below the theoretical distribution and eventually converges to it. Due to finite size effects of the system, a perfect fit is not expected.

4.3. Chapter Summary

In conclusion, a gradient in the saturation point of a binary phase transition is sufficient to induce spatial organization. It has already been well established that a phase transition can compartmentalize a single component to one phase [53]. With spatially asymmetric growth, the preferential growth of some droplets induces the dissolution of droplets in the non-preferred region, and thus spatially localize both droplets, and their granule components. Although this is not altogether surprising per se, there are several interesting properties and effects that are a matter of note: Due to the gradient, the system does not go to a single droplet equilibrium state, but instead to a non-equilibrium steady state. The gradient can thus be thought of as external field which does not allow the system to relax to equilibrium. Spatially induced phase transition is an effective method of organization. Without the need for motors or convection, one side of the system can be nearly completely depleted of a single component, which is thereby concentrated in a different state on the opposing side. The asymmetric growth of droplets occurs at a slower rate than normal LS growth. Due to local background depletion, asymmetric growth demonstrates a slower growth behavior, i.e. slower than expected $\langle R \rangle \propto t^{1/3}$ for LS growth. The final state of the system is a single droplet, but due to slower growth/competition of droplets in the posterior, there are more droplets in the posterior for an equal level of background depletion in the anterior. The dissolution/growth of droplets creates a gradient in the background field. Although this gradient decreases in magnitude

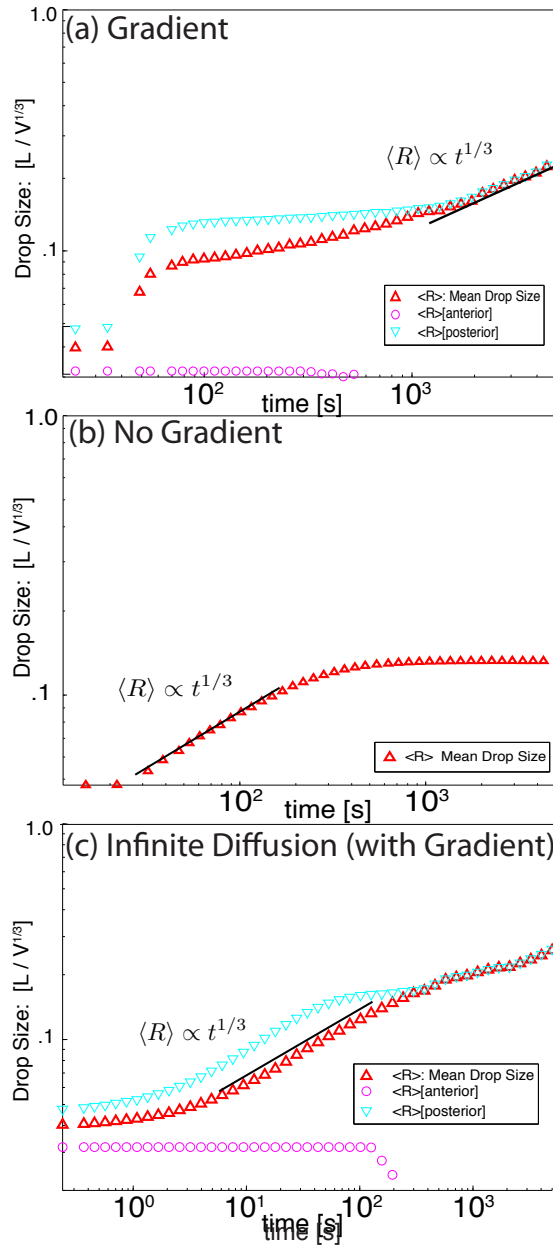


Figure 4.14.: Average droplet size as a function of time. The red triangles show the mean droplet size (radius), $\langle R \rangle$, where all values are normalized by the system size, $V^{1/3}$. The mean drop size in the posterior half (light blue), and in the anterior half (purple) are also displayed in the situations with a gradient. Time scales are different for each plot. (a) In the case of a monomeric diffusion field with a gradient, there is a period of slow growth, and only at late times does $\langle R \rangle$ scale with $t^{1/3}$. This is indeed the slow growth of the posterior, while the average size in the anterior half stays fairly constant. (b) In the case of no gradient, the system shows the well studied behavior of LS growth almost immediately, with no slow growth regime. (c) With a gradient in ϕ^s , but allowing for a homogeneous background field (monomer components diffuse infinitely fast), the system also shows no slow growth regime, and enters directly into LS growth, in a like manner to the no gradient case.

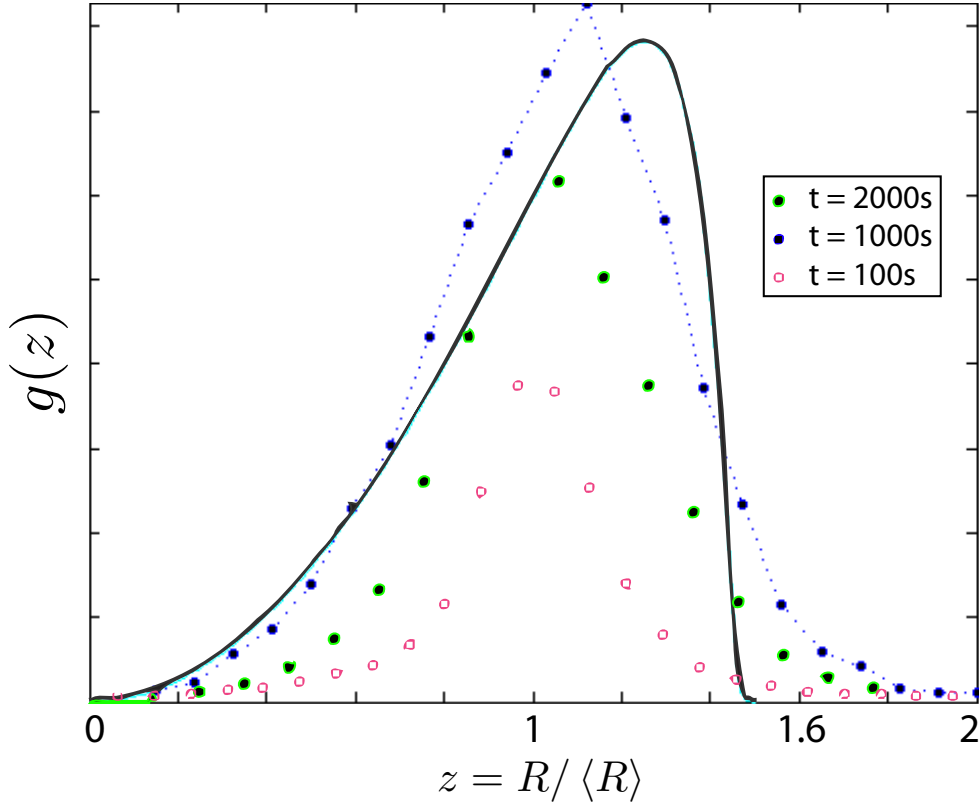


Figure 4.15.: Scaled droplet size distribution function $g(z)$, compared to normalized, scaled droplet radius, $z = R/\langle R \rangle$ (see intro.1.2.1). The black line is the theoretical scaled droplet size distribution function from Lifshitz-Slyozov growth[46]. Different plots correspond to the normalized, scaled droplet distributions from 1018 averaged simulations. For late times, the droplet distribution converges to the LS distribution curve. Since the system is of finite size, this convergence does not coincide for infinite times.

over time, it is continuously maintained throughout the entire process.

This droplet growth model appears to be a reasonable model to describe germ granule segregation. Germ granules preserve proteins and RNAs that would otherwise be broken down within the cell, specifically macromolecules required for the development of the germ layer. Localization by phase transition allows the cell to compartmentalize RNAs and proteins into germ granules, while simultaneously localizing them to the proper region, such that they are in only one cell after cell division occurs. Without this type of compartmentalization a significant amount of cellular resources would be required to actively transport these macromolecules into the proper region.

The non-equilibrium steady state of the system can be described as a single droplet with a source in the posterior and a sink in the anterior. A gradient emerges due to the differential diffusion of the droplet as it changes in size. The properties of the droplet, which causes a system with no gradient to evolve to a single droplet

state, appear to be the same in the case of the gradient. Hypothetically, allowing the droplet surface tension to approach zero, would allow the system to contain multiple droplets, similar to the no gradient case.

Considering the mechanical simplicity of this system, it is likely that localization by phase transition is a process that is not just unique to germ granules. This gradient growth model can give some additional insight into the P granule system, and other systems that undergo the same type of process. As cell division progresses, there are key moments which indicate to the cell that a major global transition should occur, e.g. fertilization of the egg by the sperm, indicates that the cell should undergo symmetry breaking; which sets into motion the proteins required for this to occur. For cell division, what signal(s) are required for the cell to continue and complete the process? In the P cells, the background monomer field, of a specific granule protein, could be a likely possibility. Since this is a global quantity, receptors anywhere in the cell could “know” whether localization of the proper materials have occurred by measuring the local protein concentration, or protein gradient. This type of global signalling, with a minimal number of necessary components, could also be generic to any cell of fixed volume and number of molecules for the activation of other global events within the cell.

In addition to allow for P granule localization, we observe that with a spatial gradient, with a “sufficiently” high nucleation, the system can be maintained at a cyclical non-equilibrium steady with the flux multi-mer droplets in one direction, and monomeric droplet components in the opposite direction. This behavior is not altogether different than the oscillatory behavior of nucleation and growth observed in continuous stirred tank aerosol reactor (CSTR) experiments [50]. Although the dynamics of P granules do not appear to fall into this cyclical regime, it would be interesting to see if such behavior can be found within a cell.

5. Comparison of Theory and Experiment

So far, we have identified the important processes occurring within the *C. elegans* embryo which are necessary for P granule localization, but comparison of experiments with our theory is by far, not trivial. With respect to computer simulations, there are few parameters that can be ascertained directly from experiment, and the kinetics of our theory are only well understood close to the steady state. P granules are clearly not at steady state, and the window of knowledge divulged from experiments is temporally small, making scaling arguments inconclusive. This chapter will focus on a comparison of simulations to the point after symmetry breaking in the *C. elegans*, i.e. $t > -7.5\text{min}$. PNM in figure 2.4. To simplify comparisons, this time will now be redefined as $t = 0$ and referred to as the point of symmetry breaking. All biological experiments were performed by C. P. Brangwynne.

5.1. Determining Simulation Parameters

Few simulation parameters are known directly from experiment. This section states these known parameters, and discusses how all other simulation parameters have been chosen through experimental observations and trends, simulations, and rough calculations with occasional guesswork. All simulation parameters are summarized in table 5.1. This section is organized in a somewhat chronological manner; parameter descriptions and how they were chosen, are stated in the order that they are fixed. It should be noted that how a certain parameter is determined, in this section, can often necessitate prior knowledge of a previously fixed parameter.

System Size

A single cell is roughly ellipsoidal. We take the system volume as a rectangular solid with dimensions equal to the length of the principal axes of the ellipsoid. Although we are interested in what occurs on different sides of the cell, boundary effects are neglected. Within a few micrometers, the single cell *C. elegans*' dimensions are, $\approx 50\mu\text{m} \times 25\mu\text{m} \times 25\mu\text{m}$, where the long axis is the antero-posterior axis (or x axis).

Parameter		Description
Global		
ϕ	0.163	System volume fraction
V	31250 (50 × 25 × 25)	System volume [μm^3]
Molecular Properties		
D	0.2	Monomer diffusion coefficient [$\mu m^2/s$]
v^a	$3 \cdot 10^{-11}$	Cytoplasm monomeric volume [μm^3]
v^b	$1 \cdot 10^{-10}$	Granule monomeric volumes [μm^3]
Free Energy		
$\bar{\gamma}$	$2 \cdot 10^{-3}$	Surface tension coefficient [μm]
η^a, η^b	0.001, 0.001	Bond energies, a-a and b-b
$\chi(0), \chi(1)$	1.6, 1.8	Interaction energy, a-b, at $x(0)$ and $x(1)$
Nucleation		
α	0.001	Nucleation prefactor [$s^{-1} \mu m^{-3}$]
$k_B T$	0.001	Nucleation Exponential Coefficient
Initial Conditions		
$M(0)$	150	Initial Number Drops
$\xi(0)$	0.3 ± 0.1 (†)	Initial droplet size distribution [μm]

Table 5.1.: List of all simulation parameters used to replicate P granule in the single cell *C. elegans* embryo. Droplets are randomly distributed throughout the entire system, where (†) their initial size is a normal distribution defined by $\xi(0)$. See section 5.1 for full details each parameter, and how it is chosen.

Monomeric Volumes

We assume for our binary fluid, that the cytoplasmic component has the properties of water. Using the known molar mass of H_2O , ≈ 18.02 g/mol, and density, $= 1000$ kg/ m^3 , the molecular volume of water is then $\approx 3 \cdot 10^{-11} \mu m^3$.

It should be noted, that although each H_2O molecule has a bond length of ångstroms, giving a volume of order $10^{-10} \mu m^3$, empirical evidence shows that molecules pack more tightly than what one would expect from just the molecular length. The structure of the granule component is not known, in fact, considering the array of proteins and RNA's that do make up P granules, the granule component per se, does not truly exist. We initially define our “effective” granule component based on the knowledge we have of the protein Pgl-1, which as of yet, has an undetermined 3D structure. Considering Pgl-1 to be of nanometer length, and assuming that, just like water, it packs an order of magnitude closer than this length, it's molecular volume would then be of order $\approx 10^{-10} \mu m^3$.

5.1.1. Free Energy Parameters from Experiment

Bond Energy of the Free Energy Density

The bond strength of the cytoplasmic component is assumed to also to have the properties of water. Using the strength of a hydrogen bond in water, ≈ 10 kJ/mol [79], Avogadro's number, and its molecular volume, we calculate its bond energy to be of order $\eta^a \approx 0.001$ (see appendix B for definition of bond energies). Nothing is known about the bond energy of the granule component. For simplicity, it is assumed to have the same bond energy as water. It should be noted that with the limited information about the P granule system, η^a and η^b have been chosen such that they are negligible parameters in the model. The key point being that, for some values, η^a and η^b , one must choose the interaction energy, χ , and surface tension parameter, $\bar{\gamma}$, to give a proper equilibrium description of the system for some initial conditions. Since the entropic term of the free energy density is of order $\nu \approx 0.3$, these enthalpic bond energy terms have no significance. Thus, any choice of η^a and η^b of order less than ν , has negligible impact on the system.

Droplet Size as a Constraint

After symmetry breaking, we see that the number of observable P granules in the posterior is relatively constant, while their number decreases in the anterior (figure 5.1 A1). This supports the hypothesis that droplet size dynamics within this time span are growth dominated, and that nucleation and coalescence of P granules have negligible effects in comparison; in either a nucleation or coagulation regime, one would expect to see the number of P granules in the posterior to increase due to nucleation, or decrease due to fusion of P granules. One does in fact observe small fluctuations in the number of drops even in the posterior, and both P granule nucleation and coalescence have been previously observed in the *C. elegans* embryo [6].

Reexamining now the P granule growth rate from chapter 2 (figure 2.6) we see that the growth rate approaches zero at late times. We thus assume that even though the system is far from equilibrium, the total P granule volume is close to its final size. That is, this volume should be close to the equilibrium size of the system, which is set by the total free energy.

The largest P granules can be up to a few micrometers [78]. To set an upper limit for the equilibrium size, we first assume that that all 80-100 P granules at $t = 300s$ (figure 5.1) have a radius $\approx 1\mu m$. We measure the integrated intensity of the entire cell and see that this quantity is $20\times$ larger than the total intensity of all tracked P granules. Using the assumption that the total GFP intensity is proportional to the total P granule volume, we set an upper bound for the equilibrium size, $R_{eq} \leq 0.1V^{1/3}$. Of course, the system equilibrium size is a spatially dependent quantity changing across the cell due to the saturation gradient. Since this is an upper limit, and as shown in the previous chapter, the granules will collect onto one

side of the embryo due to the gradient, the posterior equilibrium size is set to this value, which becomes a constraint on the free energy parameters.

Thus so far, we have imposed a single constraint (the equilibrium size at the posterior end) onto the three remaining free parameters of the total free energy: the system volume fraction $\bar{\phi}$, the surface tension coefficient $\bar{\gamma}$, and the spatially dependent interaction energy $\chi(x)$. It is known that P granules can be highly varied in size (see introduction 1.1.2), and likely to have a critical size below the resolution of the microscope throughout the posterior. Simultaneously, the critical size must be sufficiently large in the anterior such that all P granules are unstable. We thus require the critical size to be initially, $R_{crit} \leq 1.0\mu m$ throughout the posterior, where in particular, it is $\leq 0.01\mu m$ at the posterior end.

Interaction Energy

With the bond energy parameters and molecular volumes already fixed, only the interaction parameter gradient χ (see Appendix B) of the free energy density must be set. Consistent with our choice of the critical radius in the previous subsection, we impose the constraint that phase separation can only occur on the posterior side of the system. That is, the free energy density has two minima in the posterior, and a single minimum in the anterior. This places a rather limited range for the χ , which is roughly 5 – 6 times the magnitude of ν . We choose χ to vary linearly across the system,

$$\chi(x) = \chi(0) + (\chi(1) - \chi(0))x \quad (5.1)$$

and choose $\chi(0), \chi(1)$ according to our phase separation constraint. The actual range of χ is later adjusted with respect to the other free energy parameters to satisfy the spatial constraints of the critical size, i.e. R_{crit} diverges at the anterior end, and is $\leq 0.01\mu m$ at the posterior end.

Surface Tension and Initial Volume Fraction

The constraints on the equilibrium size at the posterior end, $R_{eq}(1)$, and the critical size at the midpoint of the system, $R_{crit}(1/2)$, are now sufficient to uniquely determine the remaining parameters of the free energy. We thus calculate the final two parameters of the free energy, $\bar{\phi} \approx 0.15$, and $\bar{\gamma} \approx 2 * 10^{-3}$, which state the P granule volume fraction of the entire system, and the P granule droplet surface tension within the cytoplasm.

5.1.2. Parameters Determined From Numerical Simulations

To this point, all stated parameters have come from direct experimental measurements and observations, or assumptions made upon said observations. The following parameters were initially chosen or guessed in the same manner, but subsequent

numerical simulations demonstrated that these values were incorrect. These parameters were thus determined by repeated simulation iterations.

Monomeric Diffusion Coefficient

Initially, the monomeric diffusion coefficient of P granules was set to the measured diffusion coefficient of Pgl-1 from photobleaching experiments (section 2.2.1). Simulations using this coefficient, for a system of appropriate size and number of droplets, show that the system would be clearly in a coagulation regime, where the number of drops decrease due to fusion events on throughout the system, irrespective of the system's free energy. Since all other parameters can be more precisely measured, the data strongly suggests that the initial diffusion coefficient was overestimated. Assuming that P granules follow the Stokes-Einstein relation for spheres, the monomeric diffusion coefficient must then be consistent with the measured diffusion of observable P granules ($R_{max} \approx 1\mu m$). This sets an absolute lower limit on the diffusion coefficient by physical constraints, since P granules monomers must be larger than single atoms. By simulation iterations, the order of magnitude of the diffusion was determined, $D = 0.2 \pm 0.5\mu m^2/s$, which is an order of magnitude smaller than the diffusion coefficient of Pgl-1.

Nucleation

With this new diffusion coefficient, fusion events do still occur, but the system is not dominated by fusion dynamics. The goal is then to determine the nucleation parameters such that, at least for the experimental time span, the nucleation rate is of the same order as that of the fusion rate. The energy to create a droplet of critical size, ΔF^* , changes across the system, and particularly close to the saturation point, can change dramatically. First, $k_B T$ was chosen in a manner such that at least initially, the probability of nucleation is not greater than an order of magnitude from the posterior end of the system to the center, $k_B T \approx 10^{-3}$. Simulations were then run to determine the nucleation prefactor, $\alpha \approx 10^{-3}$.

Initial Conditions

Experiments shows that there are approximately 150 P granules observed within the cytoplasm at symmetry breaking (figure 5.1), and literature suggests, this number can in fact be somewhere between 100-200, and highly varying in size (see Updike, Strome (2009) [78]). Considering that we begin our comparison at the time point where granules start growing in the posterior and shrinking in the anterior, we assume that they are fairly close to the critical size (although this does not have to be the case). Initially, the initial number of droplets is set to $N = 150$, where their sizes were set by a normal distribution about the critical size. As expected, the system did evolve to the proper final state, but the dynamics were clearly different than what is observed experimentally; droplets immediately disappeared in the anterior.

The droplet mean size and distribution width were gradually incremented to find this proper behavior.

5.1.3. Discussion of Parameter Choices

It should be noted, that much of the section discussed initial values of the system, in particular with respect to the R_{crit} . This critical size was discussed in a manner such that there were no droplets existing in the system at $t = 0$. For a fixed $\bar{\phi}$, varying the number and size of the initial number of drops, would clearly change the critical size also. This would mean that for each set of droplets of a certain size, both $\bar{\phi}$, and $\chi(x)$ were adjusted, and then after subsequent simulation runs, α for the nucleation would also then be adjusted.

From the assumptions made, the system volume fraction was determined to be, $\bar{\phi} \approx 0.15$. This would mean that approximately 15% of the cellular volume is P granule material. One may immediately think that this quantity is too large, but with some consideration, the subject becomes more ambiguous. P granules can envelope other organelles, which would indicate that their volume does not necessarily exclude other cellular structures. Reproduction is also quite possibly the most important function of any living organism function. In a fully mature *C. elegans*, the germline takes up nearly half of the worms volume, thus, I would argue, it is not unrealistic that P granules take up such a large volume of the embryonic cell. This of course is somewhat of a hand waving argument, but considering the difficulty of the necessary experimental measurements, not much more can be done at the present.

5.2. Comparison of Data

From the chosen simulation parameters, one can get a reasonable qualitative comparison between simulation and experiment (figures 5.1, and 5.2), where some insight with regards to the biological system can be gained. It should be first noted that, although possible, at the current time it is superfluous to perform simulations that match the experimental trends more precisely for several reasons: At early times, prior to symmetry breaking, there is a larger number of P granules in the anterior of the cell, and both symmetry breaking and the formation of the Mex-5 gradient are not instantaneous events within the cytoplasm. Replicating the gradual gradient formation or the “initial distribution” at this point without more knowledge of how these processes occur would be artificial or ad hoc at best.

Examining the similarity between both the number of P granules and the granule size to simulations, figure 5.1, the data suggests that both experiment and simulation demonstrate the same type of growth behavior, which reaffirms the hypothesis that P granules grow through spatially mediated phase separation. As mainly P granules dissolve in the anterior, while the total granule size increases, it is likely that the

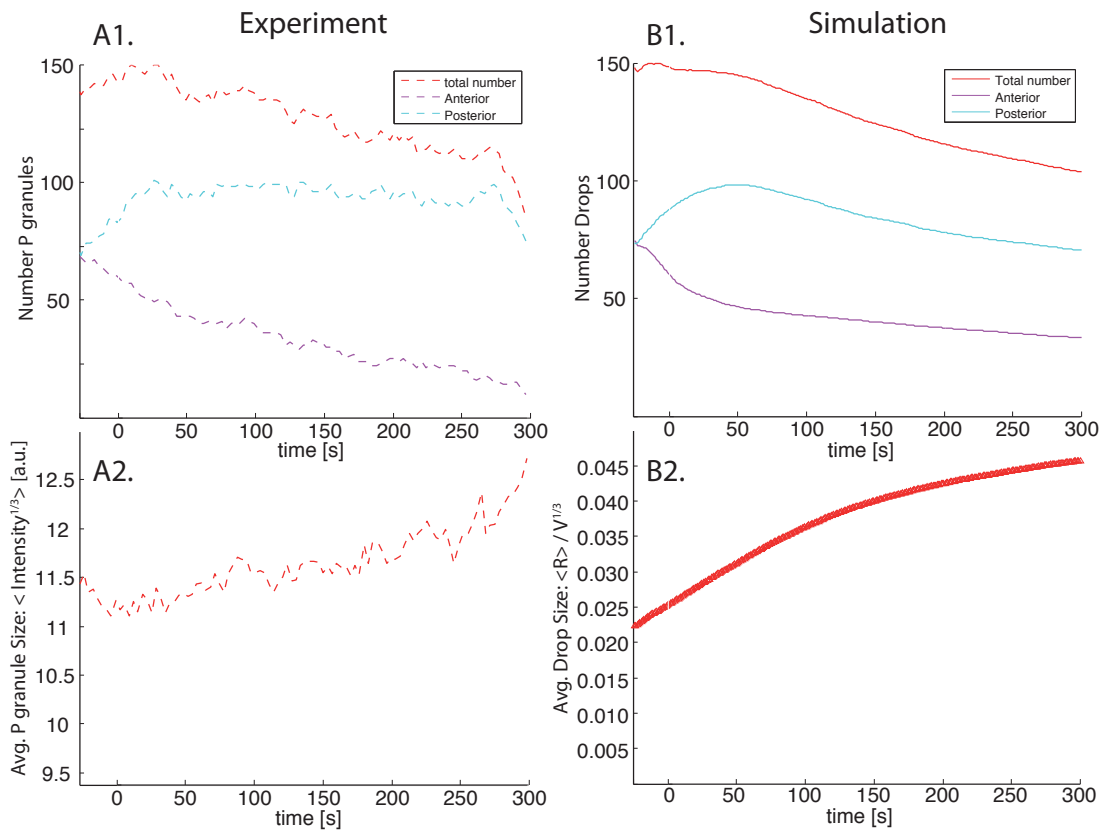


Figure 5.1.: Time evolution of the of P granules compared to simulation. (A1) The time evolution of the number of P granules, and (A2) the average P granule intensity (average size) from a *C. elegans* embryo, as compared to simulations showing (B1) the time evolution of the number of droplets, and (B2) their average size. Experiment performed by C.P. Brangwynne, and intensities plotted are effective intensities (see appendix A.2). Simulation data averaged over 100 simulations.

system is undergoing the slow growth discussed in the prior chapter (section 4.2). That is, one sees a slower growth rate as compared to a $t^{1/3}$ scaling one would expect in a simple, non-spatially mediated growth regime. This hypothesis is further supported by P granule behavior in the last 50 seconds of the experimental data. If the system was in a slow growth regime, one would expect the system to transition to normal growth once nearly all the P granules in the anterior have been depleted. The sudden fall in number of P granules in the posterior and simultaneous increase in P granule volume would suggest exactly this. Of course, the length of the experiment is too short to confirm any scaling behavior, and the sudden increase in P granule size could be due to some other transition occurring within the cell as it begins to divide which is well beyond the scope and understanding of this study.

5.2.1. P granule Distribution

Looking now at the distribution of P granule material (figure 5.2 left), we see that initially P granule material is fairly evenly distributed throughout the system, with a slightly larger concentration at the center of the cell. Eventually a gradient in Pgl-1 forms, as material concentrates within the P granules on the posterior side of the cell, consistent with simulation. It should be noted that at $t = 300s$, the pronuclei from the oocyte is located at $x \approx 0.5$ and the sperm are pronuclei at $x \approx 0.7$. Although we would expect the intensities to continue rising in the posterior, as there are clearly more P granules in the posterior, due to position of the pronuclei, this behavior can not be properly observed.

To get a better understanding of this distribution, we create a simple diffusion reaction model to describe the P granule dynamics, which was done in collaboration with Chiu Fan Lee at the MPIPKS. For simplicity, we assume that all droplets have a typical size v_d . Since we are interested in the steady state solution of this model, the high variance of P granule sizes initially observed, does not undermine this model. The droplet distribution can then be written as,

$$\partial_t n_d = D_d \nabla^2 n_d - k^-(x, \phi_0) n_d + k^+(x, \phi_0), \quad (5.2)$$

where D_d is the droplet diffusion coefficient, k^+ is the rate at which a droplet of size v_d is formed, and k^- is rate at which the droplet is disassembled, assumed to be proportional to n_d . Both the assembly and disassembly rates are dependent on the local level of supersaturation ($\delta\phi = \phi_0 - \phi^s$), which has a spatial dependence due to the Mex gradient ($\phi^s = \phi^s(x)$). This distribution can be written as a global droplet volume fraction,

$$\partial_t \phi_d = D_d \nabla^2 \phi_d - k^-(x, \phi_0) \phi_d + v_d k^+(x, \phi_0), \quad (5.3)$$

with a complementary equation to describe the background monomeric field,

$$\partial_t \phi_0 = D_0 \nabla^2 \phi_0 - h^-(x, \phi_d) \phi_0 + v_0 h^+(x, \phi_d). \quad (5.4)$$

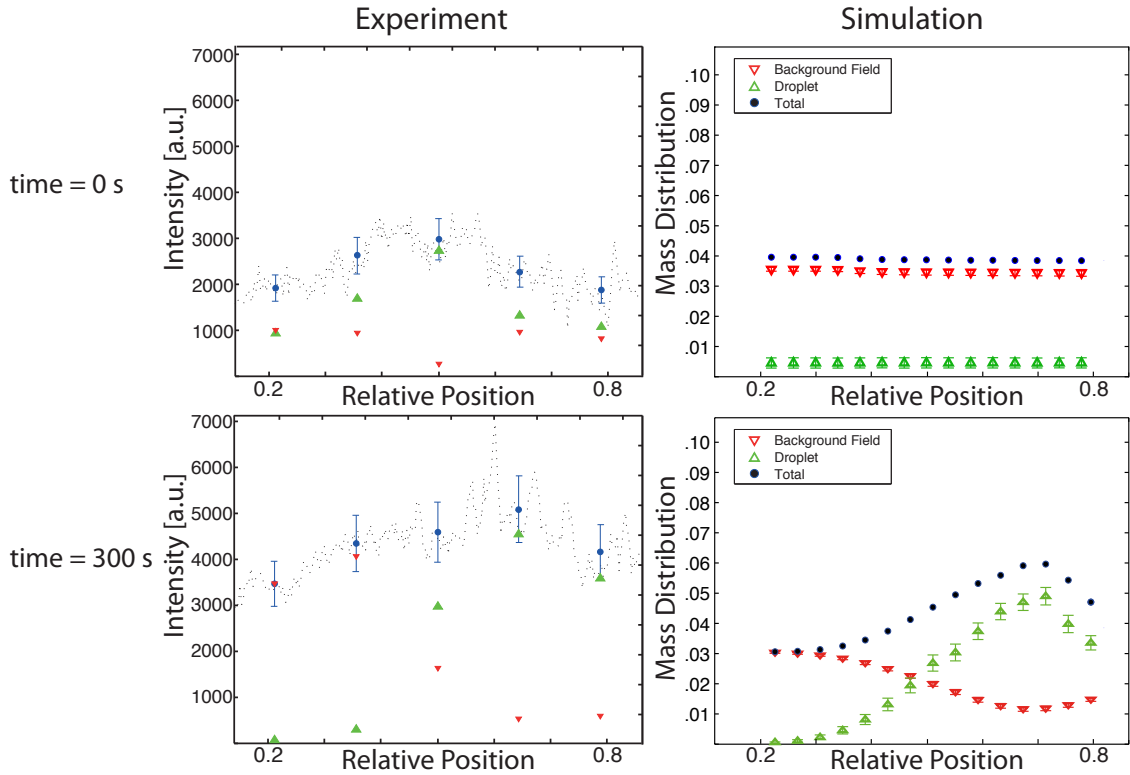


Figure 5.2.: Comparison of concentration distributions. (left) P granule material (GFP::PGL) intensity distribution within a *C. elegans* embryo, and (right) mass distribution of granule components from simulation. The total amount of granule component is shown in blue, the amount within P granules (or droplets) is shown in green, and the amount of material within the cytoplasm (or background) is shown in red. The dashed line in the experimental data is the total integrated intensity across the cell from the boxed region in figure 5.3. This data is then binned (blue dots) and compared to the total P granule intensity across the cell from P granule tracking (green triangles). The difference between these two values (red triangles) should then correspond to the amount of material within the cytoplasm. This cytoplasmic concentration is a rough approximation at best. This is due to the difficulty of subtracting the background intensity, and the fact that both pronuclei are in the center/center right of the cell, which causes a lowered intensity measurement as compared to the actual concentration of P granule material. The background intensities for each image has been subtracted independently of the other, thus the total intensities for both time points are not comparable, although ΔI is still comparable. In simulation, the system is also spatially binned. The mass distribution corresponds to the amount of granule component within the bin, normalized by the total amount in the system, N^b . Error bars show the standard deviation. Experiments performed by C. P. Brangwynne and simulation data averaged over 1000 simulations.

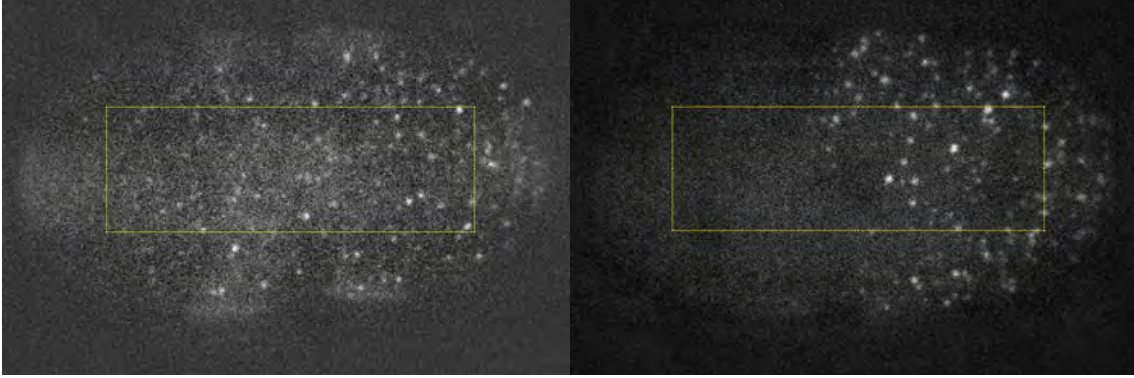


Figure 5.3.: *C. elegans* embryo tagged with GFP::PGL-1, at $t = 0s$ (left) and $t = 300s$ (right). The images are total intensity of all z-stacks. The yellow boxes correspond to the region which is further analyzed (see figure 5.2). The oocyte and sperm pronuclei are the two dark circular regions in the right image. Experiment performed by Dr. C.P. Brangwynne

Here, D_0 is the diffusion coefficient and v_0 is the cytoplasmic monomer volume of the cytoplasmic P granule constituents. The rates h^+ and h^- are respectively, the rates of accumulation and depletion of cytoplasmic P granule constituents due to droplet formation and dissolution. With the assumption that the system is incompressible, volume fraction distributions are equivalent to mass distributions. Thus by conservation of mass, the rates of the last two equation must be equal,

$$v_d k^+(x, \phi_0) = h^-(x, \phi_d) \phi_0 \quad (5.5)$$

$$k^-(x, \phi_0) \phi_0 = v_0 h^+(x, \phi_d). \quad (5.6)$$

To make this problem analytically accessible, we look at a simplified case: a one dimensional system, where growth occurs only in the posterior, and dissolution only in the anterior, both at constant rates,

$$v_d k^+(x, \phi_0) = \alpha \Theta(x) \phi_0$$

$$k^-(x, \phi_0) = \beta \Theta(-x).$$

Thus, α and β are constants that represent the effective rates of conversion of between ϕ_d and ϕ_0 , and $\Theta(x)$ is the Heaviside step function. In this manner, the rates k^\pm , mimic the saturation gradient dependent growth, such that in the anterior, $x < 0$, the system is in a single phase state and all droplets disappear at a rate $\beta \phi_d$, while the system is in the two phase state in the posterior, $x > 0$, and the cytoplasm is converted into droplets at a rate of $\alpha \phi_0$. With these simplifications, the steady state solution for equations (5.3), (5.4) can now be obtained. Incorporating no flux boundary conditions at both ends of the system ($x = \pm L/2$),

$$\phi_d(x) = \begin{cases} K \frac{\cosh(\beta_d(L/2+x))}{\cosh(\beta_d L/2)}, & x < 0 \\ K \left(1 + \frac{2 \tanh(\beta_d L/2) \sinh(\alpha_0 x/2) \sinh(\alpha_0(L/2-x/2))}{(\alpha_0/\beta_d) \sinh(\alpha_0 L/2)} \right), & x \geq 0 \end{cases} \quad (5.7)$$

$$\phi_0(x) = (K - \phi_d) D_0/D_d. \quad (5.8)$$

Here, $(\alpha_0)^2 = \alpha/D_0$, $(\beta_d)^2 = \beta/D_d$, L is the system length (from $-L/2$ to $L/2$), and K is a constant proportional to the total volume of P granule constituents within the cell.

Using the diffusion coefficients determined from simulation (see prior section), this model is now fit to the previous distribution, figure 5.4. Again, due to the

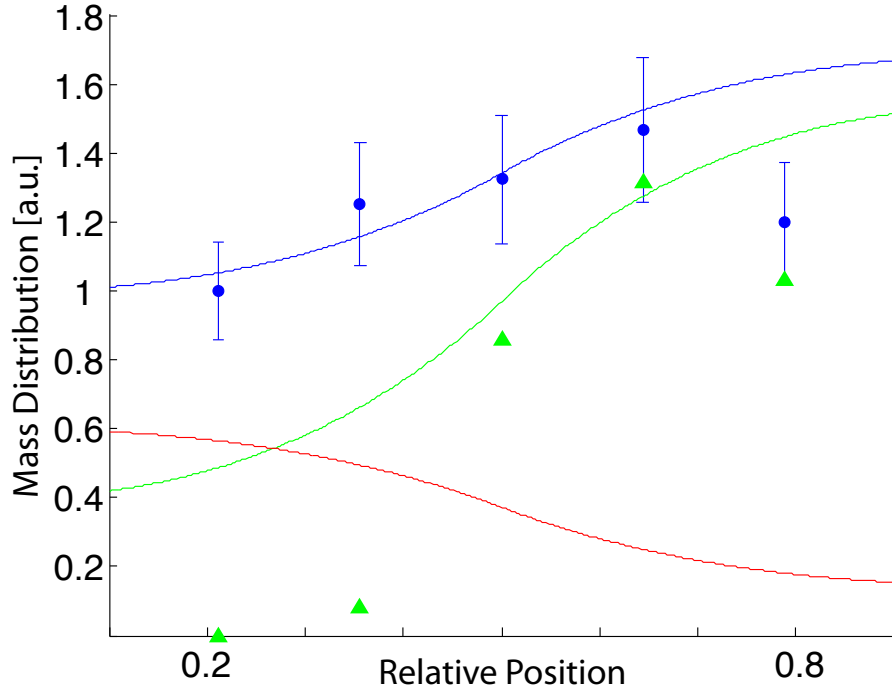


Figure 5.4.: Comparison of analytical model at steady state model with P granule distribution. The P granule constituents within P granules ϕ_d is shown in green, the background material ϕ_0 in red, and the total P granule material $\phi_{tot} = \phi_d + \phi_0$ is shown in blue. The data points shown are corresponding experimental data from GFP::PGL in the *C. elegans* embryo. Both sets of data have been normalized using the anterior most point. For the model, the system length was determined by measurement of the *C. elegans* embryo, $L = 50\mu m$, the diffusion parameters were taken from those determined by experiment $D_d = 0.08\mu m^2/s$ (see Chapter 2), and simulation $D_0 = 0.2\mu m^2/s$ (prior section). All other parameter values were chosen to fit the experimental data, $K = 20$, $\alpha = 2.0 \cdot 10^{-4}s^{-1}$ and $\beta = 5 \cdot 10^{-4}s^{-1}$.

position of nucleus and boundary effects, there are some discrepancies between the model and the experimental results. In this, so called steady state distribution, we observe that the concentration of P granule constituents within the posterior is roughly 1.5 times that of the anterior (which is likely to be an underestimate to the pronuclei). From this model, we observe that a stronger localization of P granule material can occur by varying the growth or dissolution parameter, α, β . Since the actual P granule growth rate is set by the Mex-5 gradient through the free energy, it is possible to induce a much stronger localization of P granule material with a

smaller Mex-5 gradient. This might be in fact necessary for later cell divisions, as the amount of Mex-5 in P lineage cells decreases.

5.3. Later Cell Divisions

Simulation data can give some insight into the dynamics of subsequent cell divisions. Since the embryo is contained within an egg shell, we know that the size of daughter cells are roughly half the size of the parent cell, and in the case of the progenitor germ cells, they are in fact less than half the parent's size (see figure 1.4 for a basic overview of this process). The amount of granular material that is localized to the posterior, as of yet, has not been unequivocally quantified. Prior works suggest that this concentration is doubled after the first cell division [22]. What happens to the system if the system volume is halved and the initial concentration of granular material is doubled, while all other parameters are kept fixed? Due to the increase in the droplet density, the system switches into a coagulation growth regime; the droplet number and size are dictated by droplet coalescence (figure 5.5). We of course would only expect this to occur in the embryo if the total droplet volume were the same in both the P0 and P1 cells, which although not properly measured, does not have to be the case. On the other hand, it should be mentioned that this coalescence behavior dominates, independent of droplet growth and nucleation rates, which have also significantly increased due to the greater level of supersaturation. Although it is not clear that the P1 cell has entered the regime of fusion mediated growth, we would expect this transition to eventually occur with subsequent cell divisions, quite possibly by the 3rd or 4th cell division, where they become more and more localized to the cell nucleus.

The decrease in cell volume and increase in concentration of P granule material leads to an increase in the supersaturation of the entire system. Little is known about Mex-5 at this stage. If the concentration of Mex-5 is kept fixed at the two endpoints of the cell (as we have done), the Mex-5 gradient would double in magnitude and lead to a significant increase in growth and nucleation rates of P granules, leading to a more efficient localization of P granules. It is also possible that Mex-5 has become significantly depleted by the second cell stage, since no protein translation occurs this early in embryogenesis (see intro 1.1.2 and the majority of Mex-5 was in anterior of the cell prior to cell division (figure 2.10)). Due to the decrease in Mex-5 concentrations, a greater volume fraction of P granule material does not mean a greater supersaturation as compared to the one cell stage. This greater concentration may be necessary to “compensate” for the decrease in the Mex-5 gradient, which would lead to an increase in ϕ^s throughout the system.

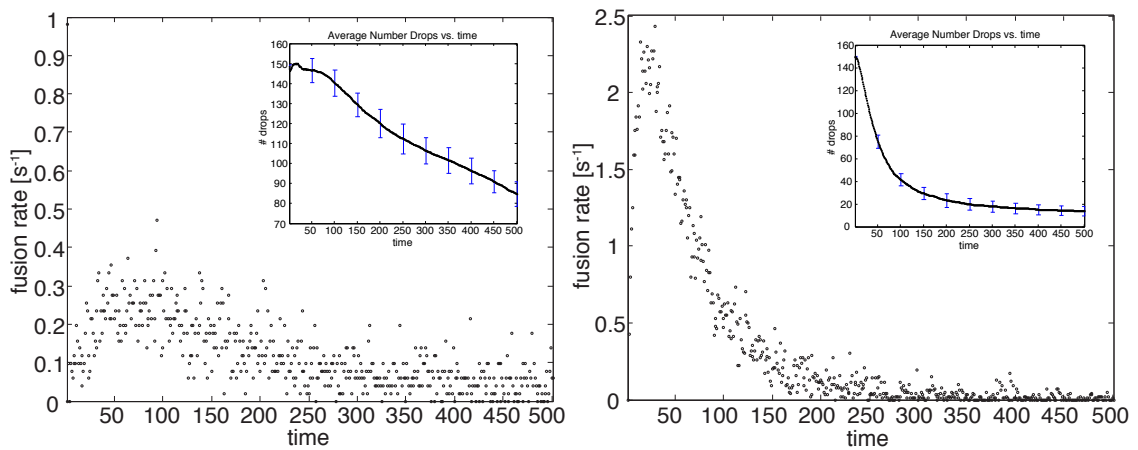


Figure 5.5.: Droplet Fusion rate versus time, from (left) simulations of the single cell stage and (right) simulations of the two cell stage. Nearly all parameters come from table 5.1, except the system length is halved and the system granule concentration is doubled, i.e. $V_{2cell} = \frac{1}{2}V$, $\bar{\phi}_{2cell} = 2\bar{\phi}$, for the two cell stage. The time evolution of the number of drops, for each system is placed in boxes for easy comparison.

6. Summary and Conclusions

In this study, we have determined the mechanism for germ granule localization within the *C.elegans* embryo. From this data, we have developed a theoretical framework to describe how spatial localization can occur due to a background gradient.

6.1. General Summary

Experimental Analysis

From experimental data of the single cell *C. elegans* embryo, we have determined that P granule localization can not occur due to cytoplasmic flows, and likely to occur through spatially mediated growth. This spatially mediated growth changes throughout the lifetime of the cell, but is in particular, controlled by the protein Mex-5. The formation of a Mex-5 gradient is necessary for P granule localization.

P granules have been also observed to have droplet properties, and thus, can be described as liquid droplets within a liquid cytoplasm. Some liquid properties of granules have been determined: Within these liquid P granules, the diffusion coefficient of the protein constituent Pgl-1 was measured. Using tracking data, the diffusion coefficient of different size (intensity) P granules has also determined.

Theoretical Model

Using experimental observations as a starting point, a theoretical model of P granules has been developed: a binary two phase fluid that can undergo liquid-liquid phase transitions. This model is based on droplet nucleation growth models. In addition, to allow for droplet localization, i.e.inhomogeneous growth, a spatial gradient was added to the saturation point by utilizing the free energy of the system. This addition of a spatially dependent saturation point builds upon the dynamics within the field of 1st order phase transitions, allowing both inhomogeneous concentrations and fluctuations throughout the system.

Simulation Study of the Gradient

Simulations were performed to study the effects of the spatially dependent gradient within the droplet growth model. It was determined that with inhomogeneous growth, the background concentration field takes on a new importance. It is no

longer globally homogeneous, and theories that use this approximation become invalid. In fact, it forms a gradient in the opposite direction as the droplet growth gradient due to depletion from droplet growth. Because of this background depletion, droplet growth occurs at a slower rate than in the comparable homogeneous growth cases at early times. At later times, when all droplets have spatially localized, the system behaves again like the homogeneous system.

For large diffusion coefficients (or for very long times), the gradient allows for a cyclical, ensemble steady state. Droplets nucleate and grow in one region, but eventually diffuse to another unstable region where they dissolve. The dissolved material in the background then diffuses back to the metastable region allowing for new droplets to nucleate and grow. In sum, a steady state is created with a net flux of droplets in one direction, and a net flux of droplet constituents within the background in the opposite direction.

The gradient in effect prevents the system from relaxing to a final equilibrium, and creates a cyclical non-equilibrium steady state. This type of behavior is similar to what has been observed in open systems that undergo nucleation and growth, where one observes temporal oscillations in phase transitions, e.g. [16, 56, 65]. Models of open systems showing this type behavior have also been developed in the study of aerosol clouds, in particular with respect to weather forecasting and climate prediction [49].

Experimental Comparison

Simulations were performed to duplicate experimental observations. From these simulations, it appears likely that P granules exist in a slow growth regime. Upper and lower bounds for their diffusion coefficients have also been determined. It has also been determined that this type of nucleation and growth behavior observed in the single cell stage are unlikely to dominate P granule dynamics in later cell stages.

6.2. Future Outlook

Given the generic nature of our model, we believe this approach can be used to study other membraneless assemblies within the cell, such as Cajal bodies, and stress granules. In addition, the ramifications of a gradient dependent free energy has not been completely understood. Probably the most important work that is required is a better understanding of the slow growth regime. Although we have identified a slow growth regime due local depletions, the properties of this regime have not as of yet been properly studied. How much slower is it as compared to the homogeneous case? Since this is a diffusion limited growth case, we would expect this rate to scale with system size (for evenly distributed particles), but proper analysis is still required.

From theory and experimental observations, many things can be said with respect to possible directions for future endeavours in the study of granules. Although

from this study we have concluded that cytoplasmic flow fields have a negligible effect on P granule localization, it does have some effect. A majority of P granules appear unaffected by the flow field, but a few are observed to “flow” with either the cytoplasmic field, or due to some other unknown cause. Hypothetically, this could be due to granules enveloping certain molecules that are themselves transported, which inadvertently drags along the granule. A more conclusive understanding of the effects of flow and its “arbitrariness” on P granules could shed light on the stability of structures within the cytoplasm that are not fixed in place, e.g. by the cytoskeleton.

From theory, it is believed that germ granules are in a slow growth regime. Due to the short time span of experiment, this can not be verified. By delaying the next stage of cell division, this behavior could be observed, in particular with transition to normal growth once most granules have localized to the posterior.

We also predict a significant change in granule dynamics in later cell divisions. Similar measurements, as have been presented here, for subsequent cell divisions of the P lineage cells could show when P granules shift from a nucleation and growth regime into a coagulation regime. In general, precise measurements of the concentration of P granules throughout the cell is difficult due to many factors (see e.g. figure 5.3). An accurate assessment of how much P granule material is localized to the posterior is difficult to make due to the position of the nucleus, background noise, and other less significant effects. Observation of P granule behavior in later cell stages could possibly place an upper limit on how much material is localized in the previous cell stage. To be more specific, if the second cell stage does not fall into the coagulation regime, ignoring other possibly new factors, an absolute limit can be placed on the amount of P granule material that has been localized prior to cell division. This of course depends on how the saturation point of the system changes after cell division; how much granule component still resides within P granules and not freely in the cytoplasm.

Probably the most interesting bit of knowledge obtained from theory pertains to the background field within the cell. With asymmetric growth of P granules, an opposite gradient is created in the cytoplasm. Although granules are discrete organelles that localize to “one” region, the gradient in the background field is better described as a continuous global quantity. How does a part of the cell “know” when something has occurred in a distal region of the same cell? We propose that this gradient, and similar ones, could play a role in cell signalling. In this specific case, local measurement of a key P granule constituent in the cytoplasm, or its gradient, would allow distant points in the cell to determine if P granules have sufficiently localized to the posterior such that a new cellular event can occur.

In sum, we have developed a theory to account for spatial organization through phase separation with the utilization of a gradient. Although this theory has been specifically applied to germ granules, it is generic, and can be applied to other biological and non-biological cases. I must admit, that the P granule system is an ideal system to observe and study localization due to phase separation, which I can

not take any credit for choosing. That said, localization by gradient is not a unique feature to this system, and with the discovery of this property within P granules, it is likely that many other systems will be observed with similar properties. From a biological perspective, this type of localization demonstrates a more fundamental type of pattern formation, as compared to e.g. the use of molecular motors. With the ability to describe a biological system using the formalism within statistical mechanics, instead of a purely phenomenological approach, we take a step closer to describing and understanding biology from basic physical principles...albeit a minute step.

Appendix

A. Determining the Diffusion Coefficient of P granules

For some body, one can calculate its diffusion coefficient by measuring the mean squared displacement of the object with respect to the elapsed time; where, for a purely diffusive object, the actual mean displacement will be ≈ 0 . As objects increase with size, the diffusion of the object decreases due to the increase of drag within the medium. For spherical objects with radius R , at low Reynold's number, this decrease in diffusion is given by the Stokes-Einstein relation,

$$D = \frac{k_B T}{6\pi\eta R}, \quad (\text{A.1})$$

where η is the viscosity of the medium. Thus for spherical objects, diffusion should decrease as $\propto 1/R$.

To determine the diffusion coefficient of P granules, two factors need to be accounted for: P granule advection due to cytoplasmic flow and the size of P granules.

A.1. Advection

Using tracking data from wild type P granule embryos, the average velocities were measured, and the velocity distributions within the embryo were observed, see figure A.1. A non-zero mean velocity of P granules is measured on the posterior side of the embryo, fig.A.1B. Comparison of this data with the distribution of velocities, fig.A.1C, shows that the mean velocity is not necessarily indicative of P granule behavior, and that the median velocity is a better description of the average velocity. Although there are a few granules that are moving with “high” velocities due to cytoplasmic flow, the majority appear unaffected by flow. That is, the advection of P granules could in fact be a red herring, and it is quite possible that P granules per se, are not effected by intracellular flow. It is possible that occasionally a granule binds or envelops other objects, which then proceed to carry them; quite often, but not necessarily with the cytoplasmic flow. This conjecture is supported by the fact that there are almost as many posterior flowing granules as anterior flowing, and it is commonly observed that P granules can occasionally envelope large structures such as centrosomes [78]. This would mean that P granules do not advect on their own, but are occasionally carried by objects which are affected by cytoplasmic, or other flows. For the calculation of P granule diffusion, it is thus sufficient to measure the mean square displacement of the “0-velocity” granules and ignore advection.

A.2. Size and Intensity

With GFP labeling of proteins, the optimistic expectation is that fluorescence intensity increases proportionately with the number of existing labeled proteins. Hypothetically one could then determine the size of a polymeric protein by measuring the total GFP intensity of this single protein, knowing the intensity a GFP molecule attached to its monomeric component. This of course is not necessarily the case, and many factors, such as deconstructive interference of densely packed particles, can significantly alter this proportionality. GFP labeling has been tested in-vitro with GFP::PGL-1 where this proportionality has been shown to hold [36]. For the purposes presented here, it will be assumed that this proportionality is also valid for GFP::PGL-1 within the *C. elegans* embryo.

It is though necessary to take into account the loss of intensity with respect to different z -planes of the same embryo. As one images through an embryo, moving further away from the surface plane, there is a loss of intensity. Thus for any given z -plane, we can measure the GFP intensity of Pgl-1 and discuss the comparative sizes of P granules within that z -plane, but to compare granule data from multiple planes, the GFP intensity must be normalized to take into account the incurred change of intensity for each z -plane.

Since the particles in question are small, we assume that gravity is negligible in our system, and thus assume that there should exist no significant systematic differences in the general make up of any z -plane, i.e. P granule size distributions should be the same for all z -planes. Examining the intensity distributions for separate z -planes, we see that this is not an unreasonable assumption, as each distribution appears had a similar shape, a half binomial distribution, figure A.2A. Each z -plane distribution was thus fit to a 2 parameter normal distribution, $f(x) = Ae^{-(x/\sqrt{2}\sigma)^2}$. Defining a wellness of fit,

$$Q = \frac{\sum (f(x_i) - y_i)^2}{\sum y_i^2}, \quad (\text{A.2})$$

we see that for all fits, $Q < 0.05$. Excluding the top and bottom z -stacks due to an insufficient number of particles (and possibly other not so well understood problems related to surface boundaries), the fit parameters, A and σ , show a strong linear dependence on z (figure A.2B & A.2C). Using this linear dependence, all the original data was collapsed into a single distribution with a new, effective intensity (figure A.2D). This effective intensity was then used to analyze P granule data from multiple stacks.

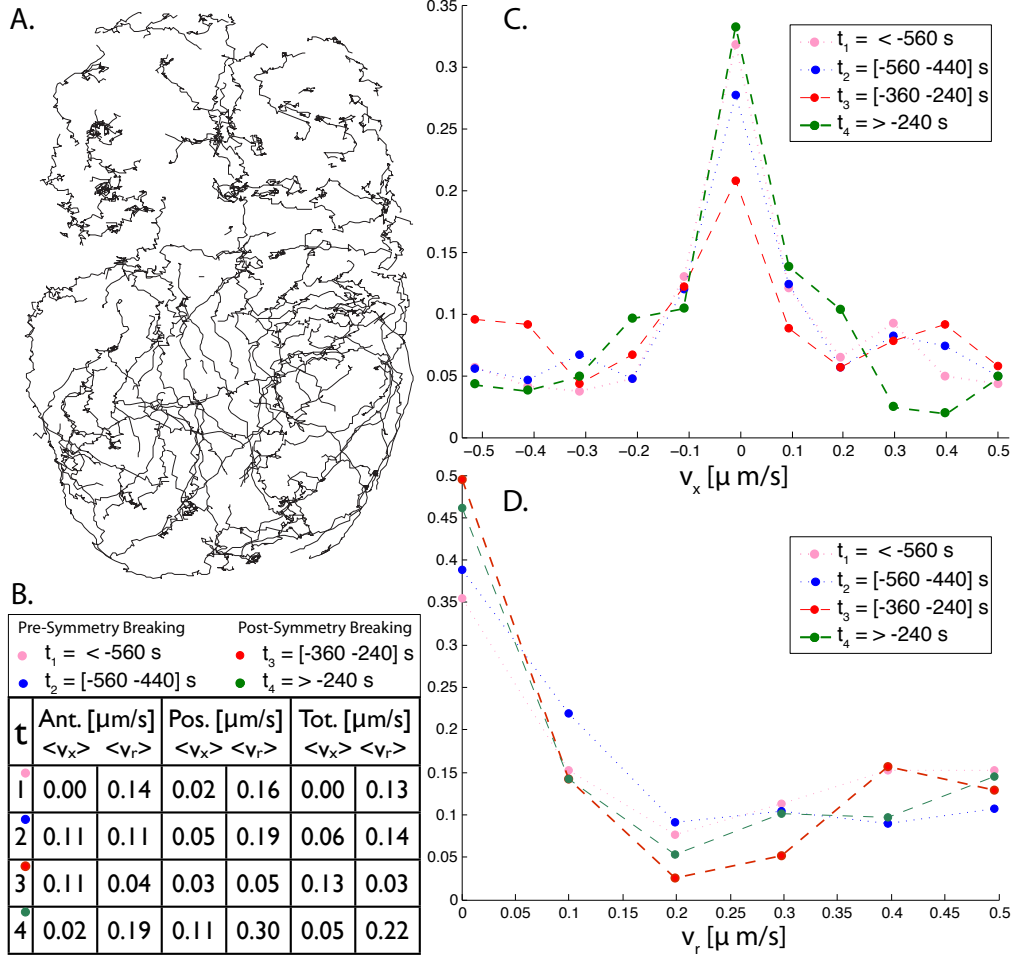


Figure A.1.: Measurement of mean and median P granule velocities from (A) Particle tracking data from a single *C. elegans* embryo. B) The mean velocities in the x-direction, $\langle v_x \rangle$, and the magnitude of the radial velocity, $\langle v_r \rangle \equiv \sqrt{\langle v_y \rangle^2 + \langle v_z \rangle^2}$ are shown at different times with respect to pro-nuclear meeting (pnm). Symmetry breaking occurs at $t \approx -400\text{s}$, which is right in the middle of the data shown. There is a clear mean velocity close to this time towards the posterior, although this velocity is always comparative in size to the radial velocities in the same region. The velocity distributions in the x-direction (C) and the radial direction (D), are shown for the same time points. Although there is a mean velocity towards the posterior, the median and mode velocities are ≈ 0 , prior to, and after symmetry breaking.

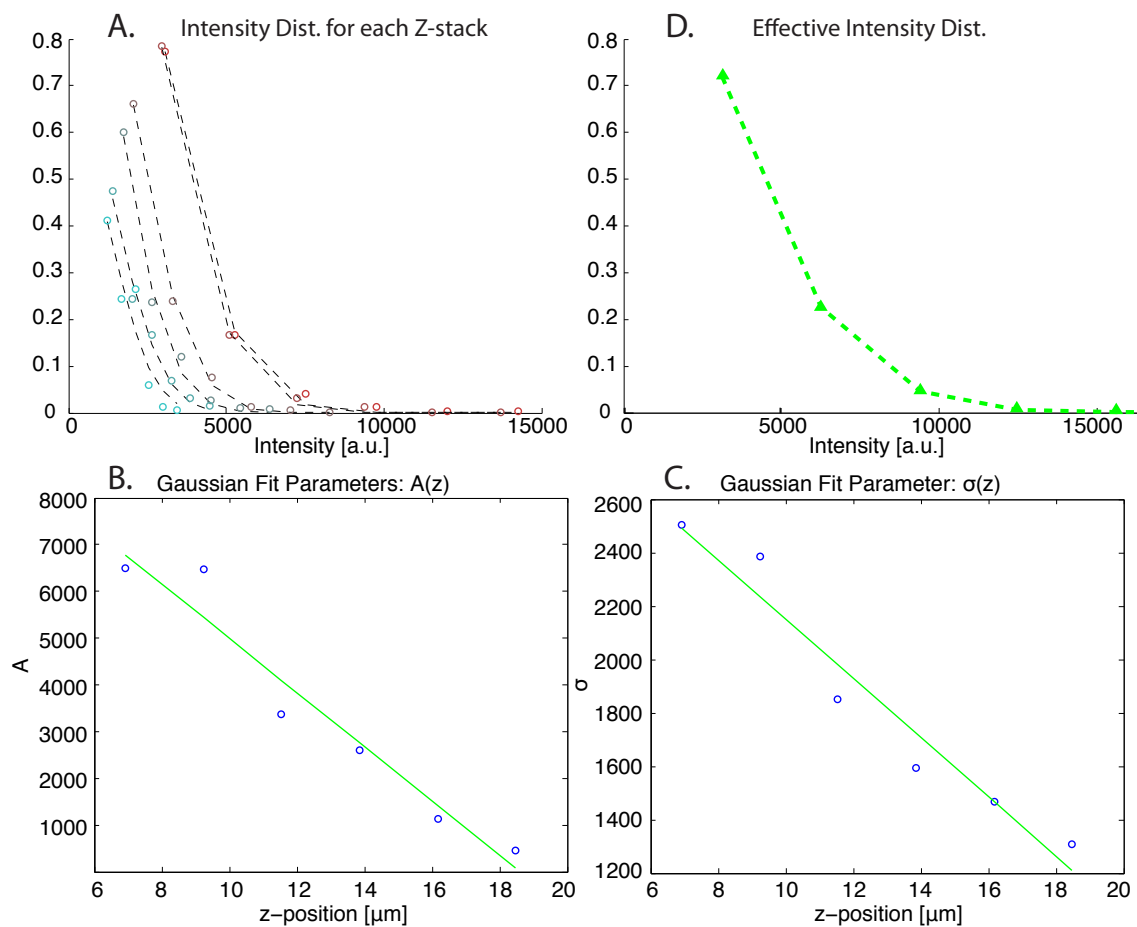


Figure A.2.: Intensity Distribution of P granules. (A) Intensity distribution of P granules of disparate z-stacks, where each distribution is fit by a Gaussian function $f(x) = Ae^{-x^2/2\sigma^2}$. (B)(C) The linear z dependence of the fit parameters, A and σ . This data is then used to collapse all z-stacks into a (D) single “effective” intensity distribution.

B. Flory-Huggins Free Energy

The Flory-Huggins free energy is a generalization of the regular solution. It was initially developed to describe the correction to the free energy of polymers, due to the different size of components, in solution [19, 20]. The key difference lies in that Flory-Huggins takes into account the different monomeric volumes between solute and solvent where the regular solution assumes that they have equal volumes. This is in fact commonly the case in biology, where the solvent is mainly water, and the solute can be large protein polymers, either chain like or globular.

The energy can be written in the general form $F = U - TS$, where U and S are respectively the enthalpic and entropic term. For a two component fluid (components “ a ”, and “ b ”), in a closed system with total volume V , described by the volume fraction ϕ ,

$$U = V \left(\frac{zw^{aa}}{2} (1 - \phi)^2 + \frac{zw^{bb}}{2} \phi^2 + z \left(w^{ab} - \frac{w^{aa} + w^{bb}}{2} \right) (1 - \phi) \phi \right)$$

$$S = -Vk_b \left(\frac{1 - \phi}{v^a} \ln(1 - \phi) + \frac{\phi}{v^b} \ln \phi \right).$$

The coordination number, z is the number of bonds that each “ a ” molecule makes, w^{aa}, w^{bb}, w^{ab} are the bond energies per unit volume between the corresponding molecules, and v^a, v^b are the molecular volumes of each component.

We redefine the free energy to make the energy densities dimensionless, and thus for a system with “ m ” homogeneous minority phases, in a single solution, the redefined energy is,

$$F(\{\phi\}_{i=1}^m, \{V\}_{i=1}^m) \equiv F \frac{v^a}{k_B T} \tag{B.1}$$

$$= V_0 f(\phi_0) + \sum_{i=1}^m (V_i f(\phi_i) + \bar{\gamma} S_i), \tag{B.2}$$

$$\tag{B.3}$$

with energy density,

$$f(\phi) = \eta^a (1 - \phi)^2 + \eta^b \phi^2 + \chi (1 - \phi) \phi + (1 - \phi) \ln(1 - \phi) + \nu \phi \ln \phi. \tag{B.4}$$

The majority phase, defined by ϕ_0, V_0 , is dependent on the minority phase as per, equations (3.26), (3.27). The surface tension parameter, $\bar{\gamma}$ (referred to only as γ

in the main text), and S_i is the area of the interface between the minority droplet phase, and majority phase. The new parameters are then,

$$\eta^a = \frac{zv^a}{2k_B T} w^{aa} \quad (\text{B.5a})$$

$$\eta^b = \frac{zv^a}{2k_B T} w^{bb} \quad (\text{B.5b})$$

$$\chi = \frac{zv^a}{2k_B T} \left(w^{ab} - \frac{w^{aa} + w^{bb}}{2} \right) \quad (\text{B.5c})$$

$$\nu = \frac{v^a}{v^b} \quad (\text{B.5d})$$

$$\bar{\gamma} = \frac{v^a}{k_B T} \gamma \quad (\text{B.5e})$$

Here, η^a, η^b are referred to as the unitless bond energies, and χ is the unitless interaction energy. The disadvantage of using the Flory-Huggins free energy is the actual form. The logarithm terms, make it a rather unruly energy to work with for analytical calculations as compared to simple polynomials. On the other hand, the advantage lies in that fact that this energy is based on a physical description of the system. It can be derived from a lattice model, which describes the molecular interactions between each molecule. Thus system parameters can be possibly attained with an increased understanding of the biological system. As mentioned initially, this energy describes the interaction between enthalpic and entropic terms. It has the required property of two minima below the critical point, where the enthalpic term allows for two phases. As entropy dominates, the system enters a single mixed state, and thus satisfies the conditions set by Cahn-Hilliard.

C. Balance of Droplet Growth with Exterior Particle Flux

Using conservation of mass, a droplet growth term is derived from its exterior particle flux within an incompressible binary fluid. Superscripts "a", and "b" refer to their corresponding components and the superscript "α" refers to a generic component, while subscripts "0", "1" refer respectively to the cytoplasmic and droplet regions. Components without a superscript refer to the sum of both components. Separate to what has been presented in the main text, this derivation is done using particle densities and fluxes (not volume fraction), to explicitly show the conservation properties used in this derivation. Variables that represent properties of the volume fraction, e.g. the volume fraction flux, will be explicitly labeled by a ϕ superscript.

For an incompressible binary fluid within a closed system, the relationship between particle densities and volume fraction is,

$$\phi = \rho^b v^b \quad (\text{C.1})$$

$$1 - \phi = \rho^a v^a, \quad (\text{C.2})$$

where v^a, v^b are the molecular volumes of each component. Thus, e.g. J_0 the total particle flux of both components within the cytoplasm, $J_0 \equiv J_0^a + J_0^b$, in relation to the volume fraction flux, J_0^ϕ , would be,

$$J_0 = J_0^\phi \left(\frac{1}{v^b} - \frac{1}{v^a} \right). \quad (\text{C.3})$$

We start with the local continuity equation for each component,

$$\frac{\partial \rho^\alpha}{\partial t} = -D \nabla^2 \rho^\alpha, \quad (\text{C.4})$$

where using Fick's law, $\mathbf{J}^\alpha = -D \nabla \rho^\alpha$, we write the conservation of both components for an arbitrary volume \mathcal{V} , as,

$$\int_{\mathcal{V}} \frac{\partial}{\partial t} (\rho^a + \rho^b) d\mathcal{V} = - \int_{\partial \mathcal{V}} (\mathbf{J}^a + \mathbf{J}^b) \cdot d\mathcal{A}. \quad (\text{C.5})$$

Since we will be considering moving boundaries, the Leibniz Rule is used to differentiate within the integral, such that the full time evolution of our volume is also taken into account,

$$\frac{d}{dt} \int_{\mathcal{V}} \rho d\mathcal{V} = \int_{\partial \mathcal{V}} \left(\rho \frac{d\mathbf{q}}{dt} - \mathbf{J} \right) \cdot d\mathcal{A}, \quad (\text{C.6})$$

where $d\mathbf{q}/dt$ is the velocity of the moving boundary.

We consider now a system with a closed system with total fixed volume V , and total number particles N^a , N^b . More specifically, a 2-phase system consisting of a spherical droplet of volume V_1 within a cytoplasm of volume $V_0 = V - V_1$. As defined by equation (C.5), the positive flux is defined as leaving some volume, thus the positive mass flux of each region moves particles out of that region, while a positive velocity of the boundary region increases the volume of that region. For our closed system with fixed volume V , and fixed total number of particles, the left side of equation (C.6) for the entire system goes to zero,

$$\frac{d}{dt} \int_V \rho d\mathcal{V} = 0, \quad (\text{C.7})$$

leaving only the boundary term between cytoplasm and droplet,

$$\int_{\partial V_0} \left(\rho \frac{d\mathbf{q}}{dt} - \mathbf{J} \right) \cdot d\mathcal{A} + \int_{\partial V_1} \left(\rho \frac{d\mathbf{q}}{dt} - \mathbf{J} \right) \cdot d\mathcal{A} = 0. \quad (\text{C.8})$$

In the simple case where we have spherical symmetry of the mass densities (which implies spherical symmetry of the flux, assuming Fick's Law holds), for a spherically symmetric droplet with radius R , the above equation simplifies to,

$$\frac{dR}{dt} (\rho_1(R) - \rho_0(R)) - J_0(R) + J_1(R) = 0. \quad (\text{C.9})$$

We assume that the relaxation time for ρ within the droplet is much faster than the relaxation time for ρ outside of the droplet. The droplet growth occurs on this slower, diffusion dependent, timescale; i.e. $J_1 \ll J_0$, such that,

$$\frac{dR}{dt} = \frac{J_0(R)}{\rho_1(R) - \rho_0(R)}. \quad (\text{C.10})$$

For a binary fluid, this equation can be expressed in terms of the volume fraction, and volume fraction flux,

$$\frac{dR}{dt} = \frac{J_0^\phi}{\phi_1(R) - \phi_0(R)}. \quad (\text{C.11})$$

Note that equation (C.11) is only true for isotropic (spherically symmetric) flux. For anisotropic fluxes, as in the ‘‘gradient, droplet growth model’’ presented in chapter 3, the integral in equation (C.8) cannot be trivially integrated.

We again allow the flux and the exterior mass density ρ_0 to be spatially dependent, but maintain the assumptions that ρ_1 is fixed, and thus, the flux J_1 is negligible. Equation (C.8) becomes then,

$$\int_{\partial V_1} \left((\rho_1 - \rho_0) \frac{d\mathbf{q}}{dt} - \mathbf{J}_0 \right) \cdot d\mathcal{A} = 0. \quad (\text{C.12})$$

We define $d\mathbf{G}/dt$ as the surface velocity in the situation where the flux of material into the drop at each point directly matches the surface flux at that point, such that the interior of the integral in equation (C.12) is 0 at all points along the droplet surface. The integral of $d\mathbf{G}/dt$ over the entire surface of the droplet would then give the total change in volume of the droplet,

$$\frac{dV}{dt} = \int_{\partial V_1} \frac{d\mathbf{G}}{dt} \cdot d\mathcal{A}. \quad (\text{C.13})$$

Assuming irrespective of $d\mathbf{G}/dt$, droplet growth is spherically symmetric, but the change in volume is conserved, the droplet growth rate is then,

$$\frac{dR}{dt} = \frac{1}{4\pi R^2} \int_{\partial V_1} \frac{\mathbf{J}_0}{\rho_1 - \rho_0} \cdot d\mathcal{A}, \quad (\text{C.14})$$

which simplifies to equation (C.10) in the spherically symmetric case. The droplet growth rate in terms of volume fractions is then simply,

$$\frac{dR}{dt} = \frac{1}{4\pi R^2} \int_{\partial V_1} \frac{\mathbf{J}_0^\phi}{\phi_1 - \phi_0} \cdot d\mathcal{A}. \quad (\text{C.15})$$

D. Derivation of Background Monomer Field for Droplet Growth

We now derive the equation for the monomeric background ϕ field, where it is referred to ϕ_i within a droplet, and $\phi_0(\mathbf{r})$ outside. This is a derivation of how droplet growth effects the background field of an incompressible binary fluid. The volume fraction is generally defined with respect to the “b” component as,

$$\phi \equiv \frac{N^b v^b}{V}, \quad (\text{D.1})$$

giving the derivative of ϕ as,

$$\frac{d\phi}{dt} = \frac{v^b}{V} \left(\frac{dN^b}{dt} - \frac{n^b}{V} \frac{dV}{dt} \right). \quad (\text{D.2})$$

These equations are general, where N^b is the number of “b” particles in some volume V , and the only assumption is that the system is incompressible such that the molecular volume of “b”, v^b , is constant.

We assume that droplet growth occurs at a quasi-static limit, where the volume fraction directly interior and the exterior of the droplet are allowed to relax to a local equilibrium, and that the interior of the droplet becomes uniform,

$$\begin{aligned} \phi_i(r \leq R^-) &= \phi_i \\ \lim_{r \rightarrow R^+} \phi_0(r) &= \phi_i^R. \end{aligned} \quad (\text{D.3})$$

These ϕ are set by a local energetic relaxation, the Gibbs-Thomson relation, and independent of the general dynamics of the system. Thus their evolution depends only on the droplet curvature and change in the free energy landscape as droplets diffuse. Although we are interested in both growing and shrinking droplets, we are mainly interested in relatively stable droplets. That is droplets are assumed to be at least of the same order as the critical size. For the time scale we are interested in, the change of ϕ due to the change of droplet curvature is thus negligible, $d\phi_i/dt \approx 0$. Using eqn. (D.2), we have in the droplet interior,

$$\frac{dN_i^b}{dt} = \frac{N_i^b}{V_i} \frac{dV_i}{dt}. \quad (\text{D.4})$$

We define a subvolume V_0 , which contains a droplet, V_i , where the total volume of both is constant, and are only interested in changes in this subvolume with respect to the droplet, i.e.

$$\begin{aligned}\frac{dN_0^b}{dt} &= -\frac{dN_1^b}{dt} \\ \frac{dV_0}{dt} &= -\frac{dV_1}{dt}.\end{aligned}\tag{D.5}$$

Now substituting the relations equations, (D.4) and (D.5) into equation (D.2), gives the local evolution of the background ϕ field due to the growth of droplet i ,

$$\frac{d\phi_0}{dt} = \frac{1}{V_0} \frac{dV_i}{dt} (\phi_0 - \phi_i).\tag{D.6}$$

Glossary of Terms

A significant amount of biology and biological experiments are presented in this thesis. Although most of the biology discussed here is learned in the canon of biological studies, some of it might be unfamiliar to the theoretical physicist. To simplify the understanding of the following work, a listing of biological and physical terms used in this text, and a concise definition of the term is provided here:

Biological Terms

- *Caenorhabditis elegans* (*C. elegans*): 1 mm long transparent nematode (round worm) living in soil.
- embryo: A multicellular eukaryotic organism in the stages of development. This can be from the first cell stage of an organism, all the way to birth. In humans, the term embryo is used only for the first 8 weeks after fertilization. (wikipedia)
- embryogenesis: Development of the embryo.
- epiblast: A tissue type derived from the inner cell mass during mammal embryogenesis, which goes on to form the primary germ layers of the embryo in gastrulation. Also referred to as the primary ectoderm. (wikipedia)
- eukaryotic cell: Cells of “higher level” organisms as compared to prokaryotes. The key defining feature of the cell, is a membrane bound nucleus which contains the cell’s DNA. These cells are typically much larger than prokaryotes. (wikipedia)
- germline: The line of cells that have genetic material that may be passed on to offspring. This includes cells that directly contain the genetic material, e.g. sperm and egg, as well as the cells that produce them (wikipedia).
- green fluorescent protein (GFP): protein composed of 238 amino acid residues, that exhibits bright green fluorescence when exposed to blue light. The gene is attached to protein sequence genes as a marker, see GFP tagging (wikipedia).
- nuclear pore complex (NPC): Complex protein structures that span the nuclear envelope allowing small water soluble molecules (< 40 K DA) to freely diffuse across the membrane, and mediating the transport of larger molecules through

specific signal sequences. Thousands of NPC's can cover a single nucleus. (wikipedia)

- oocyte: Female germ cell involved in reproduction, i.e. unfertilized egg. (wikipedia)
- ovum: Egg after fertilization. (wikipedia)
- pro-nuclear meeting (pnm): The time point when the sperm-derived pronucleus and oocyte pronucleus meet.
- RNA interference (RNAi): Is a system in living cells that takes part in controlling which genes are active and how active they are. This is done by small RNA molecules binding other RNAs and either increasing or decreasing their activity, e.g. preventing a messenger RNA from producing a protein. This is used experimentally to drastically reduce the expression of a certain gene. (wikipedia)
- somatic cell: In a multicellular organism, this is any cell forming the body of an organism, that is any cell that is not a germ cell, or an undifferentiated stem cell. (wikipedia)
- spermatheca: An organ in the female reproductive system that stores sperm. In the *C. elegans* worm, oocytes are fertilized by passing through the spermatheca.

Physical Concepts

- advection: Fluid motion by bulk motion (Note: This definition overlaps with the definition of convection as used in fluid mechanics, and VERY OFTEN convection is used to mean only advection, see wikipedia)
- convection: Movement of molecules with fluids, i.e. fluid motion. In fluid mechanics convection refers to the motion of fluid regardless of cause. In thermodynamics this refers to heat transfer by convection. Can be divided into 2 parts, advection and diffusion.(wikipedia)
- diffusion: motion of individual particles

Protein Acronyms

- GLH (GermLine Helicase): Constitutive P granule component. Required for the production of functional sperm. (Worm Base)
- H2B-histone: Histone protein.

- MEX-5 (Muscle EXcess): Essential for transducing polarity cues and establishing soma/germline asymmetry in the early embryo.
- PAR-1 (abnormal embryonic PARTitioning of cytoplasm): one of a series of cortex associated proteins that are required for proper asymmetric cell division of *C.elegans* during development. PAR-1 in particular, localizes to the same cell as P granules. (Worm Base)
- PGL-1 (P-GranuLe abnormality): RNA-binding protein that contains RGG motif. Localized in germ granules (P granules). Abnormalities lead to infertility. (Worm Base) maturation and duplication, and hence mitotic spindle assembly. Localizes to the centriole and pericentriolar material of centrosome. (Worm Base)
- SPD-5 (SPindle Defective): Required for centrosome maturation, symmetry breaking, pronuclear migration, mitotic spindle assembly, and cell division. Localizes to the pericentriolar material of centrosome. (Worm Base)

Experimental Techniques

- DAPI (4',6-diamidino-2-phenylindole): A fluorescent stain marker that strongly binds A-T rich regions of DNA. It can pass through the cell membrane and is used to stain both living and fixed cells. (wikipedia)
- Differential interference contrast (DIC) microscopy: Optical microscopy illumination technique used to enhance contrast in unstained, transparent samples. Works by separating (shearing) orthogonally polarized light into two separate paths and recombining before observation. The interference pattern is sensitive to the optical path difference, providing a contrast proportional to the path length gradient along the shear direction, giving the appearance of a 3D physical relief corresponding to the variation of the optical density of the sample. This method emphasises lines and edges though not providing a topographically accurate image. (wikipedia)
- Fluorescence recovery after photobleaching (FRAP): Optical technique used to measure the diffusion of fluorescent labeled probes within a thin medium or cell. A light source is focused onto a small patch of the medium. The fluorophores in this region are overexposed to high intensity light of the proper frequency such that their fluorescence lifetime is quickly elapsed. The recovery time, time for fluorescent molecules from outside this region to diffuse into this region is then measured. Assuming a Gaussian profile of the light beam, the diffusion coefficient would be approximately the area of the patch over the time for half the initial intensity to recover, $D = A/4T_{1/2}$ (wikipedia).

- GFP Tagging (Nomenclature: GFP::[Target Protein], where protein acronyms are all upper case): In a cell that produces the target protein, the gene for GFP is spliced into the gene for the target protein, and is thus produced with the target protein. This protein can then be observed since GFP fluoresces under blue light.
- Particle imaging velocimetry (PIV): Optical method of flow visualization. A fluid is seeded with tracer particles that are assumed to follow the flow dynamics. Motion of these tracer particles are tracked and a 2D vector field can be created. (wikipedia)
- RNAi knockdown (Nomenclature: [Target Gene](RNAi), where gene acronyms are lower case in the *C. elegans*): Refers to a target gene being knocked down using RNAi, reducing the protein production of said gene.

Bibliography

- [1] F Alber, S Dokudovskaya, L M Veenhoff, W Zhang, J Kipper, D Devos, A Suprpto, O Karni-Schmidt, R Williams, B T Chait, A Sali, and M P Rout. The molecular architecture of the nuclear pore complex. Nature, 450(7170):695–701, 2007.
- [2] B Alberts, A Johnson, J Lewis, M Raff, K Roberts, and P Walter. Molecular biology of the cell. Garland Science, 4th edition, 2002.
- [3] A Amiri, B D Keiper, I Kawasaki, Y Fan, Y Kohara, R E Rhoads, and S Strome. An isoform of eIF4E is a component of germ granules and is required for spermatogenesis in *C.elegans*. Development, 128(20):3899–3912, 2001.
- [4] The *C.elegans* Sequencing Consortium. Genome sequence of the nematode *C.elegans*: A platform for investigating biology. Science, 282(5433):2012–1493, (2012)1998.
- [5] K Binder. Theory of first-order phase transitions. Rep Prog Phys, 50(7):783–859, 1987.
- [6] C P Brangwynne, C R Eckmann, D S Courson, A Rybarska, C Hoege, J Gharakhani, F Jülicher, and A A Hyman. Germline P granules are liquid droplets that localize by controlled dissolution/condensation. Science, 324(5935):1729–1732, 2009.
- [7] C P Brangwynne, T J Mitchison, and A A Hyman. Active liquid-like behavior of nucleoli determines their size and shape in *Xenopus laevis* oocytes. P Natl Acad Sci Usa, 108(11):4334–4339, 2011.
- [8] A J Bray and C L Emmott. Lifshitz-Slyozov scaling for late-stage coarsening with an order-parameter-dependent mobility. Phys. Rev. B, 52(2):R685–R688, 1995.
- [9] S Brenner. The genetics of *Caenorhabditis elegans*. Genetics, 77(1):71–94, 1974.
- [10] J W Cahn and J E Hilliard. Free energy of a nonuniform system. 1. Interfacial free energy. J Chem Phys, 28(2):258–267, 1958.
- [11] R J Cheeks, J C Canman, W N Gabriel, N Meyer, S Strome, and B Goldstein. *C.elegans* PAR proteins function by mobilizing and stabilizing asymmetrically localized protein complexes. Current Biology, 14(10):851–862, 2004.

- [12] J F Collet and T Goudon. On solutions of the Lifshitz-Slyozov model. Nonlinearity, 13(4):1239–1262, 2000.
- [13] M C Cross and P C Hohenberg. Pattern formation outside of equilibrium. Reviews of Modern Physics, 65(3):851–1112, 1993.
- [14] C DeRenzo, K J Reese, and G Seydoux. Exclusion of germ plasm proteins from somatic lineages by cullin-dependent degradation. Nature, 424(6949):685–689, 2003.
- [15] C.elegans II. Cold Spring Harbor Monograph Series, Vol.33. Edited by D L Donald, T Blumenthal, B J Meyer, J R Preiss. Cold Spring Harbor Laboratory Press., 1997.
- [16] K Ernst and J J Hoffman. Oscillatory evolution of laser-induced aerosol in Cs2 vapor. Chemical Physics Letters, 75(2):388–391, 1980.
- [17] A Z Fire and C C Mello. The nobel prize in physiology or medicine. http://www.nobelprize.org/nobel_prizes/medicine/laureates/2006/, 2006.
- [18] M E Fisher. Correlation functions and the critical region of simple fluids. Journal of Mathematical Physics, 5:944–962, 1964.
- [19] P J Flory. Thermodynamics of high polymer solutions. J. Chem. Phys. 10:55–62, 1942.
- [20] P J Flory and W R Krigbaum. Thermodynamics of high polymer solutions. Annu Rev Phys Chem, 2:383–402, 1951.
- [21] S Frey, R P Richter, and D Goerlich. FG-rich repeats of nuclear pore proteins form a three-dimensional meshwork with hydrogel-like properties. Science, 314(5800):815–817, 2006.
- [22] C M Gallo, J T Wang, F Motegi, and G Seydoux. Cytoplasmic partitioning of P granule components is not required to specify the germline in *C.elegans*. Science, 330(6011):1685–1689, 2010.
- [23] A Gierer. Generation of biological patterns and form: Some physical, mathematical, and logical aspects. Progress In Biophysics & Molecular Biology, 37(1):1–47, 1981.
- [24] J P Gollub and J S Langer. Pattern formation in nonequilibrium physics. Reviews of Modern Physics, 71(2):S396–S403, 1999.
- [25] P Gönczy. Mechanisms of asymmetric cell division: Flies and worms pave the way. Nature Reviews Molecular Cell Biology, 9(5):355–366, 2008.

- [26] M Grant, J Yao, and H Guo. Growth kinetics in exciton systems. Phys. Rev. B, 47(3):1270–1275, 1993.
- [27] G Greenan, Cl P Brangwynne, S Jaensch, J Gharakhani, F Jülicher, and A A Hyman. Centrosome size sets mitotic spindle length in *Caenorhabditis elegans* embryos. Current Biology, 20(4):1–6, 2010.
- [28] E E Griffin, D J Odde, and G Seydoux. Regulation of the MEX-5 gradient by a spatially segregated kinase/phosphatase cycle. Cell, 146(6):955–968, 2011.
- [29] M E Gruidl, P A Smith, K A Kuznicki, J S McCrone, J Kirchner, D L Rousell, S Strome, and K L Bennett. Multiple potential germ-line helicases are components of the germ-line-specific P granules of *Caenorhabditis elegans*. P Natl Acad Sci Usa, 93(24):13837–13842, 1996.
- [30] N J Günther, D A Nicole, and D J Wallace. Goldstone modes in vacuum decay and first-order phase transitions. Journal Of Physics A-Mathematical And General, 13(5):1755–1767, 1980.
- [31] J D Gunton, M San Miguel, and P S Sahni. The dynamics of first-order phase transitions. In J.D.Gunton, editor, Phase Transitions, volume 8, chapter 3. Academic Press, London, 1983.
- [32] K Hayashi, S M Chuva S Lopes, and M A Surani. Germ cell specification in mice. Science, 316(5823):394–396, 2007.
- [33] S N Hird, J E Paulsen, and S Strome. Segregation of germ granules in living *Caenorhabditis elegans* embryos: Cell-type-specific mechanisms for cytoplasmic localisation. Development, 122(4):1303–1312, 1996.
- [34] S N Hird and J G White. Cortical and cytoplasmic flow polarity in early embryonic cells of *Caenorhabditis elegans*. Journal of Cell Biology, 121(6):1343–1355, 1993.
- [35] N G Van Kampen. Condensation of a classical gas with long-range attraction. Physical Review, 135(2A):A362–A369, 1964.
- [36] I Kawasaki, A Amiri, Y Fan, N Meyer, S Dunkelbarger, T Motohashi, T Karashima, O Bossinger, and S Strome. The pgl family proteins associate with germ granules and function redundantly in *Caenorhabditis elegans* germline development. Genetics, 167(2):645–661, 2004.
- [37] I Kawasaki, Y-H Shim, J Kirchner, J Kaminker, W B Wood, and S Strome. PGL-1, a predicted RNA-binding component of germ granules, is essential for fertility in *C.elegans*. Cell, 94(5):635–645, 1998.

- [38] W G Kelly, C E Schaner, A F Dernburg, M H Lee, S K Kim, A M Villeneuve, and V Reinke. X-chromosome silencing in the germline of *C.elegans*. Development, 129(2):479–492, 2002.
- [39] M Kiledjian and G Dreyfuss. Primary structure and binding activity of the hnRNP U protein: Binding RNA through RGG box. EMBO Journal, 11(7):2655–2664, 1992.
- [40] K A Kuznicki, P A Smith, W M A Leung-Chiu, A O Estevez, H C Scott, and K L Bennett. Combinatorial RNA interference indicates GLH-4 can compensate for GLH-1; these two P granule components are critical for fertility in *C.elegans*. Development, 127(13):2907–2916, 2000.
- [41] J S Langer. Theory of nucleation rates. Phys. Rev. Lett., 21(14):973–975, 1968.
- [42] J S Langer. Statistical theory of the decay of metastable states. Annals of Physics, 54(2):258–275, 1969.
- [43] J S Langer. Kinetics of metastable states. In L. Garrido, editor, Systems far from equilibrium, volume 132 of Lecture Notes on Physics, pages 12–47. Springer-Verlag, New York, 1980.
- [44] J S Langer and A J Schwartz. Kinetics of nucleation in near-critical fluids. Phys Rev A, 21(3):948–958, 1980.
- [45] E M Lifshitz and L P Pitaevskii. Landau and Lifshitz course of theoretical physics; Physical kinetics, Vol. 10, Pergamon Press plc, 1st edition, 2002.
- [46] E M Lifshitz and V V Slyozov. The kinetics of precipitation from supersaturated solid solutions. J Phys Chem Solids, 19(1-2):35–50, 1961.
- [47] T Mattila, M Kulmala, and T Vesala. On the condensational growth of a multicomponent droplet. J Aerosol Sci, 28(4):553–564, 1997.
- [48] R McGraw and Y Liu. Kinetic potential and barrier crossing: A model for warm cloud drizzle formation. Physical Review Letters, 90(1):1–4, 2003.
- [49] R McGraw and Y Liu. Analytic formulation and parametrization of the kinetic potential theory for drizzle formation. Physical Review E, 70(3):1–13, 2004.
- [50] R McGraw and J H Saunders. A condensation feedback mechanism for oscillatory nucleation and growth. Aerosol Science And Technology, 3(4):367–380, 1984.
- [51] V Mitlin. Numerical study of a Lifshitz-Slyozov-like metastable dewetting model. Journal of Colloid and Interface Science, 233(1):153–158, 2001.

- [52] J D Murray. Mathematical Biology II. Spatial Models and Biomedical Applications. Springer, 3rd edition, 2003.
- [53] A A Nepomnyashchy and A A Golovin. General aspects of pattern formation. In Self-assembly, pattern formation and growth phenomena in nano-systems, 1st edition, Springer Netherland, 2006.
- [54] J N Pitt, J A Schisa, and J R Priess. P granules in the germ cells of *Caenorhabditis elegans* adults are associated with clusters of nuclear pores and contain RNA. Developmental Biology, 219(2):315–333, 2000.
- [55] W H Press, S A Teukolsky, W T Vetterling, and B P Flannery. Numerical Recipes in C. Cambridge University Press, 3rd edition, 1992.
- [56] M B Rubin, R M Noyes, and K W Smith. Gas-evolution oscillators. 9. A study of the ammonium nitrite oscillator. Journal of Physical Chemistry, 91(6):1618–1622, 1987.
- [57] C Sagui and M Grant. Theory of nucleation and growth during phase separation. Physical Review E, 59(4):4175–4187, 1999.
- [58] C Sagui, D S O’gorman, and M Grant. Nucleation and growth: Decay of a metastable state. Physical Review E (Statistical Physics), 56(1):21, 1997.
- [59] C E Schaner, G Deshpande, P D Schedl, and W G Kelly. A conserved chromatin architecture marks and maintains the restricted germ cell lineage in worms and flies. Developmental Cell, 5(5):747–757, 2003.
- [60] E Schierenberg, J E Sulston, T Cole, J S Laufer, and G Vonehrenstein. Embryonic-cell lineages and development of the nematode *Caenorhabditis elegans*. European Journal Of Cell Biology, 22(1):450–450, 1980.
- [61] J A Schisa, J N Pitt, and J R Priess. Analysis of RNA associated with P granules in germ cells of *C.elegans* adults. Development, 128(8):1287–1298, 2001.
- [62] S Q Schneider and B Bowerman. Cell polarity and the cytoskeleton in the *Caenorhabditis elegans* zygote. Annu Rev Genet, 37:221–249, 2003.
- [63] G Seydoux and A Fire. Soma-germline asymmetry in the distributions of embryonic RNAs in *Caenorhabditis elegans*. Development, 120(10):2823–2834, 1994.
- [64] E D Siggia. Late stages of spinodal decomposition in binary mixtures. Phys Rev A, 20(2):595–605, 1979.
- [65] K W Smith and R M Noyes. Gas evolution oscillators. 3. A computational model of the Morgan reaction. Journal of Physical Chemistry, 87(9):1520–1524, 1983.

- [66] C Spike, N Meyer, E Racen, A Orsborn, J Kirchner, K Kuznicki, C Yee, K Bennett, and S Strome. Genetic analysis of the *Caenorhabditis elegans* GLH family of P-granule proteins. Genetics, 178(4):1973–1987, 2008.
- [67] C A Spike, J Bader, V Reinke, and S Strome. DEPS-1 promotes P-granule assembly and RNA interference in *C.elegans* germ cells. Development, 135(5):983–993, 2008.
- [68] C A Spike and S Strome. Germ plasm: Protein degradation in the soma. Current Biology, 13(21):R837–R839, 2003.
- [69] S Strome and R Lehmann. Germ versus soma decisions: Lessons from flies and worms. Science, 316(5823):392–393, 2007.
- [70] S Strome and W B Wood. Generation of asymmetry and segregation of germline granules in early *C.elegans* embryos. Cell, 35(1):15–25, 1983.
- [71] M Suntharalingam and S.R Wenthe. Peering through the pore: Nuclear pore complex structure, assembly, and function. Developmental Cell, 4(6):775–789, 2003.
- [72] P R ten Wolde and D Frenkel. Numerical study of gas–liquid nucleation in partially miscible binary mixtures. The Journal of Chemical Physics, 109(22):9919–9927, 1998.
- [73] J R Tenlen, J N Molk, N London, B D Page, and J R Priess. MEX-5 asymmetry in one-cell *C.elegans* embryos requires PAR-4- and PAR-1-dependent phosphorylation. Development, 135(22):3665–3675, 2008.
- [74] M Tokuyama and K Kawasaki. Statistical-mechanical theory of coarsening of spherical droplets. Physica A, 123(2-3):386–411, 1984.
- [75] M Tokuyama, K Kawasaki, and Y Enomoto. Kinetic equations for Ostwald ripening. Physica A, 134(2):323–338, 1986.
- [76] K Tsumuraya and Y Miyata. Coarsening models incorporating both diffusion geometry and volume fraction of particles. Acta Metallurgica, 31(3):437–452, 1983.
- [77] A M Turing. The chemical basis of morphogenesis. Philosophical Transactions Of The Royal Society Of London Series B-Biological Sciences, 237(641):37–72, 1952.
- [78] D Updike and S Strome. P granule assembly and function in *Caenorhabditis elegans* germ cells. J Androl, 31(1):53–60, 2010.

-
- [79] D van der Spoel, P J van Marren, P Larsson, and N Timneanu. Bionumbers: Id 103914. <http://bionumbers.hms.harvard.edu/bionumber.aspx?id=103914&ver=2>, 2009.
- [80] C Wagner. Theorie der Alterung von Niederschlägen durch Umlösen (Ostwald-Reifung). Zeitschrift Fur Elektrochemie, 65(7-8):581–591, 1961.
- [81] O Wartlick, P Mumcu, A Kicheva, T Bittig, C Seum, F Jülicher, and M González-Gaitán. Dynamics of Dpp signaling and proliferation control. Science, 331(6021):1154–1159, 2011.
- [82] J H Yao, H Guo, and M Grant. Growth kinetics in exciton systems. Physical review. B, Condensed matter, 47(3):1270–1275, 1993.
- [83] Y Zhang, L Yan, Z Zhou, P Yang, E Tian, K Zhang, Y Zhao, Z Li, B Song, J Han, L Miao, and H Zhang. SEPA-1 mediates the specific recognition and degradation of P granule components by autophagy in *C.elegans*. Cell, 136(2):308–321, 2009.

Versicherung

Hiermit versichere ich, dass ich die vorliegende Arbeit ohne unzulässige Hilfe Dritter und ohne Benutzung anderer als der angegebenen Hilfsmittel angefertigt habe; die aus fremden Quellen direkt oder indirekt übernommenen Gedanken sind als solche kenntlich gemacht. Die Arbeit wurde bisher weder im Inland noch im Ausland in gleicher oder ähnlicher Form einer anderen Prüfungsbehörde vorgelegt. Die vorliegende Arbeit wurde vom 02.2008 bis 08.2012 unter der Aufsicht von Prof. Dr. Frank Jülicher am Max-Planck-Institut für Physik komplexer Systeme. und

Ich versichere, dass ich bisher keine erfolglosen Promotionsverfahren unternommen habe. Ich erkenne die Promotionsordnung der Fakultät Mathematik und Naturwissenschaften der Technischen Universität Dresden an.

Dresden, den 15.08.2012, jöbin gharakhani